



HAL
open science

Investigation of OPO cavities for high average power generation in the mid-infrared

Medina Manuel

► **To cite this version:**

Medina Manuel. Investigation of OPO cavities for high average power generation in the mid-infrared. Physics [physics]. Aix-Marseille Université, 2022. English. NNT: . tel-03688918

HAL Id: tel-03688918

<https://theses.hal.science/tel-03688918>

Submitted on 6 Jun 2022

HAL is a multi-disciplinary open access archive for the deposit and dissemination of scientific research documents, whether they are published or not. The documents may come from teaching and research institutions in France or abroad, or from public or private research centers.

L'archive ouverte pluridisciplinaire **HAL**, est destinée au dépôt et à la diffusion de documents scientifiques de niveau recherche, publiés ou non, émanant des établissements d'enseignement et de recherche français ou étrangers, des laboratoires publics ou privés.



Distributed under a Creative Commons Attribution - NonCommercial - NoDerivatives 4.0 International License

Doctoral thesis

Defended at ISL, French-German Research Institute of Saint-Louis
on 12 April 2022 by

Manuel Alessandro Medina

Investigation of OPO cavities for high average power generation in the mid-infrared

Discipline

Physique et Science de la Matière

Spécialité

Optique, Photonique et Traitement d'Image

École doctorale

ED 352

Laboratoire/Partenaires de recherche

ISL- French-German Research Institute of Saint-Louis

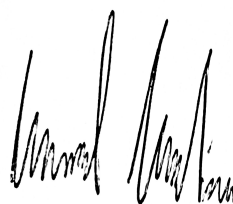
Composition du jury

•	Antoine Godard	Reviewer
•	ONERA	
•	Marwan Abdou Ahmed	Reviewer
•	Universität Stuttgart	
•	Fabrice Devaux	Examiner
•	Institute FEMTO-ST	
•	Patricia Segonds	President of the jury
•	Université Grenoble Alpes	
•	Antoine Berrou	ISL co-supervisor, In-
•	ISL	vited
•	Anne Dhollande	ISL supervisor
•	ISL	
•	Frank Rüdiger Wagner	Thesis director
•	Aix Marseille Université	

I, undersigned, Manuel Alessandro Medina hereby declare that the work presented in this manuscript is my own work, carried out under the scientific direction of Frank R. Wagner, in accordance with the principles of honesty, integrity and responsibility inherent to the research mission. The research work and the writing of this manuscript have been carried out in compliance with both the french national charter for Research Integrity and the Aix-Marseille University charter on the fight against plagiarism.

This work has not been submitted previously either in this country or in another country in the same or in a similar version to any other examination body.

Saint-Louis 28/01/2022



Cette œuvre est mise à disposition selon les termes de la [Licence Creative Commons Attribution - Pas d'Utilisation Commerciale - Pas de Modification 4.0 International](https://creativecommons.org/licenses/by-nc-nd/4.0/).

Journal publications and conference contributions

List of scientific publications within the thesis project :

1. M. A. Medina, M. Piotrowski, M. Schellhorn, F. R. Wagner, A. Berrou, and A. Hildenbrand-Dhollande. Beam quality and efficiency of ns-pulsed high-power mid-IR ZGP OPOs compared in linear and non-planar ring resonators. *Opt. Express*, **29** (14) :21727-21737, 2021.
2. M. Piotrowski, M. A. Medina, M. Schellhorn, G. Spindler, and A. Hildenbrand - Dhollande. Effects of pump pulse energy and repetition rate on beam quality in a high-power mid-infrared ZnGeP₂ OPO. *Opt. Express*, **29**(2) :2577-2586, 2021.

Conference contributions and summer school participation :

1. M. A. Medina, M. Piotrowski, M. Schellhorn, F. R. Wagner, A. Berrou, and A. Hildenbrand - Dhollande, *38 W high repetition rate ZGP OPO and novel approaches to improve beam quality in miniaturized non-planar cavities*, 9TH EPS-QEOD EUROPHOTON CONFERENCE (virtual), Prague, Czech Republic, (2020).
2. M. Piotrowski, M. A. Medina, M. Schellhorn, and A. Hildenbrand - Dhollande, *Temporally resolved studies of thermal effects in high power ZGP OPO pumped by high-repetition Ho :LLF MOPA system*, 9TH EPS-QEOD EUROPHOTON CONFERENCE (virtual), Prague, Czech Republic, (2020).
3. M. Piotrowski, M. A. Medina, G. Spindler, M. Schellhorn, and A. Hildenbrand - Dhollande, *Beam quality enhancement in high power mid-IR ZGP OPO Sources : a focus on a build-up of thermal lens*, Advanced Solid State Lasers, ASSL (virtual), Washington, D.C., United States, (2020).
4. M. A. Medina, M. Piotrowski, M. Schellhorn, F. R. Wagner, A. Berrou, and A. Hildenbrand - Dhollande, *Performances of mid-IR high-power ZGP OPOs compared in non-planar ring resonators*, Advanced Solid State Lasers, ASSL (virtual), Washington, D.C., United States, (2021).
5. M. A. Medina, M. Piotrowski, M. Schellhorn, F. R. Wagner, A. Berrou, and A. Hildenbrand - Dhollande, *Performance of mid-IR high-power ZGP OPO*

compared in linear and non-planar ring resonators, CLEO/EUROPE-EQEC (virtual), Munich, Germany, (2021).

6. M. Piotroski, M. A. Medina, and A. Hildenbrand - *Dhollande Non-planar image-rotating cavities allow to reach 30 W of average power in mid-IR with good beam quality from high-repetition-rate ns-pulsed ZGP OPOs*, Mid-Infrared Coherent Sources, MICS, Budapest, Hungary, 2022.
7. Summer School, Siegman International school on Lasers (virtual), Chęciny, Poland, (2020)
8. Summer School, Siegman International school on Lasers (virtual), Chęciny, Poland, (2021)

Résumé

Des sources lumineuses cohérentes émettant dans la région spectrale du moyen infrarouge (moyen IR) entre 3 et 5 μm , sont nécessaires pour de nombreuses applications civiles et militaires telles que la télédétection, la spectroscopie et les contre-mesures optroniques. Certaines de ces applications requièrent une émission impulsionnelle de forte puissance moyenne avec un taux de répétition élevé. Actuellement, la technique la plus mature pour générer un tel rayonnement consiste à convertir un faisceau de pompe vers des fréquences inférieures grâce à des oscillateurs paramétriques optiques (OPO). Malgré de nombreuses études de différents groupes de recherche impliqués dans ce domaine, le développement de systèmes compacts et fiables délivrant des dizaines de watts avec une bonne qualité de faisceau reste un défi. Les effets thermiques en jeu dans les cristaux et le seuil d'endommagement sous fort flux laser des composants impliqués dans ces systèmes à haute puissance sont les facteurs limitants.

L'objectif de cette thèse est de démontrer un système compact et robuste délivrant une puissance moyenne élevée dans le moyen IR (de l'ordre de plusieurs dizaines de watts) avec une bonne qualité de faisceau ($M^2 \leq 2$). La thèse se divise en deux parties. La première partie s'intéresse à l'investigation de différentes cavités OPO basées sur des cristaux non linéaires de phosphore de zinc et de germanium (ZGP). La source de pompe utilisée est un système MOPA (oscillateur maître amplifié en puissance) basé sur des cristaux $\text{Ho}^{3+}:\text{LLF}$. Cette source, développée à l'ISL, délivre une puissance moyenne de sortie de 68,7 W à une cadence de 10 kHz à une longueur d'onde de 2,065 μm , et une qualité de faisceau limitée par la diffraction. L'étude comprend des cavités linéaires et deux cavités non-planaires à rotation d'images, appelées RISTRA et FIRE. Les avantages et les inconvénients de chaque architecture, ainsi qu'une comparaison entre les cavités sont reportés. Une puissance maximale de sortie de 38 W avec un facteur $M^2 = 2,2$ est démontrée à l'aide d'un résonateur linéaire. Grâce à la cavité FIRE, la qualité du faisceau a été améliorée avec un facteur $M^2 = 1,4$ pour une puissance en sortie de 25 W.

Dans une deuxième partie, cette thèse montre comment les performances de ces cavités non planaires peuvent être améliorées, d'un point de vue de la puissance et de la qualité du faisceau de sortie. La diminution de la taille du faisceau de pompe nous permet de diminuer le seuil d'oscillation et d'augmenter la puissance moyenne, obtenant ainsi jusqu'à 30 W de puissance en sortie de la cavité RISTRA et atteignant l'une des limites de notre configuration. Par ailleurs, il est important de disposer de sources compactes pour certaines appli-

cations notamment militaires. Une cavité FIRE miniaturisée a donc été conçue, construite et étudiée. Une puissance de sortie totale de 24 W avec une bonne qualité de faisceau ($M^2 = 1,6$) est obtenue, prouvant que des performances similaires peuvent être atteintes avec une conception OPO très compacte. Enfin, des études paramétriques sur la dépendance de la qualité des faisceaux en sortie des résonateurs non plans en fonction, notamment, du taux de répétition du laser de pompe, ont permis de mieux comprendre l'influence de ces paramètres sur sa détérioration. Cette meilleure compréhension ouvre la voie à une optimisation du fonctionnement de l'OPO et une amélioration de la qualité des faisceaux en sortie.

Mots clés : oscillateurs paramétriques optiques, OPO, optique non linéaire, ZGP, cavité non plane, puissance moyenne élevée, qualité du faisceau, FIRE, RISTRA

Abstract

High repetition rate, high average power, coherent light sources emitting in the mid infrared (mid-IR) spectral region (3-5 μm) are important for many civil and military applications, such as remote sensing, spectroscopy and defense countermeasures.

Currently, the most mature technique to deliver such radiation is through frequency down-conversion in Optical Parametric Oscillators (OPOs). Despite many studies of different research groups involved in this field, developing compact and reliable systems delivering tens of watts with good beam quality is still challenging. The thermal effects in nonlinear crystals and optical damage threshold of components involved in such high power systems are the limiting factors.

The aim of this thesis is to demonstrate a compact and robust system delivering mid-IR high average power (in the order of tens of watts) with good beam quality ($M^2 \leq 2$). The thesis can be divided in two parts. The first part of this work is dedicated to the investigation of different OPO resonators based on nonlinear crystals of Zinc Germanium Phosphide (ZGP). The OPO pump source is a 10 kHz, Ho^{3+} :LLF MOPA (Master Oscillator Power Amplifier) system, developed at ISL and delivering 68.7 W of total output power at a wavelength of 2.065 μm with a diffraction limited beam quality. The study includes linear resonators, and two different non-planar ring cavities, the so-called RISTRA and FIRE resonators. We explore the advantages and drawbacks of each design and a comparison between them is reported. A maximum output power of 38 W with an $M^2 = 2.2$ is demonstrated using a linear resonator, while the beam quality is improved down to an $M^2 = 1.4$, in the FIRE resonator, at an output power of 25 W.

In the second part, this thesis shows how the performances of these devices can be further enhanced, both in power and output beam quality. At first, reducing the pump spot size allows us to decrease the oscillation threshold and up-scale the average power, obtaining 30 W in RISTRA and reaching one of the limitation of our setup. Moreover, since SWaP (Size, Weight, and Power)-optimized sources are important for certain applications, in particular military, a miniaturized FIRE cavity is designed, built and investigated. A total output power of 24 W with good beam quality ($M^2 = 1.6$) is obtained, proving that similar performances can be achieved with a very compact OPO design. Then, parametric studies on the beam quality dependence on different factors, such as pump repetition rate, allows us a better understanding of the effects which

concur to deteriorate it. This paves the way to optimizations of the OPO operation and further improvement of the output beam quality in the non-planar ring resonators.

Keywords : optical parametric oscillators, OPO, nonlinear optics, ZGP, non-planar cavity, high average power, beam quality, FIRE, RISTRA.

Synopsis

Etude des cavités OPO pour la génération de hautes puissances dans l'infrarouge moyen

La longueur d'onde d'émission d'un laser étant définie par les niveaux d'énergie dans le milieu à gain, celle-ci ne peut pas être choisie de façon arbitraire. Malheureusement, en raison d'un manque de matériaux, il existe encore des régions spectrales pour lesquelles des lasers efficaces ne sont pas disponibles. Une gamme spectrale d'intérêt particulier se situe dans la région du moyen infrarouge (moyen IR), c'est-à-dire pour des longueurs d'onde entre 3 et 5 μm . Les applications à ces longueurs d'onde vont de la spectroscopie, la télédétection, la télécommunication aux applications médicales et militaires. Une application notable de ce rayonnement IR est son utilisation dans les systèmes de contre-mesure optroniques (IRCM), qui servent à protéger les avions civils ou militaires contre les missiles à guidage thermique. Dans ce domaine, un faisceau laser moyen IR peut être utilisé pour aveugler, brouiller ou même détruire le détecteur infrarouge du missile. De plus, une telle application a des besoins très exigeants pour la source infrarouge : le système doit être compact, robuste et doit fournir un faisceau stable avec une puissance élevée et un large spectre dans la plage spectrale souhaitée. De plus, comme le faisceau de la source doit parcourir de longues distances dans l'atmosphère pour atteindre son objectif, le faisceau de sortie doit avoir une bonne qualité de faisceau, donc une faible divergence, afin de délivrer l'énergie utile sur la cible.

Actuellement, la technique la plus mature pour générer un tel rayonnement consiste à convertir un faisceau de pompe vers des longueurs d'onde supérieures grâce à des oscillateurs paramétriques optiques (OPO). Les deux faisceaux générés présentent la même cohérence caractéristique d'un faisceau laser, mais sont accordables en continu sur une large gamme spectrale. Lorsque nous nous concentrons sur les applications possibles dans le domaine spectral IR moyen, telles que les systèmes IRCM, les OPOs pulsés en régime nanoseconde offrent de bonnes conditions pour la génération de faisceaux à haute énergie et haute puissance moyenne.

Malgré de nombreuses études de différents groupes de recherche impliqués dans ce domaine, le développement de systèmes compacts et fiables délivrant des dizaines de watts avec une bonne qualité de faisceau reste un défi. Les effets thermiques en jeu dans les cristaux et le seuil d'endommagement sous fort

flux laser des composants impliqués dans ces systèmes à haute puissance sont les facteurs limitants. Habituellement, la puissance moyenne élevée requise est obtenue par l'utilisation d'un étage d'amplification. Cependant, pour les applications où la compacité est essentielle, comme dans les systèmes IRCM, cela vaut la peine d'étudier les OPO à un seul étage.

L'objectif de cette thèse est de démontrer un système compact et robuste délivrant une puissance moyenne élevée dans le moyen IR (de l'ordre de plusieurs dizaines de watts) avec une bonne qualité de faisceau ($M^2 \leq 2$). Afin d'atteindre ce résultat, nous utiliserons comme matériau non linéaire des cristaux de phosphore de zinc et de germanium (ZGP), actuellement la technologie la plus mature pour la conversion de haute puissance dans le moyen IR. Peu de sources expérimentales de haute puissance basées sur des OPO avec ZGP et délivrant des dizaines de watts ont été démontrées, et beaucoup souffraient d'une stabilité ou d'une qualité de faisceau limitée. De plus, même si le type de résonateur utilisé pour l'OPO pulsé joue un rôle important dans la résolution des difficultés de stabilité et de qualité de faisceau dans les sources de haute puissance, peu d'études publiées ont testé de manière adéquate les performances de différents types de résonateurs dans les expériences OPO.

Compte tenu de cela, dans cette thèse, nous avons étudié différents résonateurs OPO et nous avons comparé leurs performances dans des conditions similaires. Les cavités étudiées sont un résonateur linéaire et deux types de cavités non-planaires à rotation d'images, appelées RISTRA et FIRE. Leurs géométries et configuration de miroirs sont illustrées dans la Fig. 1.

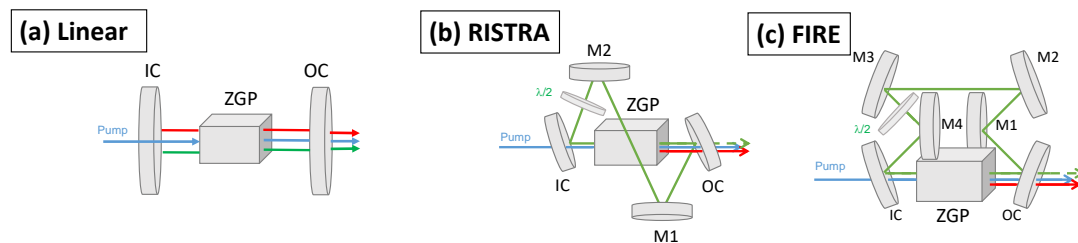


FIGURE 1 : Les trois cavités différentes qui ont été étudiées au cours de la thèse. (a) Résonateur linéaire. (b) Résonateur RISTRA. (c) Résonateur FIRE.

La source de pompe utilisée est un système MOPA (oscillateur maître amplifié en puissance) basé sur des cristaux $\text{Ho}^{3+}:\text{LLF}$. Cette source, développée à l'ISL, délivre une puissance moyenne de sortie de 68,7 W à une cadence de 10 kHz à une longueur d'onde de $2,065 \mu\text{m}$ et avec une qualité de faisceau limitée par la diffraction. Une puissance maximale de sortie de 38 W (66 W de puissance de pompe) avec un facteur $M^2 = 2,2$ est démontrée à l'aide d'un résonateur li-

néaire doublement résonnant de 46 mm de long. Les facteurs de propagation du faisceau ont ensuite été améliorés dans les résonateurs non-planaires : $M^2 = 1,8$ dans le RISTRA, et $M^2 = 1,4$ dans le FIRE. Leurs rendements de conversion étaient comparables au résonateur linéaire, mais la puissance de sortie obtenue était plus faible en raison de leur seuil d'oscillation plus élevé. Nous avons obtenu 25 W de puissance de sortie dans le RISTRA et 21 W dans le FIRE. Il s'agit de la première démonstration de telles cavités en régime de taux de répétition élevé et haute puissance moyenne.

À partir de ces premières démonstrations d'amélioration de la qualité des faisceaux dans les cavités FIRE et RISTRA, nous avons mené des études pour augmenter encore leurs performances. Étant limité par la puissance de sortie de la source de la pompe, la première approche pour augmenter la puissance de sortie de l'OPO a été d'abaisser son seuil d'oscillation. Nous avons donc augmenté la fluence de la pompe dans le ZGP en réduisant son diamètre de faisceau de 1 mm à 0,7 mm. Cela nous a permis d'atteindre 30 W de puissance totale en sortie pour le RISTRA et 27 W pour le FIRE. Cependant, nous avons atteint le seuil de dommage laser des optiques. Par conséquent, nous avons exploré une autre méthode pour augmenter la puissance du système. Nous avons conçu, construit et étudié une version miniaturisée de la cavité FIRE appelée mini-FIRE, ayant une longueur optique de la cavité plus courte (135 mm contre 265 mm). Un système de refroidissement par eau du cristal non linéaire a également été ajouté au résonateur. Une image du résonateur est montrée dans la Fig. 2.

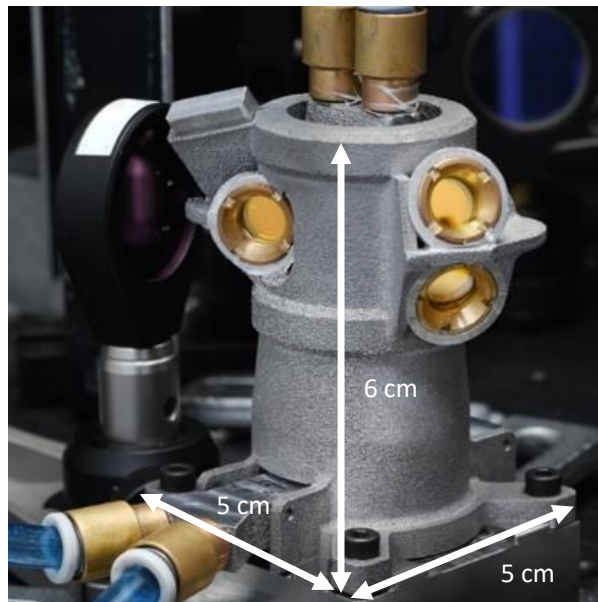


FIGURE 2 : Photo du résonateur mini-FIRE.

Dans cette configuration, en utilisant un ZGP de 16 mm de long, nous avons obtenu 24 W de puissance de sortie avec un $M^2 = 1,6$. Une comparaison avec la conception FIRE précédente a été faite à l'aide de simulations du logiciel OPODESIGN. Ce résultat prouve que des performances similaires à celles de la cavité FIRE peuvent être atteintes en utilisant un résonateur beaucoup plus compact.

En plus des études précédentes, nous avons également étudié les facteurs qui contribuent à détériorer la qualité du faisceau en sortie de l'OPO. Tout d'abord, nous avons étudié la dépendance du facteur de propagation du faisceau sur le refroidissement par eau du ZGP. Cela a été fait en faisant des études résolues en temps sur les facteurs M^2 à puissance maximale pour le RISTRA, FIRE et mini-FIRE. Le mini-FIRE en particulier a été étudié en présence et en l'absence de refroidissement par eau, concluant qu'un système de refroidissement est crucial pour fournir un faisceau avec un M^2 stable et faible. L'étude, menée avec une résolution temporelle de 20 ms, a dévoilé le comportement dynamique de la lentille thermique avant d'atteindre l'équilibre. Dans les applications où la qualité du faisceau est critique, ce résultat pourrait être utile lorsque l'on considère le cycle de service de tels systèmes. Dans une deuxième étude, nous avons étudié les deux facteurs qui concourent à la détérioration de M^2 . Les contributions de la lentille thermique et de l'effet de guidage par le gain sur la qualité du faisceau ont été séparées. Cela a été fait en inspectant la dépendance du facteur M^2 en fonction du taux de répétition du laser de pompe à une énergie d'impulsion constante (6 mJ pour RISTRA et 5,3 mJ pour FIRE). En conséquence, nous avons révélé des conditions pour délivrer une qualité de faisceau optimale. Les résultats ont été étayés par des simulations numériques.

Acknowledgment

I must say, it was quite a ride. With up and downs of course, but always interesting and enriching. None of the work done here would have been possible without the help of several people.

First of all, I would like to thank my thesis director Dr. Frank R. Wagner. You first accepted me as your student without really knowing me, and despite the distance, you were always available and ready to help me when I needed. Your numerous insights were of great help in these past three years. I am also really grateful to my ISL supervisors : Dr. Anne Dhollande and Dr. Antoine Berrou. Always ready to listen, discuss and with tons of daily advice. Thanks for giving me the opportunity to work in this group and pursuit my objective.

A big thank you also to all my colleagues (past and present ones) from the DPA group. From the very beginning you gave me a warm welcome and it has really been a pleasure to work among you in such a friendly environment. In particular, I'd like to thank deeply Dr. Marcin Piotrowski for the countless hours spent in the lab together and for all his work and personal advices. You showed what it really means to be a good, motivated researcher.

I'm also very grateful to Dr. Martin Schellhorn for the many interesting scientific discussions we had.

A particular thanks goes to Dr. Gerhard Spindler for cutting his own free time and help me to perform some of the simulations of this thesis.

Further credit goes to Joerg Schoener for managing the technical drawing and mechanical construction of the mini-FIRE resonator.

None of this work would have been accomplished without the possibility to take some break and blow off some steam. For this, I thank my various friends that during these years joined at one time or another the *Friday pizza nights* : Dennis, Laura, Cristina, Manuel, Juan, Gabriele, GianMarco, and Caterina and Massimiliano.

And finally, a warm thanks to my Mum, Dad, sister Gabriella and my brother Ernesto, simply for just being there, believe and support me.

Contents

Journal publications and conference contributions	ii
Résumé	iv
Abstract	vi
Synopsis	viii
Acknowledgment	xii
1. Introduction	3
1.1. Background	3
1.2. Aim of the thesis	4
1.3. Outline of the thesis	4
2. State of the art of mid-IR generation	6
2.1. Mid-IR sources	7
2.2. Nonlinear crystals	8
2.3. Pump sources	10
2.4. Optical parametric oscillators based on ZGP	12
3. Theory	17
3.1. Optical parametric generation	17
3.1.1. Phase-matching	19
3.1.2. Coupled wave equations	21
3.1.3. Parametric gain	22
3.2. Optical parametric oscillators	23
3.2.1. Frequency selection	25
3.2.2. Non-planar ring cavities	26
3.3. Laser sources and their characterization	30
3.3.1. Laser beam quality	30
3.3.2. Thermal lens and gain guiding	33
4. Experimental setup and simulation tools	36
4.1. Experimental setup	36
4.1.1. Pump source	36
4.1.2. Description of the setup	39

4.1.3.	ZGP crystals	42
4.1.4.	OPO cavities	44
4.2.	Simulation softwares	47
4.2.1.	SNLO	47
4.2.2.	OPODESIGN	49
5.	High power ZGP OPO comparison in different cavities	52
5.1.	Influence of linear cavity design on its performances	52
5.1.1.	Motivation	52
5.1.2.	Influence of cavity length	53
5.1.3.	Influence of output coupler curvatures	55
5.1.4.	Influence of output wavelengths	59
5.1.5.	Influence of crystal quality	62
5.1.6.	Characterization of the linear OPO cavity	64
5.2.	Performances of non-planar ring resonators	68
5.2.1.	Motivation	68
5.2.2.	The RISTRA resonator	69
5.2.3.	The FIRE resonator	72
5.3.	Comparison of linear, RISTRA and FIRE resonators	74
6.	Investigations on non-planar ring cavities	80
6.1.	Power scaling	80
6.1.1.	Motivation	80
6.1.2.	Different pump diameter	81
6.1.3.	Different cavity length: mini-FIRE	84
6.2.	Thermal management for improved beam quality	90
6.2.1.	Motivation	90
6.2.2.	Influence of water cooling	90
6.2.3.	Pulse repetition rate dependence	93
6.3.	Conclusions	96
7.	Conclusions and outlook	97
7.1.	Conclusions	97
7.2.	Outlook	99
A.	ZGP crystal data	101
B.	Publications	102
	References	133

1. Introduction

1.1. Background

In 1960, Maiman demonstrated for the first time the laser [1]. Since then, there has been a never-stopping development in the field. Lasers are nowadays widely used in many science fields, as well as in everyday life: they allow you to listen music from a CD, detect accurately environmental pollutants, are the backbone of the current communication networks.

Since the output wavelength of a laser is dictated by the energy levels in the gain medium, the emission wavelength can not be arbitrary. Unfortunately, due to a lack of convenient materials, there are still spectral regions not efficiently accessible. Frequency conversion through nonlinear optical processes however can overcome this issue, expanding the accessible region to virtually the whole spectrum, from ultraviolet to far-infrared.

A spectral range of particular interest lies within the mid-IR region, between 3 and 5 μm . Applications of such wavelengths range from spectroscopy, remote sensing, free space communication, to medical and military applications. A noteworthy use of such radiation is for infrared countermeasure (IRCM) systems, which are used to protect civil or military aircrafts from heat-seeking missiles. There, a mid-IR laser beam can be used to blind, jam, or even destroy the infrared detector of the incoming threat. Additionally, such application has very demanding needs for the infrared source: the system has to be compact, robust, and it must deliver a stable beam with high peak power and broad spectrum in the desired spectral range. Moreover, since the laser beam has to travel long distances in the atmosphere to reach its objective, the output beam must have a good beam quality, hence low divergence, in order to deliver the useful energy on target.

Nanosecond (ns)-pulsed Optical Parametric Oscillators (OPOs) are particular suitable to deliver such radiation. Invented in 1965 [2], OPOs convert a laser pump beam into two beams of lower frequency (higher wavelength). The two generated beams present the same characteristic coherence of a laser, but are continuously tunable over a wide spectral range. Despite the work of several research groups on the subject, to develop a mid-IR source with high average power (in the order of tens of watts) and good beam quality ($M^2 \leq 2$) is still challenging. Usually, the required high average power is achieved by the use of an amplification stage. However, for applications when the compactness is

essential, such as in IRCM systems, it is worth to investigate single stage OPOs.

1.2. Aim of the thesis

The aim of this thesis is to demonstrate a compact and robust OPO system delivering high average power (in the order of several tens of watts) in the $3 - 5 \mu\text{m}$ spectral region with good beam quality. In order to achieve this result, we will use as nonlinear material Zinc Germanium Phosphide (ZGP) crystals, currently the most mature technology for high power conversion in the mid-IR domain.

Few experimental high power sources based on ZGP OPOs and delivering tens of watts have been demonstrated, but many suffered from limited stability or beam quality. The thermal effects in the nonlinear crystal in particular, are the most troublesome when power scalability and good beam quality for the OPO beams are required at the same time. Moreover, even though the type of resonator used for ns-pulsed OPO plays an important role in addressing the difficulties of stability and beam quality in high power sources, few published studies adequately tested the performance of different types of resonators in OPO experiments.

Taking this into account, in this thesis three different OPO cavities will be implemented and compared. Possible factors affecting the conversion efficiency and the output beam quality are investigated, in order to power and beam quality up-scale their performances.

1.3. Outline of the thesis

The thesis is organized as follows:

In Chapter 2 the current state of the art for mid-IR generation is given. After a quick review on the different mid-IR sources, we focus on the OPO devices. The different pump sources, as well as the nonlinear crystals, are reviewed, highlighting their main drawbacks and advantages. Finally, we consider ZGP based single stage OPOs, reviewing the main experimental results obtained up to date, emphasizing in particular the different resonator designs used in the past.

In Chapter 3 the main theoretical aspects involved in the thesis are discussed. First, the basic theory of optical parametric generation is given, defining quantities such as phase-mismatch and parametric gain. Afterwards, the optical parametric oscillators are presented, with a particular focus on the non-planar ring cavities. Finally, some features regarding the characterization of the laser sources are discussed, such as the definition of laser beam quality, thermal lens, and gain guiding.

Chapter 4 focuses on the experimental setup used in this thesis. The OPO resonators, as well as the pump source and the characteristics of the ZGP crystals used are presented. The used methodology to measure the beam quality is also described here. Then, the simulation tools used in the thesis (SNLO and OPODESIGN) are discussed briefly, highlighting their main advantages and drawbacks.

Chapter 5 presents the first part of the experimental results, focused on the implementation and comparison of three different OPO cavities. After a first study on the influence of several features on the OPO performances, a linear resonator is implemented with the best performing ZGP crystal available. Then, the non-planar ring cavities named RISTRA and FIRE are implemented and studied. Finally, a comparison of the three resonators is drafted.

Chapter 6 focuses on the second part of the experimental results, which address the power and beam quality up-scaling issues of the RISTRA and FIRE cavities. Attempts to increase the output power are done by decreasing the pump spot size and the cavity lengths of the resonators. The latter is achieved by designing, fabricating, and studying a novel miniaturized version of the FIRE resonator. To improve the beam quality, the thermal effects arising in the crystal are investigated. This study is done by analyzing the dependence of the M^2 factor on the crystal cooling and pump pulse repetition rate.

Finally, Chapter 7 summarizes the main results of the thesis and gives an outlook based on the work done.

2. State of the art of mid-IR generation

The infrared (IR) spectral domain is usually divided in three smaller sub-regions: near-infrared (NIR), mid-infrared (mid-IR) and far-infrared (FIR). Although the ISO standard (EN ISO 20473) considers the mid-IR as the wavelengths from 3 to 50 μm , its definition can vary substantially depending on the field-specific community.

If we consider the atmospheric transmission, presented in Fig. 2.1, the mid-IR is usually considered as the spectral range from 3 to 15 μm . Between these two wavelengths, two transparency windows exist: the so-called band II region (from 3 to 5.5 μm) and the band III region (8 to 14 μm).

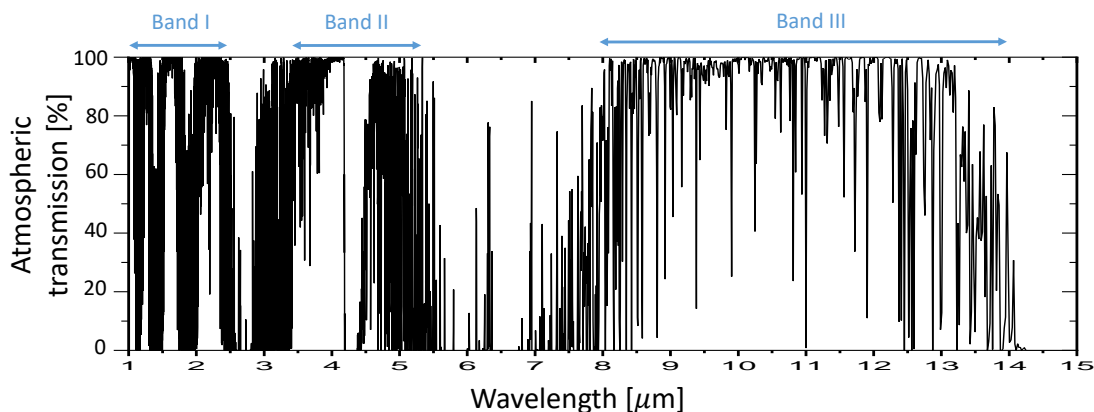


Figure 2.1: Transmission spectrum of the atmosphere between 1 and 15 μm . Data taken from [3], considering a transmission distance of 1 km and humidity of 1.86 % at ground level.

The area of interest and possible application of such wavelengths is wide [4]. They range from spectroscopy sensing and imaging, to metrology, medical applications, mid-IR plasmonics, free space communications etc. Among these, there are infrared countermeasure (IRCM) systems, which are used to protect aircrafts from heat-seeking missiles. There, a mid-IR laser beam is used to blind, jam, or even destroy the infrared detector of the incoming threat. In this field, typically high average power (from watt level to tens of watts), broadband, pulsed sources are needed.

In this thesis we will focus on the spectral region between 3 and 5 μm .

2.1. Mid-IR sources

There are several methods to generate mid-IR radiation with watt level average power. Direct emission can be obtained from few types of transition metal doped II-VI chalcogenides materials. The most common doping materials are Cr^{2+} and Fe^{2+} [5]. Although high average power (tens of watts) can be obtained from them [6], these mid-IR sources have some drawbacks. Cr^{2+} doped lasers have a limited tunability, with the longest output recorded at $3.6 \mu\text{m}$ from a $\text{Cr}:\text{CdSe}$ laser [7]. Fe^{2+} doped sources on the other hand can reach wavelengths up to around $7 \mu\text{m}$, but need to be pumped between 2.6 and $3 \mu\text{m}$, where there is a lack of high average power lasers [5]. Another method to deliver coherent radiation in the $3\text{-}5 \mu\text{m}$ spectral range is given by Quantum Cascade Lasers (QCLs). Their main advantages are the robustness, compactness, long lifetime and very good stability [8]. Even though in the past 20 years QCLs have witnessed an enormous development, they are still limited to watt level average output powers, with the highest power recorded at room temperature of around 5 W at approximately $4.9 \mu\text{m}$ [9, 10]. Better performances can be achieved operating with cryogenic cooling (12 W of output power in [11]). Other drawbacks of such sources are the limited energy and peak power achievable. The small linewidth of their output spectra moreover can be unwanted in applications where broad spectra are required, such as in IRCM. In this field, broad spectra are desirable to be insensitive to counter-counter measures systems.

The last method used commonly in order to obtain high average power in the $3\text{-}5 \mu\text{m}$ domain is through optical frequency down-conversion in nonlinear crystals using optical parametric oscillators (OPOs) [4, 12]. Contrary to the common laser systems, an OPO is frequency tunable over a broad tuning range, depending on the transparency of the material used. Since its theoretical prediction in the early 1960s [13, 14], the OPOs have been widely investigated. The first experimental demonstration by Giordmaine and Miller dates back to 1965 [2]. As nonlinear material they employed lithium niobate pumped by the $1.06 \mu\text{m}$ output of a pulsed $\text{Nd}^{3+}:\text{CaWO}_4$ laser. Since then, the development of OPOs has been accompanied by the improvement of nonlinear crystals and pump sources. At first, the high electric fields necessary for nonlinear conversion hampered the development of practical devices, because of the low optical damage threshold of the nonlinear crystals available. The advent of nonlinear crystals with increased damage threshold in the 1980s prompted OPOs for practical applications. Interest in their development has been further renewed as a consequence of the availability of new nonlinear materials with high nonlinear coefficients [15] and more compact pump sources, e.g., diode pumped solid state lasers, fiber lasers and semiconductor lasers. The interest on the field has been constantly growing, as we can see clearly from the number of publications and citations over time, presented in Fig. 2.2. Nowadays, several research groups are working in this field by exploiting different approaches, depending

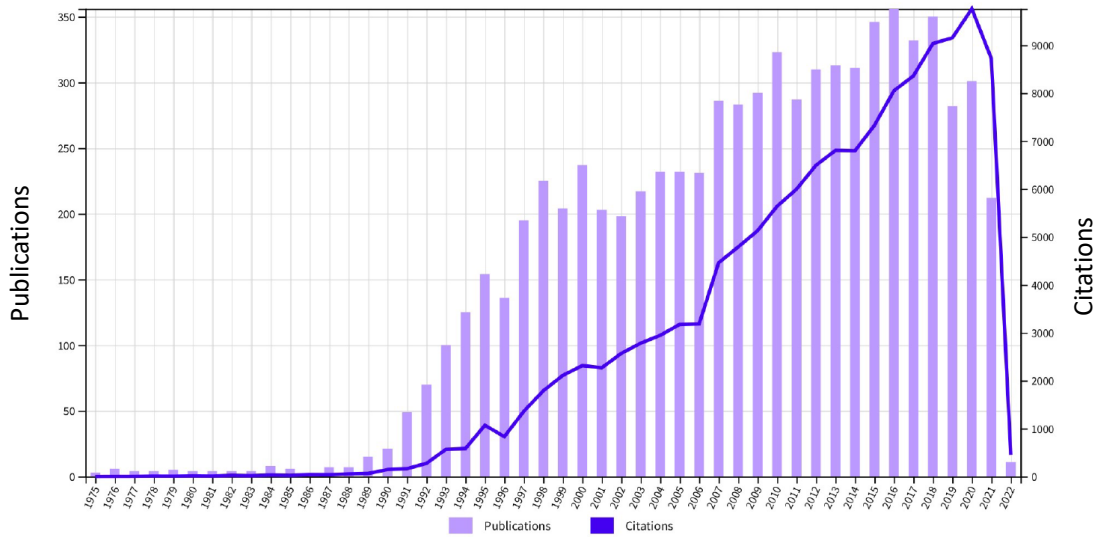


Figure 2.2: Number of publications and citations related to OPOs per year. Image taken from [16].

on the desired output wavelength. OPOs can operate in all temporal regimes, from CW to femtoseconds [17]. When we focus on the possible applications in the mid-IR spectral domain, such as IRCM systems, nanosecond OPOs provide good conditions for the generation of high energy and high average power beams [15]. In such applications moreover, high repetition rate (\sim kHz) is desired to be able to properly modulate the mid-IR beam.

In this thesis we focus on high average power (several tens of watts), high repetition rate (\sim kHz), mid-IR domain generation ($3-5 \mu\text{m}$). In order to achieve it, we will exploit nonlinear conversion in nanosecond OPOs. In the following sections we will summarize the main properties of nonlinear crystals and pump sources that can be used for this purpose.

2.2. Nonlinear crystals

The choice of the nonlinear material plays a crucial role in the operation of the OPO system. This selection is governed by many factors such as broad transparency range, useful birefringence, high nonlinear coefficient d for the process of interest, low spatial (and temporal) walk-off, relatively easy crystal growth and high optical damage threshold. Indeed, if we focus on the mid-IR region, many nonlinear materials fail to satisfy the specifications needed for appropriate OPO application. This lack of suitable nonlinear materials limited at first the practical mid-IR OPOs [15]. There were different possible materials used

at first to achieve good performing OPOs, such as BBO, LBO, KTA and KTP [18, 19]. With the development of the quasi phase-matching (QPM) technique other possibilities, such as periodically poled lithium niobate (PPLN), raised [20]. Most of these nonlinear materials are pumped by Nd-based lasers with wavelengths around $1 \mu\text{m}$ and cover only a fraction of the mid-IR domain, since multi-photon absorption starting around $4 \mu\text{m}$ limits their efficiency at longer wavelengths [15]. This upper limit in the mid-IR spectral domain is common to the used oxide nonlinear crystals. Moreover, materials like PPLN are not suitable to high average power due to their low laser damage threshold. Therefore, in order to reach longer wavelengths and high average power, non-oxide materials have to be used. However, a more complex growth technique is used in order to produce these large size single domain non-oxide crystals. This hampered their development and as a consequence such materials generally exhibit more defects and increased residual losses compared to the best oxide crystals [15]. Thus, in the development of new mid-IR nonlinear crystals, there must be a compromise between a high nonlinearity and properties which favor low losses and high damage threshold. This need for practical materials prompted many studies on different materials and it still does. The most common available nonlinear materials used for mid-IR generation are presented in Fig. 2.3. Their transparency range and nonlinear figure of merit are shown. The figure of merit is defined as d^2/n_p^3 , with d the nonlinear coefficient and n_p linear refractive index at the pump wavelength (dispersion ignored for simplicity). Its definition will be explained in Chap. 3. Very promising nonlinear materials are currently cadmium silicon phosphide (CSP) [22] and orientation patterned GaAs (OP-GaAs) [23]. Both have been used with good results [24, 25, 26]. Concerning CSP, its high nonlinear coefficient and the possibility to be pumped at $1 \mu\text{m}$ make it very suitable for mid-IR generation. However, it is still a relatively new material, therefore it is still difficult to grow crystals with the required quality and dimension to achieve high average output power (in the order of several tens of watts). On the other side, OP-GaAs has proven to be very efficient for mid-IR generation, but high power operation is limited by the thickness of the samples available [27, 21]. In fact, at present, the best candidate for high average power generation in the mid-IR is the zinc germanium phosphide (ZGP) crystal, pumped by a $2 \mu\text{m}$ pump source [21]. Fabricated by Vertical Bridgman technique, its technology is mature enough to growth crystals of large size with very low absorption coefficient at $2 \mu\text{m}$, thanks electron beam irradiation (absorption coefficient below 2 cm^{-1} [28, 29]). The reasons why ZGP is the leading material to generate mid-IR radiation are manifold: its high nonlinear coefficient (75 pm/V), good thermal conductivity ($36 \text{ W m}^{-1}\text{K}^{-1}$) relatively high damage threshold (up to $4\text{-}5 \text{ J/cm}^2$), and its transparency region (between 2 and $8 \mu\text{m}$). Hence, many research groups in the mid-IR OPO community have focused on the implementation of this crystal. The most important results will be discussed in detail afterwards.

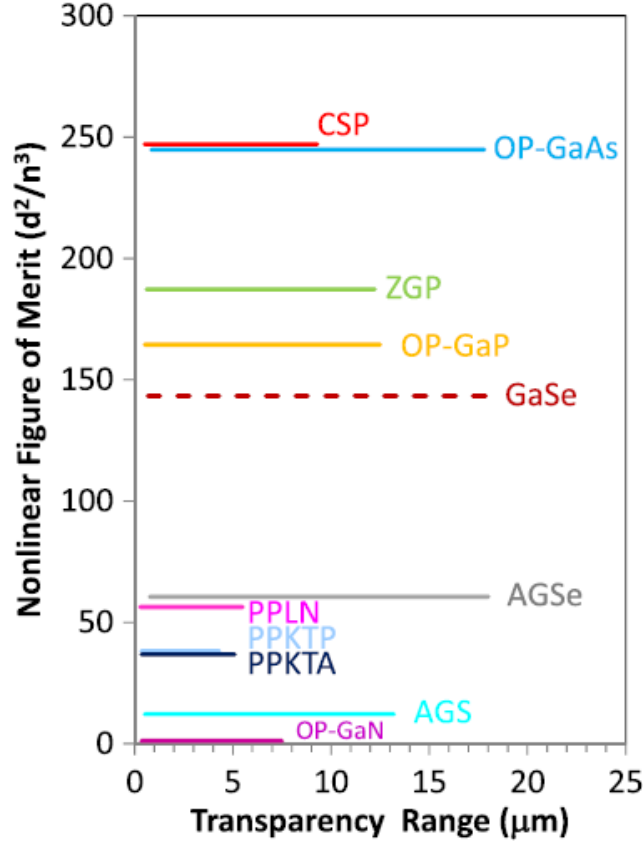


Figure 2.3: Non linear figure of merit (d^2/n_p^3) versus transparency range of various nonlinear crystals. d is the nonlinear coefficient and n_p the linear refractive index at the pump wavelength. Image taken from [21].

In this thesis we use as nonlinear crystal for OPO operation ZGPs from different suppliers. Data concerning this type of crystal is presented in Appendix A and the specific characteristics of the ZGPs used in this thesis will be presented in Chap 4. The main drawback of ZGP is that, due to absorption, it can not be pumped by 1 μm sources, where a wide choice of high average power laser is available. The ZGP requires a pump source emitting at 2 μm . The next section is devoted to overview the different possibilities concerning the pump sources.

2.3. Pump sources

If we consider just high repetition rate operation OPOs, several pump sources operating in the near infrared domain (1 – 2 μm) can be considered. One of the first to be used for OPO generation in the mid-IR was the Ti:Sapphire laser (Ti:Al₂O₃) [30]. It is a solid state laser with broadly tunable output (from 0.67 to 1.1 μm). However, it has as drawback that it must be pumped by another laser

with a wavelength between 514 and 532 nm , where no powerful laser diodes are available. The most common ways to pump it are using Argon-Ion lasers or frequency doubled Nd:based lasers. The average output power of this pump source is typically of several watts. Other possible pump sources used in order to reach the mid-IR spectral domain are diode-pumped Nd:based lasers systems (Nd³⁺:YAG or Nd³⁺:YLF), whose output wavelength are respectively 1064 nm and 1047/1053 nm . They have proven to be efficient tools in order to reach high average output power using KTP and KTA crystals [31, 18].

In order to use the more efficient non-oxide crystals, as mentioned in Sec. 2.2, there have been many studies about 2 μm radiation sources. Using this wavelength has several advantages compared to the more standard 1 μm sources. First, 2 μm is also a wavelength of interest for some applications, such as infrared countermeasures (IRCM). Second, most crystals that can be pumped at 1 μm , absorb wavelengths longer than about 4 – 5 μm , as mentioned in the previous section [32]. Moreover, some nonlinear crystals which are operating very efficiently in the 3-5 μm range, such as ZGP, can not be pumped at 1 μm due to high absorption at that wavelength. Finally, for broadband applications, a 2 μm pump source allows to have both the signal and idler wavelengths in the useful spectral range (3-5 μm). Consequently, in the past years, many studies have focused on increasing the performance of such pump sources, both in output power and beam quality. To emit at this wavelength, the most interesting materials for high power generation are Tm³⁺ and Ho³⁺ doped lasers. Initial work on 2 μm concentrated on thulium-holmium co-doped operation [33]. However, strong up-conversion processes make power scaling of such systems difficult. Therefore, studies have focused on Ho³⁺ lasers that are resonantly pumped by diode pumped Tm³⁺-doped lasers emitting at 1.9 μm . With the emergence of high power Tm³⁺-doped fiber lasers, efficient Ho³⁺:YAG lasers were demonstrated emitting at 2.09 μm [34]. Nowadays, efficient high repetition rate Q-switched Ho³⁺:YAG lasers delivering high power outputs (in the order of hundred of watts) from a single crystal and with good beam quality are available. In 2018 Duan *et al.* obtained 106 W of output power at a repetition rate of 20 kHz with a beam propagation factor of 1.6 [35].

Recently, the interest shifted towards investigating other Ho³⁺ doped laser media emitting at different wavelengths, in order to exploit the lower thermal lens of the laser crystals. Among these, Ho³⁺:LLF and Ho³⁺:YLF are very promising crystals. Their output wavelength (2.05/2.06 μm) makes them suitable for ZGP pumping. A comparison of the performance of these two materials under identical pump condition was done at ISL [36]. As result, the threshold, slope and optical-to-optical efficiency of the Ho³⁺:LLF were up to 10 % better than the Ho³⁺:YLF in CW operation. However, the two lasers behaved nearly identically in Q-switched mode at low repetition rate operation. In 2012, at ISL, Schellhorn *et al.* developed an Ho³⁺:LLF Master Oscillator Power Amplifier (MOPA) system operating at low repetition rate (100 Hz) with a nearly diffrac-

tion limited beam quality ($M^2 = 1.03$) and an optical-to-optical efficiency of 12.9% [37]. Fonnum *et al* instead demonstrated a low repetition rate (1 Hz) cryogenic Ho^{3+} :YLF oscillator [38]. Their system delivers up to 550 mJ per pulse with a beam quality factor of 1.5. Recently, high average power of the order of tens of watts with almost diffraction limited beam quality have been demonstrated from both Ho^{3+} :LLF [39] and Ho^{3+} :YLF lasers [40].

Besides solid-state lasers, fiber lasers are also attractive pump sources for mid-IR OPOs, due to their compactness. At ISL, 195 W of average output power at $2.09 \mu\text{m}$ in CW have been demonstrated using a Tm^{3+} , Ho^{3+} codoped fiber laser, with the possibility of further power scaling [41]. The output presented a good stability and slope efficiency (44.8 %), with an almost diffraction limited beam quality factor $M^2 = 1.08$. If we focus on the pulsed regime, high average power (several tens of watts) at $2 \mu\text{m}$ have been demonstrated, both with MOPA designs [42] and single oscillators [43, 44].

Fiber pump sources have proven to be effective in OPO pumping, although limited to watt level powers in the mid-IR. The first mid-IR OPO pumped directly by a pulsed fiber laser was demonstrated in 2008 by Creeden *et al.*[45]. In their work, they used a Tm^{3+} -doped fiber laser to pump a ZGP OPO, obtaining 658 mW in the mid-IR (2.9 W pump power). At ISL, 8.1 W from a ZGP OPO have been demonstrated in 2019 [46]. The most recent demonstration of a fiber laser mid-IR OPO comes from Holmen and Fonnum in 2021 [47]. Using 5.1 W from an Ho^{3+} -doped fiber laser at 10 kHz, they obtained 3 W from a ZGP OPO.

The pump source used in this thesis is an Ho^{3+} :LLF MOPA laser. Its details have been presented in [39], but an overview of its performances will be given in Chap. 4.

2.4. Optical parametric oscillators based on ZGP

As mentioned in Sec. 2.2, this thesis focuses on ZGP based, high repetition rate, high average power OPOs. In this section an overview of the current state of the art of such devices is given, highlighting the advantages and drawbacks of the different resonator geometries implemented.

In principle, high power can be achieved by the use of a Master Oscillator Power Amplifier (MOPA) architecture. The highest average power currently reported is a two-stage ZGP MOPA [48]. Its experimental setup is presented in Fig. 2.4. The pump source was a 20 kHz pulse repetition Ho^{3+} :YAG MOPA system. The mid-IR output power after the amplification stage was 161 W, with an $M^2 \approx 3.6$. However, as we can see from the figure, MOPA systems are relatively complex. If we take into account the size of the pump source, the overall system can be unwieldy. Even for applications where compactness is not required, it is valuable to investigate the first single stage OPO before the amplification stage. Few experimental single-stage, high power sources reaching tens of watts have

been demonstrated, but many suffered from limited stability or unsatisfying beam quality.

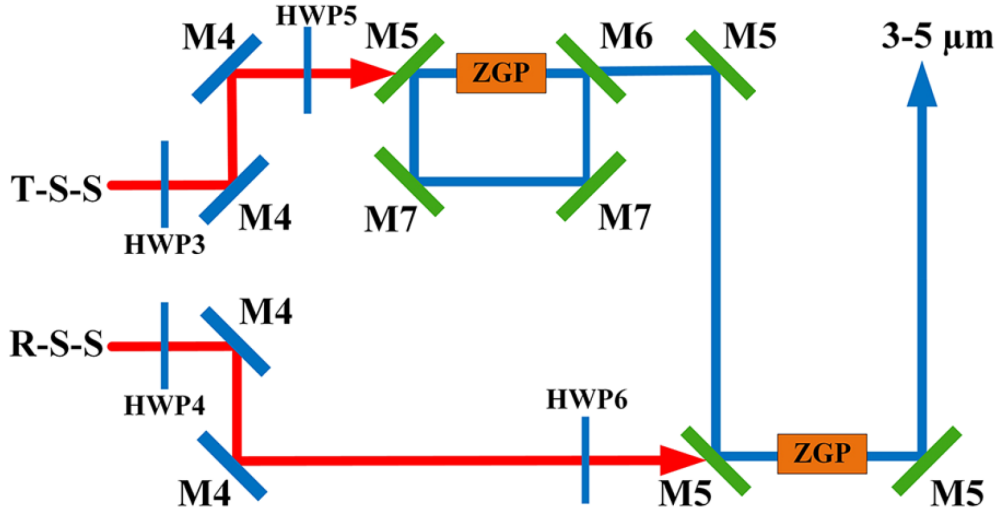


Figure 2.4: OPO experimental setup of [48].

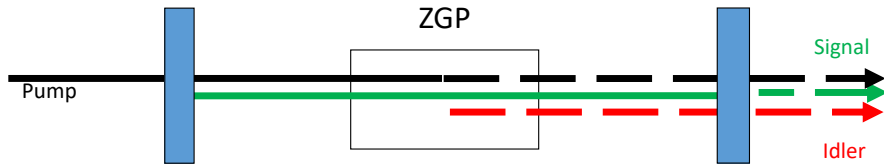


Figure 2.5: Linear OPO experimental setup.

The simplest possible approach to implement a single stage OPO is to use a linear resonator of two flat mirrors, as depicted in Fig. 2.5. This cavity design has been used to achieve good performances in the past. In 2009, Elder demonstrated an Ho^{3+} :YAG pumped ZGP OPO producing 12.6 W of output power in the 3 – 5 μm domain [49]. The beam quality factor M^2 of this output was 2.7. Using a ZGP linear resonator with two ZGP in series, Hemming *et al.* demonstrated 27 W output power with a M^2 of 4 in 2013 [50]. Their setup consists of a pair of thulium fiber laser pumping two rod Ho^{3+} :YAG laser oscillators as OPO pump source. The main drawback of this system was the thermal lensing in the ZGP at high power. Its effect limited the performances of the OPO, especially degrading the beam quality. Moreover, they used an optical isolator to avoid problems of back-reflection into the pump source. This limits the power scalability of the system, since commercially available isolators are power-limited at approximately 40 W. Further attempts to improve the performances of OPOs based on such design have clashed with back-reflection problems and beam

quality control. In this regard it is worth to mention the result achieved by Wang *et al.* in 2017 [51]. They reached a optical-to-optical conversion efficiency of 75.7 %. In order to achieve such a result, they designed a double pass pumped high gain OPO and a matched large sized high peak power pump beams to suppress spatial walk off and back conversion. However, the measured M^2 of the output beam was 9.6.

As these studies demonstrated, the main challenge in the development of high average power OPOs is to maintain the good beam quality with a simple and compact architecture. The beam quality of the generated beams tends to be lower than the one of the pump beam due to thermal effects in the crystal, induced by the unwanted pump absorption, as well as possible spatial walk-off between the pump and the generated beams. In principle, the mode discrimination of the OPO could be improved by increasing the OPO resonator length [52], but this would lead to reduced efficiency due to a longer signal buildup time, and would result in an increased system size. Another possibility is to use different cavity designs. The first option, due to its simplicity, would be to use a planar ring cavity resonator, presented in Fig. 2.6.

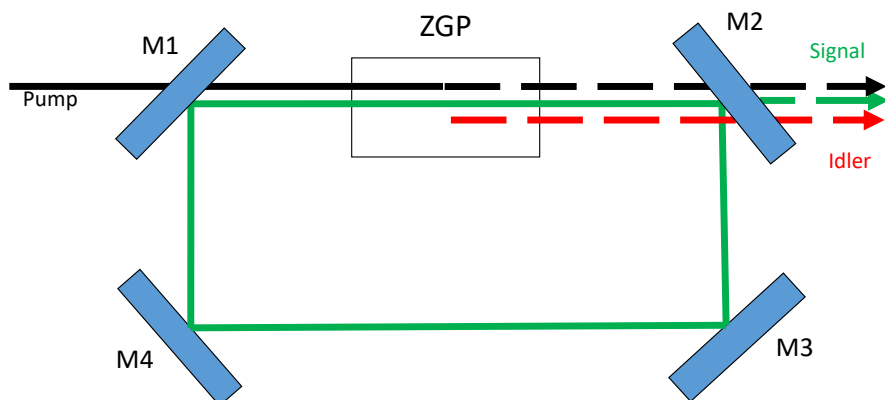


Figure 2.6: Planar ring OPO resonator setup.

This kind of resonator eliminates the problem of back-reflection into the pump source, allowing to reach higher powers. In this cavity arrangement, with two separate ZGP crystals placed in series, 41 W with $M^2 = 4.4$ was reported by Yao *et al.* in 2014 [53]. The same group demonstrated in 2018 the highest average power with such a setup, reaching 110 W [54], but the beam quality at 100 W was very poor ($M^2 \approx 9$), and the operation at maximum output power lasted only few seconds before crystal damage. An $M^2 \approx 4$ for stable operation was reported at 30 W [54]. The ring cavity approach allows to reach high output power in the mid-IR but it usually presents problems concerning the thermal lensing control inside the nonlinear crystal. Therefore the beam quality is usually not optimal. Attempts to improve the beam quality include thermal lens compensation by an intracavity lens. This method was used to demonstrate a

102 W MOPA system with an M^2 factor of 2.8 [55]. After the first OPO stage the output power was 28 W ($M^2 = 2.1$).

To assess the problem of beam quality, in recent years some innovative ring cavity resonator designs have been implemented. In 2010 Lippert *et al.* presented a 22 W mid-IR ZGP OPO with a V-shaped three-mirror ring resonator [56]. It is presented in Fig. 2.7.

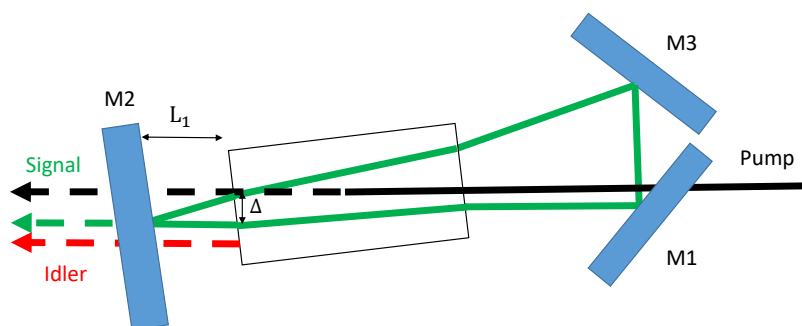


Figure 2.7: Scheme of the OPO V-shaped resonator used in [56].

With this configuration, they measured a beam quality factor of 1.4 and found indications of further power scalability. Since the two beams pass in the crystal do not overlap, the damage threshold, in terms of the maximum allowable pump fluence, is significantly higher than for a standing wave resonator and the thermal lensing is also reduced. However, in order to obtain good performances, the separation distance Δ must be at least of the order of the beam diameter. This means that the angle between the two long resonator arms and the distance L_1 from the output coupler (OC) mirror to the crystal can not be too small, hampering the scalability of the system footprint. In their experimental setup, the round trip time of the pump source matched the round-trip time of the OPO. When this was not the case reducing the OPO resonator length resulted in an increase of the threshold power, although the slope efficiency did not change.

Another method to improve the beam quality is given by the image rotation technique [57]. In particular, two OPO cavities based on this method were designed in the past. The first is called Rotated Image Singly-Resonant Twisted RectAngle (RISTRA) cavity and it was presented in 2002 by Smith *et al.* [58]. The second type was developed at ISL and it is called Fractional Image Rotation Enhancement (FIRE) cavity [59]. Their working principle and mirror configuration will be presented in Chap. 3. These cavities have proven their effectiveness and advantages over planar resonators in many OPO demonstrations with improved beam quality [60, 61]. However, most of the previous studies dealt with low repetition, high energy pump sources and focused on increasing pulse energy in cases where high Fresnel number is required due to crystal damage

constrains [62]. A deep investigation of the performances of such cavities at high repetition rate and high average power has never been carried out.

An overview of the performances of the mid-IR OPOs presented in this section is given in Tab. 2.1.

Author	Year	P_{max} [W]	M^2	Pump rep. rate [kHz]	Resonator type	Reference
Liu et al.	2021	161	3.6	20	OPO-OPA system	[48]
Qian et al	2019	102	2.1	10	OPO-OPA system with intra-cavity lens	[55]
Zhao et al.	2018	110	8 (at 100 W)	10	Planar ring	[54]
Yao et al.	2014	41	4.4	20	Planar ring	[53]
Hemming et al.	2013	27	4.4	35	DR linear cavity	[50]
Lippert et al.	2010	22	1.4	45	V-shaped cavity	[56]

Table 2.1.: Resume of high average power ZGP OPO performances.

In this thesis, different OPO cavity resonator are used. In particular, linear, RISTRA and FIRE cavities are implemented and studied. Their characteristics will be presented in detail in Chap. 4.

3. Theory

In this chapter, we consider the main theoretical aspects involved during optical parametric oscillation that are relevant to this thesis. After a brief introduction on the nonlinear optical processes, taken mostly from [63], we will focus on the second order non linearity ones. We will present different relevant aspects such as phase-matching, parametric gain and the coupled wave equations between the interacting electric fields. Afterwards, we will focus on optical parametric oscillators (OPOs) operating in the nanosecond regime, introducing the different resonant regimes and the oscillation threshold. We will then introduce quickly the two non-planar ring cavities used in this thesis.

Finally, a brief introduction on the characterization of laser sources is presented, with a particular attention on the definition of beam quality of a laser beam and on the factors affecting it during operation (thermal lensing and gain guiding).

3.1. Optical parametric generation

Usually, most optical phenomena of every day life can be described by linear equations. The electromagnetic field induces a dipole momentum in the dielectric material. These dipole moments per unit of volume are called polarization density $\vec{P}(t, r)$, which is proportional to the electric field:

$$\vec{P}^L(r, t) = \epsilon_0 \chi \cdot \vec{E}(r, t) \quad (3.1)$$

where ϵ_0 is the permittivity of vacuum, $\vec{E}(r, t)$ is the electric field and χ is called electric susceptibility. However, if the electric fields involved are sufficiently strong, the induced polarization will no longer be proportional to the electric field. The nonlinear properties of the material are described by expanding the dependence of the polarization density on the electric field into a series of higher order terms:

$$\vec{P} = \epsilon_0 \left[\chi^{(1)} \cdot \vec{E} + \chi^{(2)} \cdot \vec{E} \cdot \vec{E} + \chi^{(3)} \cdot \vec{E} \cdot \vec{E} \cdot \vec{E} + \dots \right] = \vec{P}^L + \vec{P}^{NL} \quad (3.2)$$

where the terms $\chi^{(2)}$ and $\chi^{(3)}$ are the second and third order nonlinear electric susceptibilities tensors, $\chi^{(1)}$ is the linear electric susceptibility, \vec{P}^L denotes the linear part of the polarization, and \vec{P}^{NL} the non linear part. The terms of

order greater than three are neglected in the present work due to their relative weakness. It is worth to mentioned that in a centrosymmetric medium, the term $\chi^{(2)} = 0$ [64]. Thus, often the third term in the nonlinear series is the most important one. However, many materials present a non-zero second order non linearity. In this thesis we will focus on these materials, which cause a three wave interaction in the medium via the polarization density. We consider the amplitude of a superposition of monochromatic plane waves. For example, we can consider as input an optical field given by the sum of two waves at circular frequencies ω_1 and ω_2 :

$$\vec{E}(r, t) = \vec{E}_1(r)e^{-i\omega_1 t} + \vec{E}_2(r)e^{-i\omega_2 t} + c.c. \quad (3.3)$$

where c.c. denotes the complex conjugate. Substituting it in Eq. 3.2, the second term can be expressed as [65]:

$$\begin{aligned} \vec{P}_2^{NL} = \epsilon_0 \chi^{(2)} [& \vec{E}_1^2(r)e^{-2i\omega_1 t} + \vec{E}_2^2(r)e^{-2i\omega_2 t} + 2\vec{E}_1(r)\vec{E}_2(r)e^{-i(\omega_1+\omega_2)t} \\ & + 2\vec{E}_1(r)\vec{E}_2^*(r)e^{-i(\omega_1-\omega_2)t} + c.c.] + 2\epsilon_0 \chi^{(2)} [\vec{E}_1(r)\vec{E}_1^*(r) + \vec{E}_2(r)\vec{E}_2^*(r)] \end{aligned} \quad (3.4)$$

We can notice how the quadratic polarization \vec{P}_2 is responsible for many interesting effects. The two electric fields \vec{E}_1 and \vec{E}_2 interact with the polarization densities and with themselves, causing different types of frequency conversion processes. The first two terms represent the second harmonic generation processes of each of the two waves (SHG). It can be interpreted as two equal photons that merge to form one of double frequency. The third term is the sum frequency generation (SFG), in which the two photons combine into one photon of frequency $\omega_3 = \omega_1 + \omega_2$. The fourth term describes instead the difference frequency generation (DFG), where the generated photon has a frequency given by the difference of the two interacting ones. The last term contains a static polarization density component called optical rectification (OR). An overview of the different processes is given in Tab. 3.1, each one related with the corresponding term of Eq. 3.4.

Expansion term	Nonlinear process	Abbreviation
$\epsilon_0 \chi^{(2)} \vec{E}_1^2 e^{-2i\omega_1 t} + c.c.$	Second harmonic of ω_1	SHG
$\epsilon_0 \chi^{(2)} \vec{E}_2^2 e^{-2i\omega_2 t} + c.c.$	Second harmonic of ω_2	SHG
$\epsilon_0 \chi^{(2)} \vec{E}_1 \vec{E}_2 e^{-i(\omega_1+\omega_2)t} + c.c.$	Sum frequency between ω_1 and ω_2	SFG
$\epsilon_0 \chi^{(2)} \vec{E}_1 \vec{E}_2^* e^{-i(\omega_1-\omega_2)t} + c.c.$	Difference frequency between ω_1 and ω_2	DFG
$\epsilon_0 \chi^{(2)} [\vec{E}_1 \vec{E}_1^* + \vec{E}_2 \vec{E}_2^*].$	Optical rectification	OR

Table 3.1.: List of different nonlinear processes.

Usually, the nonlinear coefficients $d = \chi^{(2)}/2$ are used. Their definition is linked

to the dielectric axes X, Y, Z [66], making it very useful. Moreover, usually only few terms in the tensor d are relevant. Therefore, it is preferred to use an effective nonlinear coefficient d_{eff} , which accounts for the specific components of $\chi^{(2)}$ involved in the interaction.

The process in which an input photon with high frequency, called *pump*, interacts with the quantum noise splitting in two photons of lower energies is called spontaneous down-conversion. The generated beams are called *signal* and *idler*, with conventionally $\omega_s \geq \omega_i$. If the inputs are two light beams (pump and one between signal and idler), one of the generated beams beam will be amplified by the process, which is called optical parametric amplification (OPA). If an optical resonator is then used to enhance the efficiency of the conversion, the device is known as optical parametric oscillator (OPO). This thesis will focus on all of these processes.

3.1.1. Phase-matching

Considering the photon interaction in the transparency range of a material, there are two main restrictions in an optical parametric process: energy and momentum conservation of the implied photons. The first one can be expressed as:

$$\hbar\omega_p = \hbar\omega_s + \hbar\omega_i \quad (3.5)$$

Among all the frequencies which obey to Eq. 3.5, all of them will be generated, but only the one whose wave vectors fulfill the momentum conservation $\hbar\vec{k}_p = \hbar\vec{k}_s + \hbar\vec{k}_i$ can be effectively detected. This is called phase-matching (PM) condition. The phase-mismatch $\Delta\vec{k} = \vec{k}_p - \vec{k}_s - \vec{k}_i$ can be obtained in collinear or noncollinear configuration, depending on whether the wave vectors are parallel between each other or not. The conservation laws are represented in Fig. 3.1. In the collinear case, which is generally more efficient and convenient for practical aspects, one can write:

$$\Delta k = k_p - k_s - k_i = \frac{\omega_p n_p(\omega_p)}{c} - \frac{\omega_s n_s(\omega_s)}{c} - \frac{\omega_i n_i(\omega_i)}{c} = 0 \quad (3.6)$$

where k_j is the wave vector of the j-th optical wave, n_j is the corresponding refractive index, and c is the speed of light in vacuum. Mainly, two techniques can be used to achieve the condition $\Delta k = 0$. The first one, called birefringent phase-matching (BPM), is to exploit the different refractive indices along the different crystal axes in birefringent crystals. In case that BPM is not efficient enough, quasi phase-matching (QPM) can sometimes be used. The second uses a periodical flip of the $\chi^{(2)}$ tensor [13]. In this thesis, only the BPM approach will be considered.

The refractive indices depend on many factors, such as temperature, orien-

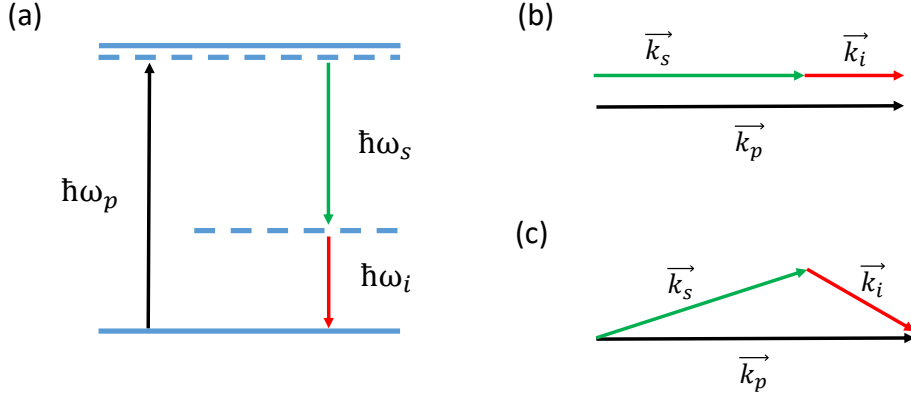


Figure 3.1: Conservation laws in an OPA process. (a) Energy conservation. (b) Momentum conservation: collinear phase-matching. (c) Momentum conservation: noncollinear phase-matching.

tation of the crystal axes, pressure etc. Therefore, fulfillment of Eq. 3.6 can be achieved for different frequencies, giving to the OPA process the ability to continuously tune its output wavelengths. The two main approaches to do it are by temperature tuning (non-critical PM) and by changing the angle between the interacting waves and the crystal axes (critical PM). Although in some of our experiments the temperature is not kept constant (see Chap. 5), in this thesis the OPO is achieved by critical phase-matching. BPM can be done if the interacting waves have different polarization with respect to the dielectric axes. In uniaxial crystals, like ZGP, light polarized in the plane spanned by the optical axis is called extraordinarily polarized, while light polarized perpendicular to it is called the ordinarily polarized. The different refractive indices along the different dielectric axes can be exploited to achieve phase-matching. We denote the polarization of the waves using the letters o and e for ordinary and extraordinary polarization, respectively. Three types of birefringent phase-matching can be distinguished. In type I, the signal and idler have the same polarization but different from the pump. In the notation $p \rightarrow s + i$:

$$o \rightarrow e + e \text{ or } e \rightarrow o + o \quad (3.7)$$

While in type II or type III they have orthogonal polarization:

$$o \rightarrow e + o \text{ or } o \rightarrow o + e, \quad (3.8)$$

$$e \rightarrow e + o \text{ or } e \rightarrow o + e$$

A typical tuning curve of the output wavelengths as a function of the phase-matching angle with respect to the dielectric axis for a type I ZGP pumped by a $2.065 \mu\text{m}$ source is presented in Fig. 3.2. The temperature was considered to be

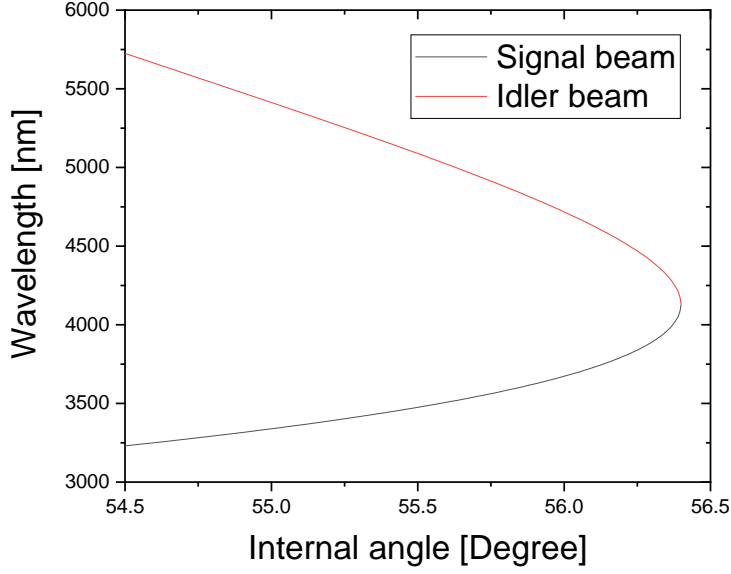


Figure 3.2: Tuning curve for a type I ZGP as function of the angle with respect to the crystal axis at 300° K. Simulation done with SNLO [67].

300° K. The degeneracy is at 56.4°, with $\lambda = 4.13 \mu\text{m}$ [67].

Choosing the angle with respect to the crystal axis can produce an unwanted effect known as Poynting vector walk-off, or simply walk-off. The direction of the energy flow is given by the Poynting vector $\vec{S} = \vec{E} \times \vec{H}$, with \vec{H} being the magnetic field, while the direction of the phase front is given by the \vec{k} vector, which is $(\vec{E} + \vec{P}/\epsilon_0) \times \vec{H}$. The polarization density \vec{P} is only parallel to the electric field \vec{E} if it oscillates along a principal dielectric axis of the crystal. Therefore, generally the Poynting vector is tilted at an angle with respect to \vec{k} , called walk-off angle. Therefore, the spatial overlap will decrease with the propagation of the waves, the conversion will be reduced and the beam profiles will be distorted.

3.1.2. Coupled wave equations

To describe the interaction between the three waves involved in a second order optical parametric process, we have to start from the Maxwell's equations. We consider a dielectric material with no free charges nor free currents. Accounting for the non linearity of the polarization, we obtain for each electric field:

$$\nabla^2 \vec{E}_j = \frac{n^2}{c^2} \frac{\partial^2}{\partial t^2} \vec{E}_j + \mu_0 \frac{\partial^2}{\partial t^2} \vec{P}_j^{NL} \quad (3.9)$$

where μ_0 is the vacuum permeability and $j = p, s, i$. For simplicity, we consider for the electric fields in 3.3 the case where the direction of propagation of the plane waves is in the positive z direction:

$$E_j(r, t) = A_j(z)e^{-i(\omega t - kz)} + c.c. \quad (3.10)$$

with $A_j(z)$ the complex amplitudes. In order to solve the problem, we consider field amplitudes slowly varying over distances compared to the wavelengths, $d^2A_j(z)/dz^2 \ll k_j dA_j(z)/dz$. Neglecting these second spatial derivatives, we then obtain the following set of coupled wave equations for the pump, signal and idler:

$$\frac{dA_p(z)}{dz} = \frac{2i\omega_p d_{eff}}{n_p c} A_s(z) A_i^*(z) e^{-i\Delta k z} \quad (3.11)$$

$$\frac{dA_s(z)}{dz} = \frac{2i\omega_s d_{eff}}{n_s c} A_p(z) A_i^*(z) e^{i\Delta k z} \quad (3.12)$$

$$\frac{dA_i(z)}{dz} = \frac{2i\omega_i d_{eff}}{n_i c} A_p(z) A_s^*(z) e^{i\Delta k z} \quad (3.13)$$

where d_{eff} is the effective nonlinear coefficient. The coupled equations describe how energy is exchanged between each different field and polarization density. As they propagate along the nonlinear medium, the each field exchanges energy with the correspondon polarization density depending on the relative phase. Under suitable conditions, the frequency down-conversion can continue until the power is completely transferred from the strong pump field to the initially weak signal and idler. If the pump is totally depleted and converted, it is regenerated from sum frequency generation of the signal and idler. This phenomenon is called back-conversion. It can occur even before total pump depletion and it reduces the OPO conversion efficiency. The amplification factor can be obtained by the coupled wave equations, which can be solved analytically under some approximations.

3.1.3. Parametric gain

Usually, an OPO starts from random quantum noise which is then amplified. We can assume as initial approximation that the pump does not undergo strong depletion. This equals to consider $dA_p(z)/dz = 0$ in Eq. 3.11. The coupled wave equations are therefore reduced to two. If we consider no input idler field and a non-vanishing initial signal amplitude $A_s(0)$, the parametric amplification of

the signal power is [68, 63]:

$$G_s(L) = \frac{I_s(L)}{I_s(0)} - 1 = \Gamma^2 L^2 \frac{\sinh^2 \sqrt{\Gamma^2 L^2 - \left(\frac{\Delta k L}{2}\right)^2}}{\Gamma^2 L^2 - \left(\frac{\Delta k L}{2}\right)^2} \quad (3.14)$$

where $I_s(z)$ is the field intensity, L is the interaction length and Γ is the gain factor, defined as (neglecting the walk-off):

$$\Gamma^2 = \frac{8\pi^2 d_{eff}^2}{c\epsilon_0 n_p n_s n_i \lambda_s \lambda_i} I_p(0) = K I_p(0) \quad (3.15)$$

with K called coupling constant. Similar results can be derived if we consider the case of non-zero input idler [69]. The amplification factor $G_s(L)$ is dependent on many factors. Among them, the strongest dependence is on the phase mismatch Δk . The maximum gain occurs when $\Delta k = 0$ and then quickly decreases for increasing phase mismatch. If we consider a fixed mismatch Δk , the intensities of the signal and idler waves increase to their maximum values periodically. The length at which this occurs is called coherence length $L_c = \pi/\Delta k$. For lengths greater than L_c , spatial oscillations occurs with a period of $2\pi/\Delta k$. In practical cases, we have $\Delta k \approx 0$, hence:

$$G_s(L) = \sinh^2(\Gamma L) \quad (3.16)$$

From Eq. 3.14 it can be noticed that the gain is also given by a number of material parameters such as the refractive indices and nonlinear coefficient. Because of this, for practical use, it is worth to define the so-called nonlinear figure of merit F :

$$F = \frac{d_{eff}^2}{n_p n_s n_i} \quad (3.17)$$

Its definition includes all the fundamental material parameters and it is widely used when comparing nonlinear crystals, as seen in Fig. 2.3.

Up to now, we have not distinguished between the different possible temporal regimes. In this thesis we will focus on OPOs operating in the nanosecond regime. General considerations for this particular case will be presented in the next section.

3.2. Optical parametric oscillators

In Sec. 2.1 we have mentioned that in order to achieve high power in the mid-IR spectral range, ns pulsed OPOs are suitable sources. In this section we will

focus on such devices.

An OPO is a device where frequency down-conversion is obtained in a non-linear crystal, which is placed in a resonant cavity. If the amplification of the resonant waves is equal or greater than the losses of the resonator, the oscillation threshold is reached, and the signal and idler waves grow dramatically. The main causes of the losses are the transmission of the mirrors, absorption of the crystal and coatings, and scattering losses. Different configurations can be built, as shown in Fig. 3.3.

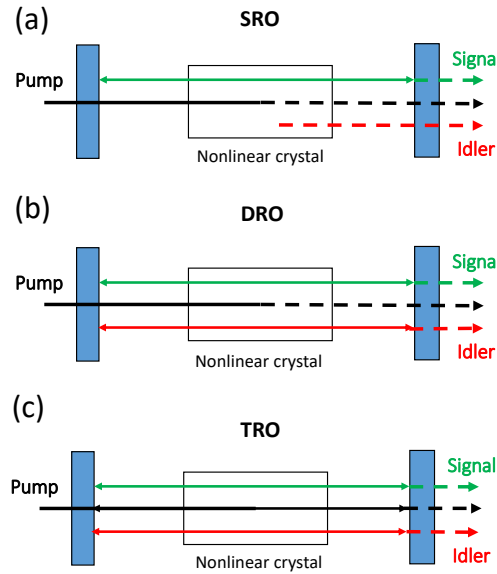


Figure 3.3: Different OPO configuration. (a) Singly resonant oscillator. (b) Doubly resonant oscillator. (c) Triply resonant oscillator.

The simplest one is the singly resonant oscillator (SRO), when only one wave is partially reflected by all mirrors (usually the signal). If the idler is resonating too, it is called doubly resonant oscillator (DRO). In both types of cavities, amplification only takes place when signal and pump co-propagate, as only then phase-matching is possible. These cavities can be built in double pump pass configuration, when the pump beam is reflected by the output coupler, giving rise to amplification in both directions of propagation. It is also possible to build a triply resonant oscillator (TRO), in which the pump is resonating at the same time. However, this last configuration is usually very unstable and requires an active stabilization cavity method. In this thesis only SRO and DRO configurations have been used.

The OPO has some similarities with lasers. First of all, a gain material is placed in a resonator cavity. They both have an oscillation threshold and emit coherent output beams. Contrarily to the laser however, in the OPO no energy

is stored in the crystal, since a pump photon is converted instantaneously into a pair of signal and idler photons. In addition, the phase of the output beams of an OPO are correlated to the phase of the pump, while in a laser they are not.

3.2.1. Frequency selection

Let us now consider more in detail the tuning characteristics of an OPO, which are very different between the singly and doubly resonant cases. The main factor that affects the coarse tuning properties of an OPO is the phase-matching, although cavity longitudinal modes have a major role in determining the details of frequency tuning. The parametric gain, defined in Eq 3.14, is usually much wider than the cavity mode spacing and cavity resonance width, so many cavity modes lie beneath the gain profile of an OPO [64].

The selection of signal and idler frequencies in a singly resonant cavity is relatively simple: oscillation occurs on the cavity mode closest to the peak of the gain curve. The case of doubly resonant cavities is more complex. In addition to obey the energy conservation law (Eq. 3.5), the signal and idler must also be simultaneously resonant in the cavity. However, due to dispersion, they have different cavity longitudinal mode frequency spacings, as represented in Fig. 3.4.

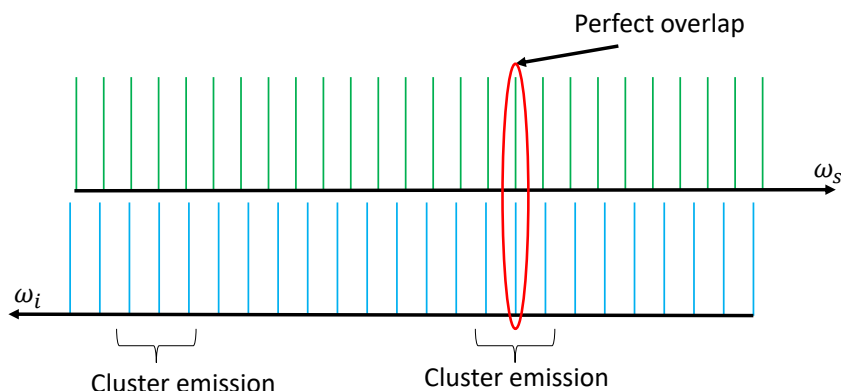


Figure 3.4: Symbolic representation of the frequency comb mode structure of a doubly resonant OPO.

The condition of simultaneous resonance occurs only at intervals of frequencies, called cluster frequencies [70]. To find the frequency distance between two clusters, we have first to define the signal and idler longitudinal modes numbers [70]:

$$m_s = \frac{2L_{opt}}{\lambda_s} = \frac{\omega_s}{\pi c} (L - l + ln_s) \quad (3.18)$$

$$m_i = \frac{2L_{opt}}{\lambda_i} = \frac{\omega_i}{\pi c} (L - l + ln_i) \quad (3.19)$$

where $2L_{opt}$ is the optical length of a cavity round-trip, L is the physical length of the cavity and l is the crystal length. The free spectral ranges of the signal/idler resonance $\delta\omega_s$ and $\delta\omega_i$, are the frequencies that change the respective mode number by one:

$$\frac{\partial m_s}{\partial \omega_s} = \frac{l}{\pi c} \left(n_s + \omega_s \frac{\partial n_s}{\partial \omega_s} \right) + \left(\frac{L-l}{\pi c} \right) = \delta\omega_s^{-1} \quad (3.20)$$

$$\frac{\partial m_i}{\partial \omega_i} = \frac{l}{\pi c} \left(n_i + \omega_i \frac{\partial n_i}{\partial \omega_i} \right) + \left(\frac{L-l}{\pi c} \right) = \delta\omega_i^{-1} \quad (3.21)$$

Generally, there are hundreds of cavity axial modes between two cluster frequencies. If we consider the sum of mode numbers $m = m_s + m_i$, the signal frequency separation of adjacent clusters Ω_s can be obtained by second order approximation [70]:

$$\Delta m = \pm 1 = \left(\frac{\partial m}{\partial \omega_s} \right) \Omega_s + \frac{1}{2} \left(\frac{\partial^2 m}{\partial \omega_s^2} \right) \Omega_s^2 \quad (3.22)$$

Away from degeneracy, we can consider only the first order term, obtaining:

$$\Omega_s = \pm \left(\frac{\partial m}{\partial \omega_s} \right)^{-1} = \left[\frac{l}{\pi c} \left(n_s - n_i + \omega_s \frac{\partial n_s}{\partial \omega_s} - \omega_i \frac{\partial n_i}{\partial \omega_i} \right) \right]^{-1} \quad (3.23)$$

where the minus sign comes from the energy conservation: from Eq. 3.5, if we consider the $\omega_p = \text{constant}$, as the ω_s increases, ω_i must decrease. This cluster separation is usually $\Omega_s \sim \text{THz}$, as calculated and measured in [56]. This correspond to approximately 50 nm in the wavelength regime (at around 3.8 μm). Usually, only few clusters (two or three) are within the gain bandwidth [70].

3.2.2. Non-planar ring cavities

In a resonator, it is of advantage to construct a short cavity to have a low threshold. Moreover, usually large beam diameters (few millimeters) are used to avoid coating damages. This conditions leads to a large cavity Fresnel number $N_F = d^2/\lambda L$, where d is the beam diameter and L the geometrical cavity length. This causes a low cavity transverse-mode discrimination and thus a low beam quality [71]. To overcome this problem, two particular non-planar ring cavities have been designed in the past years. They are both used in this thesis. Their specific characteristics (resonant regime, cavity length etc.) will be presented in Chap. 4. A complete theoretical examination of these two cavities is beyond the scope of this thesis and can be found in their original publica-

tions [58, 59]. Nevertheless, a brief description of the theory of image rotation technique is presented below.

The first non-planar ring cavity is the Rotated Image Singly-resonant Twisted RectAngle (RISTRA) cavity, presented in 2002 by Smith *et al.* [58, 72]. Its scheme is presented in Fig. 3.5 (a). To understand its working principle, let's consider first the image rotation created by the reflection at two flat mirrors M_1 and M_2 , as represented in Fig. 3.6. We consider the Z axis always lying in the propagation direction, while Y lies in the plane of incidence. An image point with coordinates (x, y) in the coordinate system $[X, Y]$ will be transformed after the reflection of the first mirror in the new frame $[X', Y']$:

$$\begin{pmatrix} x' \\ y' \end{pmatrix} = M \begin{pmatrix} x \\ y \end{pmatrix} \quad (3.24)$$

where M denotes the matrix of the mirror transformation:

$$M = \begin{bmatrix} 1 & 0 \\ 0 & -1 \end{bmatrix} \quad (3.25)$$

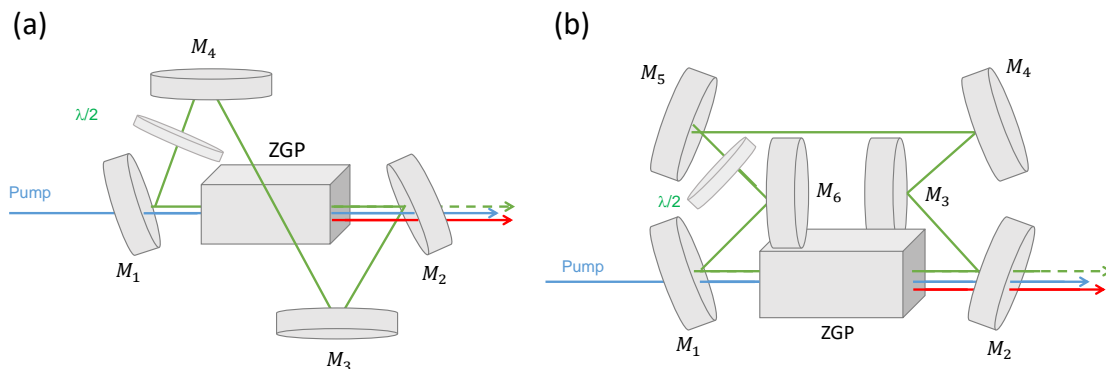


Figure 3.5: The two non-planar cavities studied in the thesis. (a) RISTRA. (b) FIRE.

Before treating the second reflection at M_2 , it must be noted that the planes of incidence between the two mirrors are tilted between each other by an angle γ . We must thus transform to the reference frame $[X'', Y'']$:

$$\begin{pmatrix} x'' \\ y'' \end{pmatrix} = R \begin{pmatrix} x' \\ y' \end{pmatrix} \quad (3.26)$$

where the rotational matrix R is defined by:

$$R = \begin{bmatrix} \cos\gamma & \sin\gamma \\ -\sin\gamma & \cos\gamma \end{bmatrix} \quad (3.27)$$

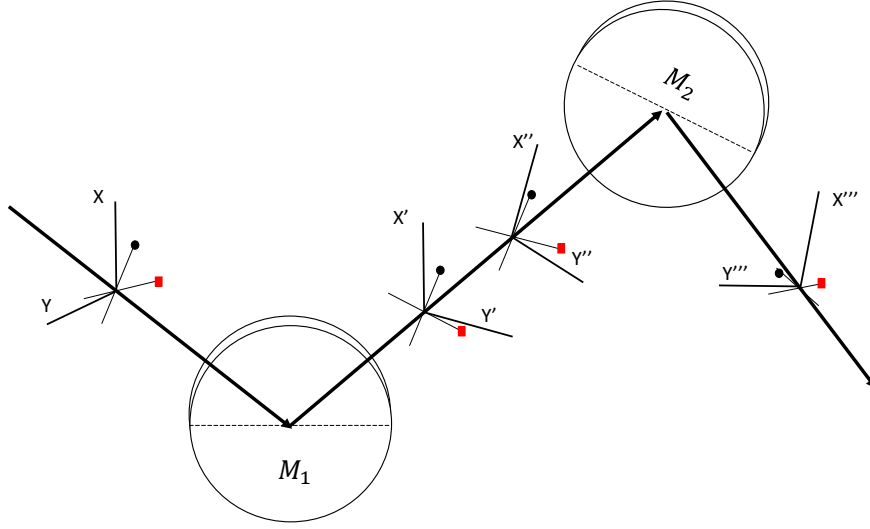


Figure 3.6: Reflection of a beam on two mirrors. The reference frames are labeled X and Y. The image is represented by the colored pins. Image adapted from [58].

Therefore, after the second reflection, the total transformation from the initial to the final reference frame will be:

$$\begin{pmatrix} x''' \\ y''' \end{pmatrix} = MRM \begin{pmatrix} x \\ y \end{pmatrix} \quad (3.28)$$

We can now consider a cavity formed by a set of four mirrors. After a round trip, the coordinate of a point (x_1, y_1) in the final reference frame will be:

$$\begin{pmatrix} x_1 \\ y_1 \end{pmatrix} = MR_{41}MR_{34}MR_{23}MR_{12} \begin{pmatrix} x_0 \\ y_0 \end{pmatrix} \quad (3.29)$$

where (x_0, y_0) are the coordinates of the point in the initial frame and R_{ij} indicates the rotation matrix transforming the reference frames between mirrors M_i and M_j . Noting that:

$$MRM = \begin{bmatrix} \cos\gamma & -\sin\gamma \\ \sin\gamma & \cos\gamma \end{bmatrix} = R^{-1} \quad (3.30)$$

the Eq. 3.29 becomes:

$$\begin{pmatrix} x_1 \\ y_1 \end{pmatrix} = R_{41}^{-1}R_{34}R_{23}^{-1}R_{12} \begin{pmatrix} x_0 \\ y_0 \end{pmatrix} \quad (3.31)$$

The odd-numbered mirrors are associated with a rotation R_{ij} , while the even-numbered mirrors are associated with an inverse rotation $R_{ij}^{-1}(\gamma) = R_{ij}(-\gamma)$. If we invert the direction of rotation between M_2 and M_3 , as well as between M_4 and M_1 , the total angle of image rotation after a round-trip is:

$$\Theta = -(\gamma_1 + \gamma_2 + \gamma_3 + \gamma_4) \quad (3.32)$$

where we denoted as γ_i the rotation angle after mirror M_i . In the RISTRA cavity, this angle Θ is 90° . This image rotation technique allows that on successive passes, each portion of the resonant beam samples a different gain region, averaging the gain and refractive index inhomogeneities. Moreover, it also averages over eventual pump inhomogeneities. The result is a much more symmetric beam with a better beam quality. Another characteristics of this cavity is that choosing the angle of incidence on the first mirror determines all the other mirror angles. This allows the cavity to be constructed from a monolithic metal block. Therefore, the cavity has a fixed optical axis, being insensitive to vibrations and small misalignments. In the RISTRA the angle of incidence on all mirrors is 32.765° [58]. It is equal for all cavity mirrors, allowing the use of identical mirrors. Together with the image, the polarization also experience a rotation. An intra-cavity half-wave plate is therefore needed to restore the original polarization state after one round-trip to allow for proper phase-matching on all passes. The RISTRA as an OPO resonator was proven effective and advantageous in many OPO studies with improved beam quality [60, 73, 74, 62]. However, previous studies dealt mostly with low repetition, high energy pump sources. A direct comparison of the RISTRA with the linear and planar ring cavity was also limited to low repetition rate regime (10 Hz) [73]. The authors focused on the non resonant idler beam, finding an improvement in the beam quality only in the case where large beams are used (pump diameter of 5.35 mm).

The second type of non-planar ring cavity considered in this thesis was developed at ISL and it is called Fractional Image Rotation Enhancement (FIRE) cavity [59, 75]. Its mirror configuration is depicted in Fig. 3.5 (b). It is composed by six mirrors. As the RISTRA, it exploits the image rotation to enhance the beam quality of the output beams. However, in this case the cavity is based on an image rotation angle that can't be expressed as $2\pi/n$, where n is an integer number. In this way the number of transversal modes that after one round-trip are self consistent is greatly reduced, resulting in fewer transverse modes oscillating within the resonant cavity. In particular, the FIRE uses a rotational angle $\Theta = 77.448^\circ$. The angle of incidence on the mirrors is the same as for the RISTRA ($\sim 32.7^\circ$), allowing to use the same mirrors. As for the RISTRA, in the FIRE the polarization rotation is compensated by an intra-cavity half-wave plate. Such cavity was proven effective to enhance the beam quality in high energy low repetition rate systems [61]. Using this type of cavity, a beam quality

factor down to an M^2 factor of 1.5 has been achieved for 36 mJ of output pulse energy at a repetition rate of 100 Hz [52]. However, it has never been studied in high average power setups.

All these studies proved the effectiveness of the RISTRA and FIRE resonators in the nanosecond regime with low repetition rate pump sources. But as low repetition rate means low average power, less thermal issues arise in the crystal. As mentioned previously, in this thesis we will focus on high average power OPO systems. If a high repetition rate pump source is used (>1 kHz), the thermal effects can not be ignored.

3.3. Laser sources and their characterization

3.3.1. Laser beam quality

In this section we will introduce the most important concepts when defining the beam quality of a laser. In particular, we will give the definition of beam width and M^2 beam propagation factor.

If we consider an ideal laser with a stable cavity, oscillating in a transverse TEM00 mode and emitting a beam with propagation direction z , its intensity distribution can be written:

$$I(r, z) = I_0 e^{\frac{-2r^2}{\omega^2(z)}} = \frac{2P_0}{\pi\omega^2(z)} e^{\frac{-2r^2}{\omega^2(z)}} \quad (3.33)$$

where r is the radial distance from the center of the beam, P_0 is the total power of the beam, and $\omega(z)$ is the radius at which the intensity values fall to $1/e^2$ of their axial values, i.e: $I(\omega) = I_0 e^{-2}$. The evolution of the beam radius $\omega(z)$ along z is given by the hyperbolic relation [76]:

$$\omega^2(z) = \omega_0^2 \left[1 + \left(\frac{\lambda z}{\pi\omega_0^2} \right)^2 \right] = \omega_0^2 \left(1 + \frac{z^2}{z_R^2} \right) \quad (3.34)$$

where ω_0 is the beam radius at waist position, λ is the wavelength and z_R is called Rayleigh range. It indicates the position at which $\omega(z_R) = \sqrt{2}\omega_0$. All these quantities are depicted in Fig. 3.7.

From the equation above, it is clear that a proper definition of beam width is crucial when it comes to characterize the divergence of a laser beam. Many different definitions of beam radius have been used over the years, not all of them related to each other. The most widespread are:

- Width at $1/e^2$ intensity points: it is equal to the distance between two points on the marginal distribution where the intensity is $1/e^2$ the maximum value. This corresponds to a diameter containing the 86.5 % of the

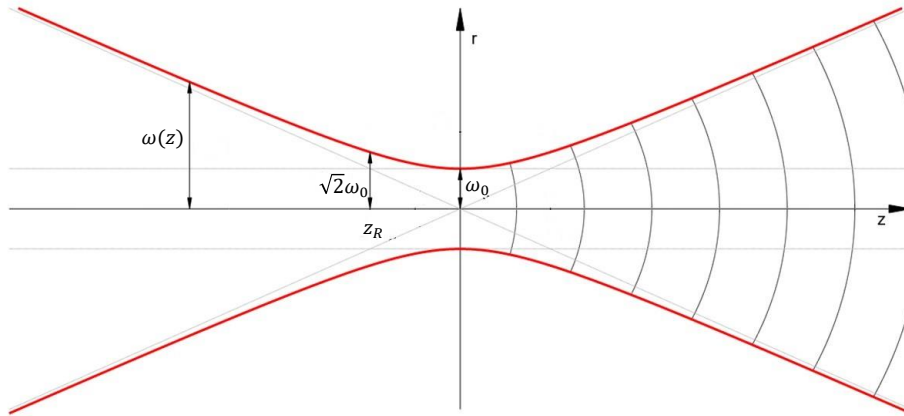


Figure 3.7: Gaussian beam width $\omega(z)$ as function of the propagation distance z . z_0 is the beam waist position and ω_0 the corresponding beam waist radius.

- beam power. Sometimes it can be used the width at $1/e$ intensity points;
- FWHM: distance between two points at which the intensity is half the maximum value;
- 10 % - 90 % knife-edge width: definition given by the commonly used knife-edge method measurement. The width of the beam is defined as the distance between the points of the measured curve that are 10 % and 90 % of the maximum value. It corresponds to 80 % of the total beam power for a gaussian beam;
- $D4\sigma$: the diameter is defined as 4 times the standard deviation σ of the intensity distribution.

Depending on the shape of the beam profile the above definitions can give very different width values, as illustrated in Fig. 3.8 using a Gaussian profile. Because of its rigorous mathematical definition, the $D4\sigma$ method is meaningful also in the case of multimodal beams, i.e. beams with more than one local maximum. Consequently, it became the ISO international standard definition for beam widths. If the beam has a gaussian shape, it gives the same results as the $1/e^2$ method, i.e. $D4\sigma = 2\omega$. For these reasons, in this thesis, we used the $D4\sigma$ approach.

Using such definition for the beam diameter, we can now consider more realistic laser beam, which are often elliptic and possibly astigmatic (in x and y directions). In this cases, the evolution of the beam radius in each transversal

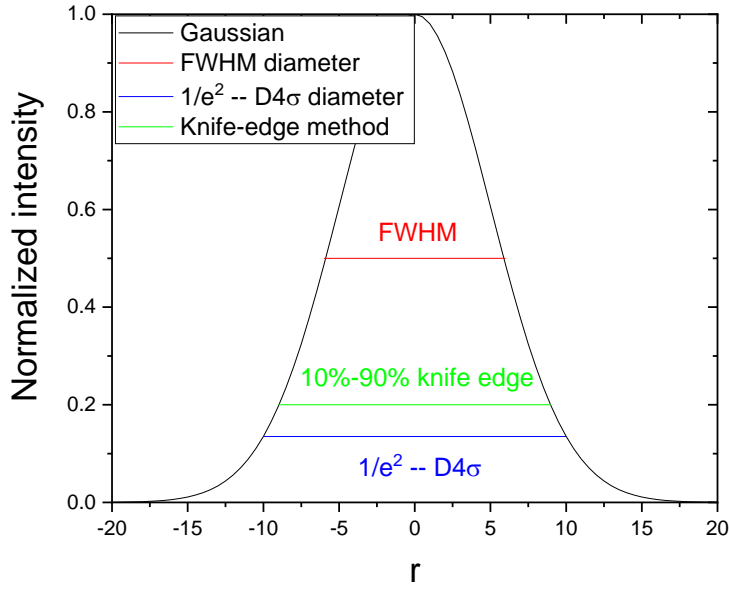


Figure 3.8: Gaussian intensity beam profile. Different definitions of beam widths are depicted.

direction i can be written [77]:

$$\omega_i^2(z) = \omega_{0i}^2 + \left(M_i^2\right)^2 \left(\frac{\lambda}{\pi\omega_{0i}}\right)^2 (z - z_{0i})^2 \quad (3.35)$$

where z_0 is the waist position. The factor M^2 is the so-called beam quality factor, which characterizes the evolution of the beam radius for an arbitrary beam. It gives a measure of how close the real laser beam is to the diffraction limit. It assumes values ≥ 1 for any arbitrary beam profile. The limit $M^2 = 1$ occurs only in the case of a perfectly single mode gaussian beam. Practically, in order to measure this factor, it is necessary to acquire spatial profiles (images) of the beam at generally five positions ranging from the beam waist to typically $2z_R$. The ellipticity of the beam profiles allows to define two axes that are common to all images and extract the beam diameters $2\omega_i$ along these axes. Finally, the $\omega_i(z)$ -data can be fitted using Eq. 3.35 to obtain the M^2 factor as one of the fit parameters.

This beam propagation factor is of crucial importance when we consider the fluence of a laser beam with pulse energy E_p :

$$\Phi = \frac{2E_p}{\pi\omega_{D4\sigma}^2} \quad (3.36)$$

where $\omega_{D4\sigma}$ is the beam radius measured by the $D4\sigma$ method. For some appli-

cations, such as IRCM, a certain fluence on a target is needed. As seen from Eq. 3.35, the beam radius at a certain distance depends on the M^2 factor. Thus, having an higher M^2 , i.e. higher divergence, means that in order to deliver the necessary fluence on target, high energy pulses are needed. This is not always effortless or possible. Consequently, it is beneficial to design sources with the best beam quality possible.

3.3.2. Thermal lens and gain guiding

As mentioned previously, this thesis focuses on high power ZGP based OPOs delivering good beam quality. The thermal effects arising in such devices at high powers are a significant challenge to overcome. There are mainly two type of effects that can affect the beam quality: thermal lensing and gain guiding. Their effect on the beam quality in our specific setup will be discussed in Chap. 6.

Although usually weak, the residual absorption of the ZGP crystal in the $2 \mu\text{m}$ spectral range results in a spatially varying refractive index. This creates a thermal lens inside the crystal, which is usually unwanted. Under continuously pulsed operating conditions, if the period between pulses is shorter than the thermal relaxation time, a steady-state temperature distribution is achieved. The consequent thermal lens has an effective focal length given by [71]:

$$f \approx \frac{kA}{P_a} \left(\frac{1}{2} \frac{dn}{dT} \right)^{-1} \quad (3.37)$$

where k is the thermal conductivity ($36 \text{ W m}^{-1}\text{K}^{-1}$ for ZGP [78]), A is the area of the pump beam, P_a is the pump power absorbed and dn/dT is the temperature variation of the refractive index. In the case of ZGP, the Sellmeier-relation gives $dn/dT \approx 1.5 \cdot 10^{-4} \text{ K}^{-1}$ at $4 \mu\text{m}$ [79, 52]. To have an idea of the strength of the thermal lens in a high average power ZGP OPOs, we can consider as first approximation a crystal with an absorption of the pump power of 8 %. With a beam diameter of 1 mm and a input pump power of 60 W, we obtain a focal length of $f \approx 79 \text{ mm}$. The resulting thermal lens is therefore significant and it reduces the beam quality of the output beams. In systems with well-characterized and known thermal lens, it is possible to compensate it with elements of fixed dioptric strength. One way to counter the thermal lens is direct compensation with intracavity negative lens [61] or a Galilean telescope [52]. This approach was also proven to be effective in the demonstration of an OPO-OPA 102 W system [55].

Usually, only the steady-state behavior of the thermal lens is considered, its dynamic nature is not studied carefully. If the heat deposited into the material is significant and the separation between the pulses is longer than the thermal-relaxation time, a time varying thermal lens arises. The material thermal time

constant is given by [79]:

$$\tau = \frac{r_0^2 c_p \rho}{k} \frac{1}{\beta_n^2} \quad (3.38)$$

where ρ is the material density (4.175 g cm^{-3}), c_p the specific heat ($0.464 \text{ J g}^{-1} \text{ K}^{-1}$ [78]), k the thermal conductivity, r_0 the pulse beam radius, and β_n are the roots of a Bessel eigenfunction equation reported in [80], which depends on the cooling and boundary conditions. For a beam diameter of 1 mm and a crystal of dimension of $6 \times 6 \text{ mm}^2$, an assumption of infinite boundary condition is reasonable [79]. We can then consider a value of 2.3 for the lowest-order solution of the Bessel equation, obtaining a thermal relaxation time of approximately 2.5 ms. High average power, high repetition rates OPOs usually operate at KHz frequencies. which corresponds to an interpulse time separation of less than a millisecond. Therefore, a steady-state thermal lens is obtained. The effect of the thermal lens will be studied in Chap. 6.

The second effect present in high power OPOs is the gain guiding effect. From Eqs. 3.14 and 3.15, we can see how the gain depends on the intensity of the pump, hence on pump pulse distribution $I_p(r)$. Different part of the beam experience different gain factors, which results in the so-called gain guiding effect [81]. We can estimate the strength of such effect in our usual experimental conditions, similarly as in [61]. Taking into account a Gaussian intensity profile with a pump spot diameter of 1 mm, pump power of 60 W, and $d_{eff} = 77 \text{ pm/V}$, the calculated parametric gain distribution from Eq. 3.15 is presented in Fig. 3.9.

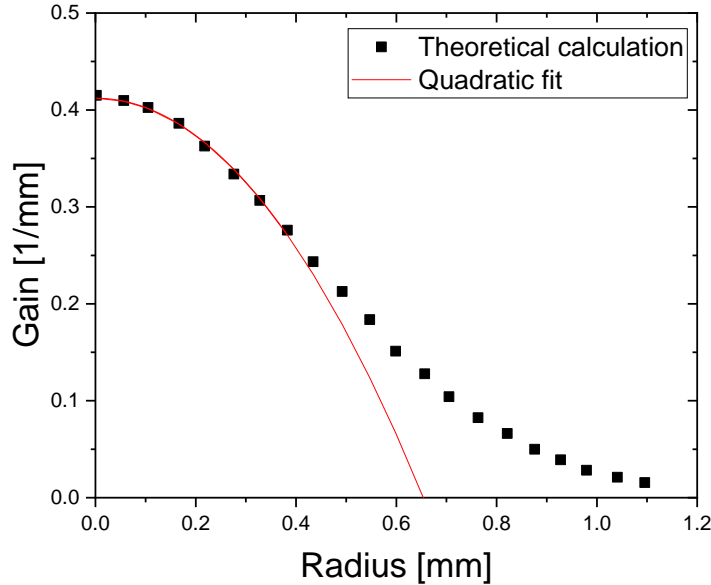


Figure 3.9: Variation of the theoretical parametric gain and its fitting according to a quadratic approximation.

Usually, as first approximation it is used a quadratic variation of the gain parameter describing the center of the beam [82]:

$$\alpha(r) = \alpha_0 - \frac{1}{2}\alpha_2 r^2 \quad (3.39)$$

Fitting the calculated values, we find an $\alpha_2 \approx 2 \text{ mm}^{-3}$. Although simple, these calculations show already how the gain can vary significantly within the pump beam. As a consequence, the resonant beams can be much narrower than the input pump beam. This may lead to a loss of the spatial overlap between the beams, which results in a lower conversion efficiency and beam quality [81].

4. Experimental setup and simulation tools

In this chapter, the setups used for the investigation of high power mid-IR OPOs are described. Firstly, the OPO pump source is presented. It consists of an Ho^{3+} :LLF based MOPA system which was developed at ISL. Its unique performances allow efficient pumping of a ZGP based OPO [83]. The corresponding experimental setup for injection and characterization of the OPO is presented. The procedures and instruments employed to measure the different quantities (average power, beam quality factor etc.) are described and explained. Various ZGP crystals with different characteristics, such as absorption coefficients and dimensions, were utilized during the thesis. Thus, a complete overview of them is given. During the investigation, different resonator cavities were studied, ranging from linear to different types of non-planar ring cavities. Therefore in this chapter, details are given concerning their geometry and design, such as resonance operation conditions, cavity length, optical round-trip etc. Finally, a particular focus is given to the simulation softwares used during these studies. Two main programs were used in order to simulate OPO behavior under different conditions. The first is the freely available SNLO software, used mostly to simulate the linear resonators [67]. The second simulation software (OPODESIGN) is a FORTRAN-based code developed in partnership with ISL in the past years that can simulate the performances of the non-planar ring cavities. Their working principle, as well as their strengths and limitations, will be explained in detail in the last section of this chapter.

4.1. Experimental setup

4.1.1. Pump source

An Ho^{3+} :LLF based MOPA system was used as a pump source for OPO injection. Its design is shown in Fig. 4.1 and it is described in detail in [83].

The 1940 nm, unpolarized pump light of a continuous wave 120 W Tm fiber laser (IPG TLR-120-WC-Y14) is sent through a first telescope (L1: $f = 7$ mm; L2: $f = -40$ mm) and it is split into two orthogonally polarized pump beams through the use of a thin film polarizer (TFP). Each of the beam passes a second telescope (L3: $f = -75$ mm; L4: $f = 100$ mm; L5: $f = -200$ mm). The size of the

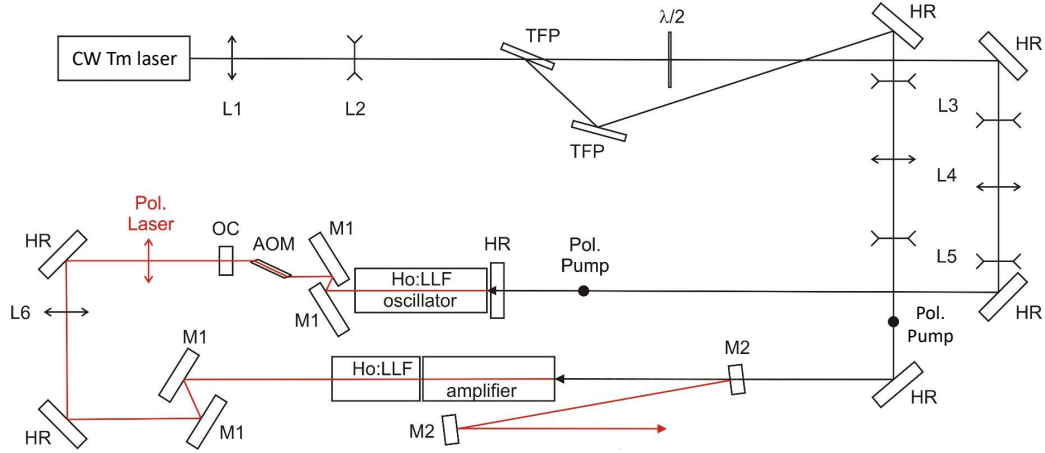


Figure 4.1: Experimental setup of the end-pumped Ho^{3+} :LLF MOPA system. TFP: thin film polarizer, $\lambda/2$: half-wave plate, HR: high reflector. Image taken from [83].

pump beam in the crystals could be adjusted by moving lenses L3 and L4 of the second telescope. All crystals are 0.5 at. % Ho doped a-cut LLF crystals with a diameter of 6 mm. The c-axis of the 60 mm long oscillator crystal and the two amplifier crystals (40 and 60 mm long) is oriented parallel to the vertical polarization of the pump beams to take advantage from the high absorption on π -polarization (vertical) of Ho^{3+} :LLF at 1940 nm. The folded resonator is approximately 130 mm long using a concave output-coupler (OC) with a radius of curvature of 300 mm and a reflectivity of 60 %, a flat high-reflector (HR) and two flat mirrors M1, tilted by 32° , all three having high transmission at pump and high reflection at lasing wavelength.

A 17 mm Brewster-cut acousto-optic modulator (AOM) (Gooch & Housego model QS041-4M(BR)-IS3) is used for Q-switched operation with a repetition rate of 10 kHz. The radio-frequency power is 20 W at 41 MHz. The AOM forces oscillation on σ -polarization of the oscillator crystal (horizontal) and amplification is done on σ -polarization, too. The middle of the oscillator crystal is imaged 1 to 1 to the center of the composite amplifier crystal with lens L6 ($f = 150$ mm). The Ho^{3+} :LLF crystals are glued in copper mounts which are water cooled during operation.

The total average output power of the system is presented in Fig. 4.2. The Ho^{3+} :LLF delivers 33 W of average power at a repetition rate of 10 kHz from the oscillator stage. After the amplification stage, the total output power delivered is 68.7 W. The optical-to-optical efficiency, calculated as the ratio between the input pump power and the total output power, is 61.5 %. The second telescope was adjusted to obtain temporally stable pulses. The pulse profile at maximum

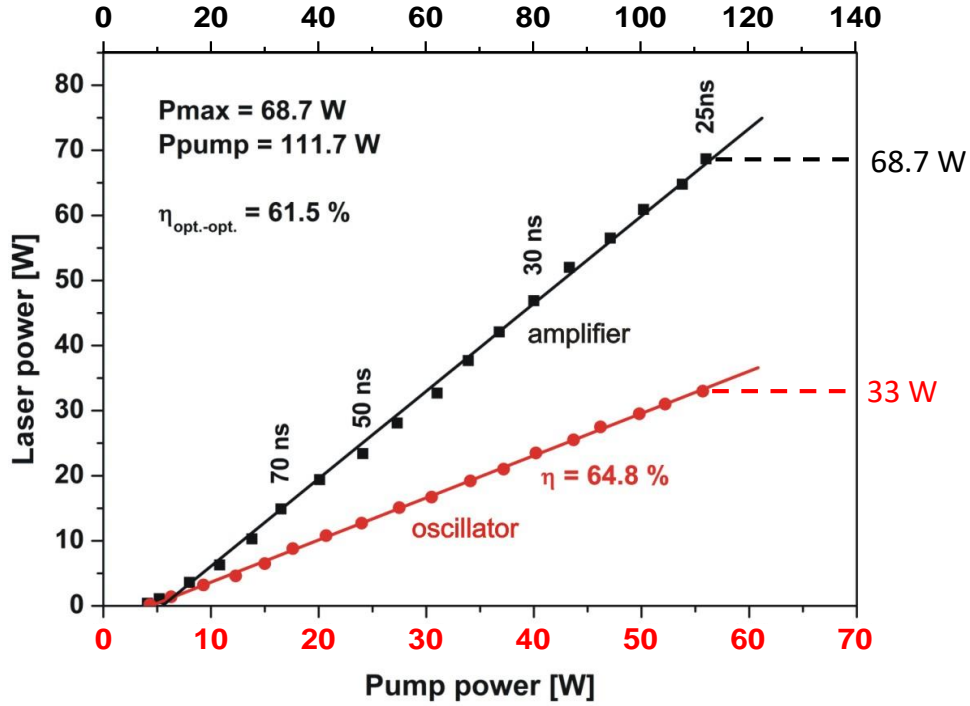


Figure 4.2: Laser power of the Ho^{3+} :LLF MOPA system. Image adapted from [83]. The bottom axis refers only to the pump power at the oscillator stage. The top axis refers to the pump power at the oscillator + amplifier stage.

power is presented in Fig. 4.3 (a). The pulse was acquired by a HgCdTe infrared detector, with a time constant ≤ 1.5 ns. The fitting of the pump pulse was done according to the Gaussian function, obtaining a Full Width Half Maximum (FWHM) of $\tau \approx 25$ ns. This corresponds to a maximum peak power of 274.8 kW. Under this operational conditions, the pump presents a good power stability, as presented in Fig. 4.3 (b). Over a period of operation of 30 minutes, the fluctuations have a standard deviation $\sigma = 0.19$ W. For an average value $\mu = 67.7$ W, this corresponds to a relative standard deviation $C_v = \sigma/\mu = 0.28$ %.

Concerning the output wavelength, the Ho^{3+} :LLF emission is centered at 2065 nm and has a spectral width of 0.55 nm during Q-switched operation, as presented in Fig. 4.4. The procedure of measurement is described in Sec. 4.1.2. Since the Ho^{3+} :LLF is operating in TEM₀₀ mode, the beam quality factor M^2 is close to diffraction limit. The corresponding measurement at maximum pulse energy of 6.87 mJ, whose procedure is described in Sec. 4.1.2, is presented in Fig. 4.5. More precisely, the M^2 factors assume a value in the X and Y directions of : $M_x^2 = 1$ and $M_y^2 = 1.02$. Some astigmatism can be noted between the two orthogonal directions.

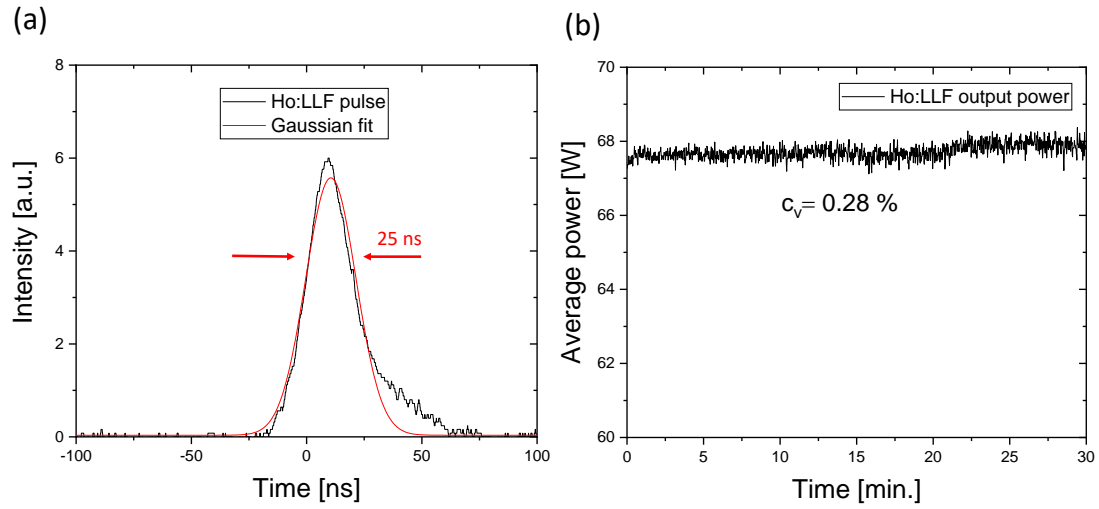


Figure 4.3: (a) Temporal profile of the pump pulse. The fit was done according to the Gaussian statistics. (b) Power stability of the Ho^{3+} :LLF output.

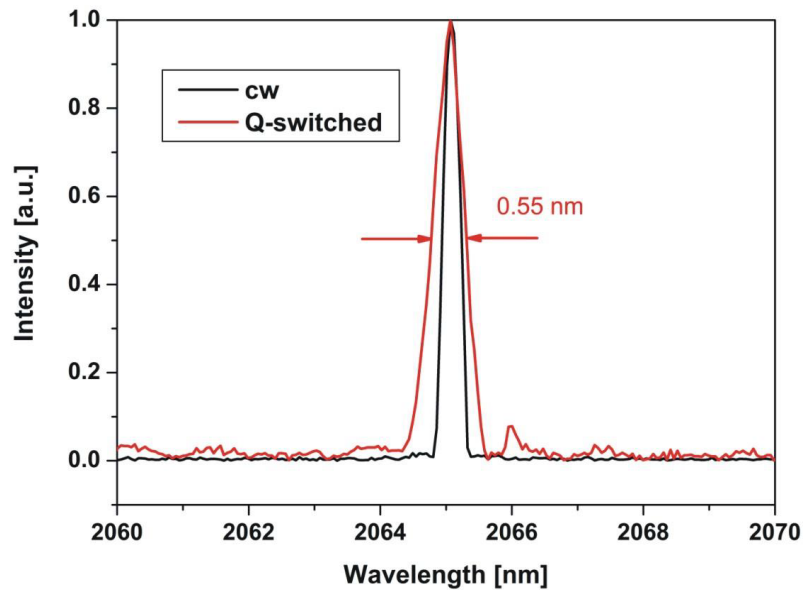


Figure 4.4: Spectral output of the Ho^{3+} :LLF pump source in continuous and pulsed mode. Image taken from [83].

4.1.2. Description of the setup

The experimental setup of the ZGP OPO is presented in Fig. 4.6. The energy peak fluence for a Gaussian beam is defined as $2E_{pulse}/(\pi\omega^2)$, with ω being the beam radius (see Eq. 3.36). Since we had no specific information about the

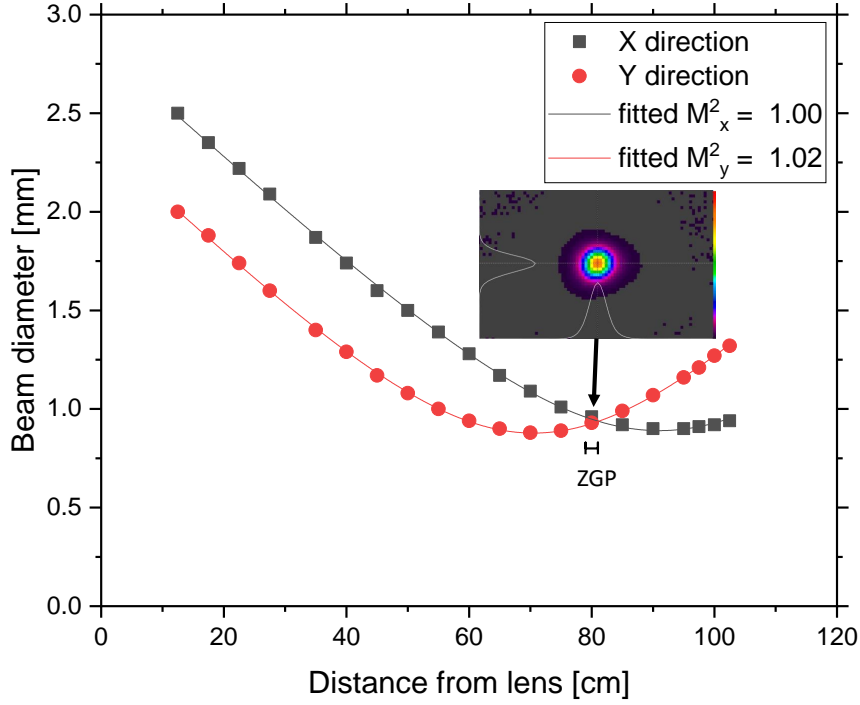


Figure 4.5: M^2 value measurement of the pump source at maximum output power. The position of a ZGP, with typical length of 20 mm, is depicted, together with the corresponding pump beam image.

laser damage threshold of the mirror and crystal coatings, the energy peak fluence was kept to a reasonable value for our experience [84, 85] ($< 2 \text{ J/cm}^2$) in order to avoid any risk of damage. Therefore, a 300 mm plano-convex fused silica (SiO_2) lens focuses the output from the Ho^{3+} :LLF onto the ZGP crystal with a measured beam diameter (according to the $D4\sigma$ formalism) of 1 mm, corresponding to the data point at 80 cm from the lens in Fig. 4.5. This beam dimension corresponds to a fluence at maximum pump power of 1.75 J/cm^2 . A half-wave plate in combination with a polarizer allows polarization rotation and, by this means, pulse energy and power adjustment without changes in spatial and temporal pulse properties. At the working wavelength, the polarizer has transmittances of $T_p > 97\%$ and $T_s < 0.05\%$, corresponding to an extinction ratio $> 1940:1$. A Pockels cell allows voltage-controlled polarization rotation for power adjustment and pulse picking. It was used in order to modify the pump repetition rate externally. The triggering signal is generated by a 2-channel waveform generator (KeySight 33500B). We can set the pump repetition rate to the values: 0.1 kHz, 0.5 kHz, 1 kHz, 2.5 kHz, 5 kHz, and 10 kHz without affecting pulse properties. The temporal profiles of the pump and output beams are acquired by HgCdTe ambient temperature infrared detectors, with a

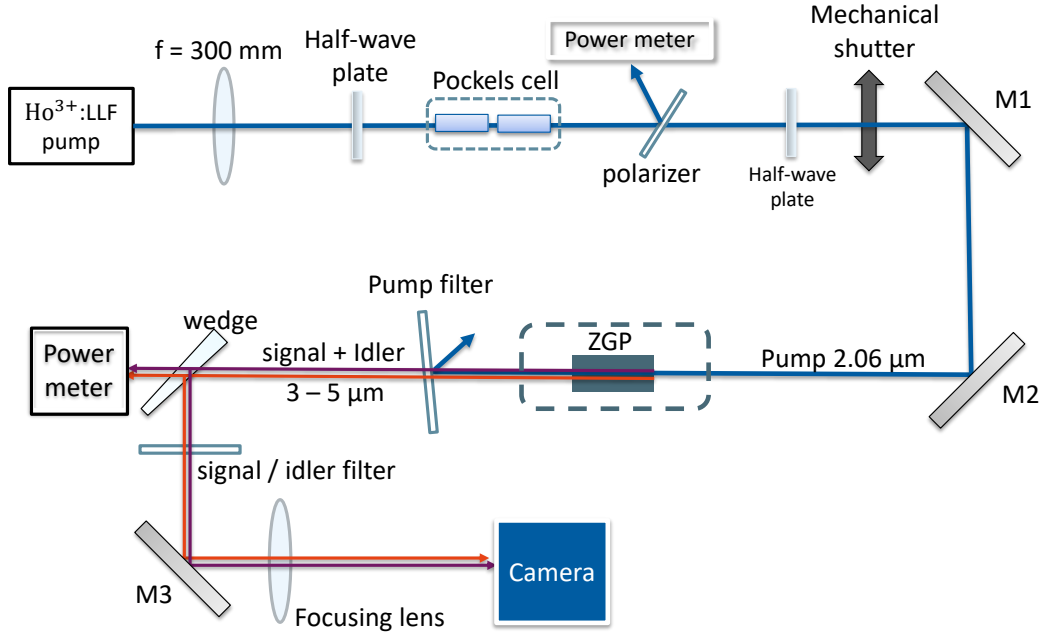


Figure 4.6: The scheme of the experimental setup for OPO pumping and characterization.

time constant $\tau \leq 1.5$ ns. Their response is then collected and monitored by a 4-channel, digital oscilloscope (Tektronix TDS 2024B). It has a 200 MHz bandwidth and 2 GS/s maximum sample rate, so that the time profiles are known with a resolution of 5 ns. A second wave plate allows to have the appropriate linear polarization for OPO pumping. For type I phase-matching the pump polarization is perpendicular to the crystal optical axis (ordinary polarization, see Chap. 3). The mechanical, remotely controlled beam shutter allows the pump beam blocking before the OPO cavity. M1 and M2 are bending mirrors which are high reflective at 45° for $2.06 \mu\text{m}$ wavelength ($R > 99\%$). They are used to align the pump beam with the OPO resonator. All optical components used for delivering the pump beam insert up to 5% losses for the pump power before it reaches the ZGP OPO. Therefore, we had a maximum of approximately 65 W of pump average power available for OPO pumping.

Behind the OPO cavity, the residual pump is reflected by a dichroic silicon mirror, with $R > 99.9\%$ for $2.06 \mu\text{m}$ and $R < 5\%$ in the $3-5 \mu\text{m}$ region. Then, a CaF_2 wedge window with 4° tilting angle is used to pick off part of the two OPO beams for beam quality analysis. The reflection of the wedge strongly depends on the polarization of the incident beam [86]. Because of this, its contribution to the losses of the setup varies depending on the OPO resonator used and they were evaluated time by time. The bending mirror M3 is a silver protected mir-

ror, with high reflectance at the output wavelengths ($R > 96\%$ for $3\text{--}5\ \mu\text{m}$). For the beam quality measurements, the beams are first filtered by the appropriate filter for signal or idler wavelength and then focused by a CaF_2 focusing lens, AR coated in the $3\text{--}5\ \mu\text{m}$ range. Brightness determination was done by inspection of the signal and idler beams with an infrared pyroelectric array sensor (mks Ophir Pyrocam IV Beam Profiling Camera) using the test method for laser beam parameters: beam widths, divergence angle, and beam propagation factor M^2 (EN ISO 11146). The beam diameters were measured according to the $D4\sigma$ formalism. The beam radius as a function of the distance from the focusing lens were fitted according to the Eq. 3.35. The camera resolution is 320×320 pixels with pixel pitch of $80\ \mu\text{m}$. This camera was used in chopped (50 Hz) or triggered (100 Hz) modes for all the beam images. The 50 Hz frame rate offers 20 ms time resolution for the acquisition of beam images. The average power of the OPO, as well as the pump power, are monitored by two thermal power meters (mks Ophir L250W), which are water cooled during operation and have a power accuracy of $\pm 3\%$. The wavelengths involved are measured through the use of a iHR 320 spectrometer (Horiba): the beams are focused and injected into the spectrometer through a mid-IR hollow fiber. An home-made LabView program is then used to collect the spectra for further analysis.

4.1.3. ZGP crystals

As mentioned in Sec. 2.2, in this thesis the OPO was operated by using non-linear crystals of Zinc Germanium Phosphide (ZGP). The data concerning this type of crystal is presented in Appendix A. In particular, in this thesis crystals with different characteristics were used. They were purchased from two suppliers: the Harbin Huigong Science & Technology Co., Ltd., and the BAE systems. A photo of ZGP samples from each manufacturer is shown in Fig. 4.7, together with an uncoated ZGP.

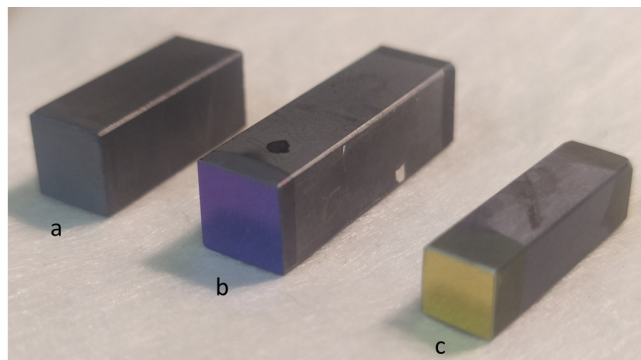


Figure 4.7: Picture of ZGP crystals: (a) Uncoated ZGP, (b) purchased from Harbin Institute, (c) purchased from BAE Systems.

All the crystals used are cut with respect to the optical axis in order to allow type I phase-matching at $2\ \mu\text{m}$ ($o \rightarrow e + e$, Chap. 3). Their end faces are AR coated for the pump wavelength and in the $3\text{--}5\ \mu\text{m}$ spectral range. Transmission through the AR-coated crystal was evaluated with a spectrometer (PerkinElmer Frontier FT-IR/FIR Spectrometer). In Fig. 4.8 such transmission measurement is presented for two crystals, coated by the two suppliers.

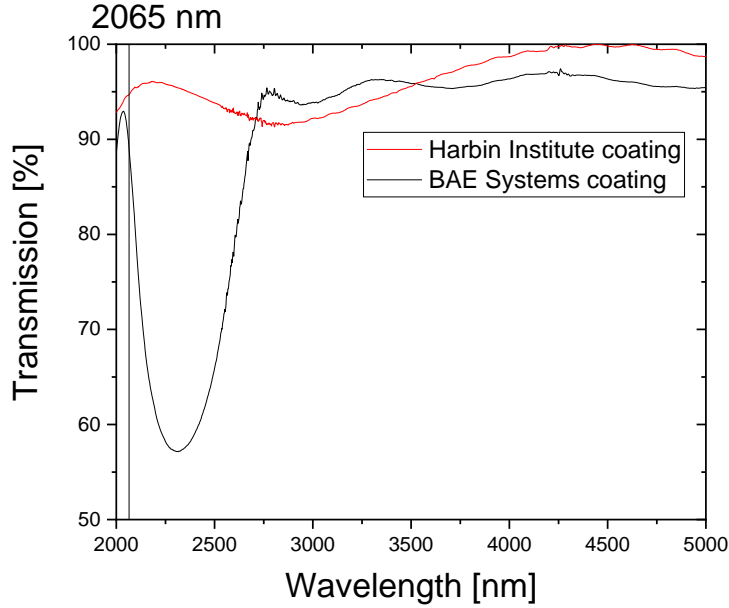


Figure 4.8: Transmission through a ZGP with AR coating from the two different suppliers. The vertical line highlights the pump wavelength at 2065 nm.

Since the measurement was carried out with unpolarized light, its accuracy is low. Some conclusion can however still be made. Although differences can be noted in the $2.1\text{--}2.7\ \mu\text{m}$ spectral range, in the $3\text{--}5\ \mu\text{m}$ region the two coatings are both high transmittive. Transmission at pump wavelength is comparable. A total of four ZGP crystals were used in this thesis: two from the Harbin Institute and two from the BAE systems. The first ones have a size of $6 \times 6\ \text{mm}^2$ (aperture) \times 20 mm (length) and are cut at 55° with respect to the optical axis. They were used for the investigation of the linear, RISTRA and FIRE OPO resonators, as it will be discussed in Chap. 5. Crystals provided by BAE Systems have instead smaller size: $4 \times 4 \times 16\ \text{mm}^3$. The smaller dimension was chosen in order to implement such ZGPs in the novel mini-FIRE resonator, which will be presented in Chap. 6. Moreover they are cut at 56° .

For all the crystals, the absorption at $2.065\ \mu\text{m}$ was determined from the ratio between the power transmitted through them and the incident one. To calculate the absorption coefficient, we considered negligible absorption of the coating

layers and we took into account their reflectivity, which were measured $< 1\%$ for our linearly polarized pump source. All the crystals have a low absorption at pump wavelength and are among the best available in the market. In Tab. 4.1 a summary of the characteristics of all the used ZGPs is presented.

ZGP name	Supplier	Cut angle [°]	Dimensions [mm ³]	Absorption [%]	Abs. coeff. α [cm ⁻¹]
CH#1	Harbin	55	6x6x20	6.4	0.033
CH#2	Harbin	55	6x6x20	8.4	0.044
BAE E1	BAE Systems	56	4x4x16	7.5	0.049
BAE E2	BAE Systems	56	4x4x16	8.4	0.055

Table 4.1.: Characteristics of the ZGP used in the thesis. Absorption coefficients are measured at 2.065 nm.

To operate the OPO and avoid excessive thermal load on the crystals, the ZGPs were wrapped in indium foil and mounted inside the optical cavities in copper holders, serving as heat sinks. Some of these holders could also be water cooled (see Sec. 4.1.4). The copper holders were then mounted on a rotational stage to allow angle tuning and thus critical phase-matching.

4.1.4. OPO cavities

For the investigation of high power ZGP OPOs carried out in this thesis, three different type of OPO geometries have been studied: a linear cavity resonator and two types of non-planar ring cavities (called RISTRA and FIRE). Their mirror configurations are shown in Fig. 4.9.

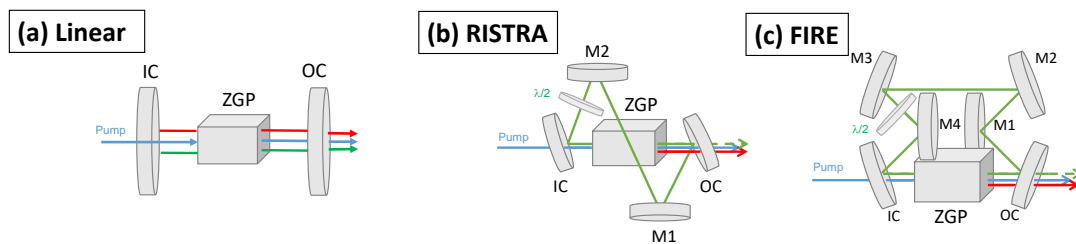


Figure 4.9: The three different cavities that were studied during the thesis. (a) Linear resonator. (b) RISTRA resonator. (c) FIRE resonator.

The linear cavity is composed of two flat mirrors. A picture of it is shown in Fig. 4.10 (a). The ZGP is water cooled during OPO operation. The input coupler (IC) is highly transmissive for the pump wavelength ($T > 95\%$) and highly reflective in the 3-5 μm range. The output coupler mirror (OC) is also highly

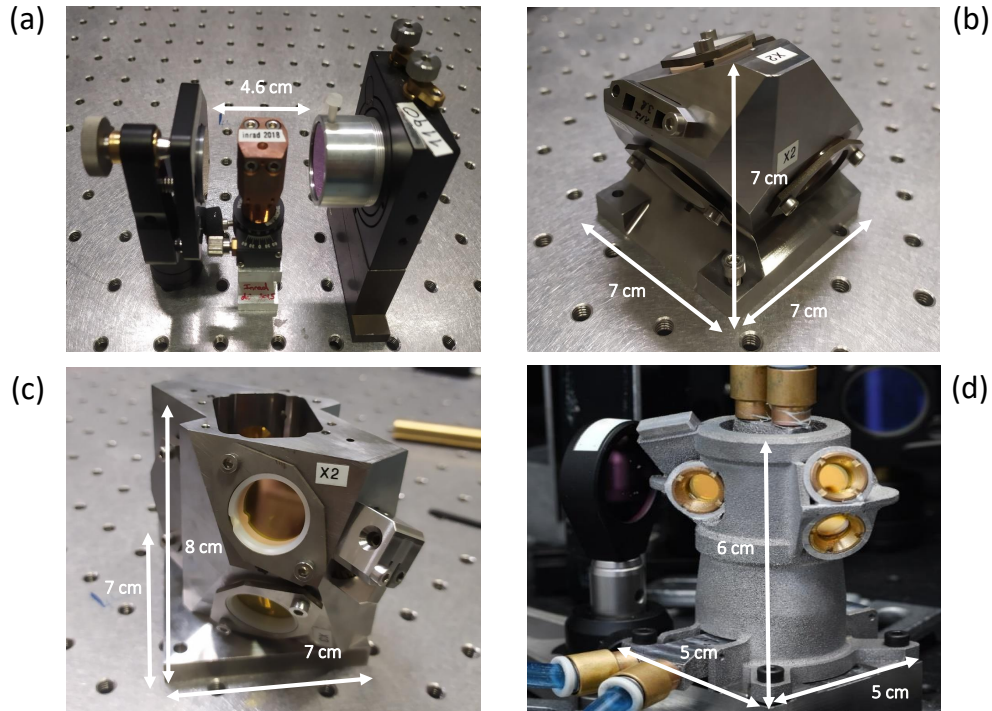


Figure 4.10: Pictures of the cavities used in the thesis. (a) Linear resonator. (b) RISTRA resonator. (c) FIRE resonator. (d) Mini-FIRE resonator.

transmissive for the pump and has $\approx 50\%$ reflectivity for both signal and idler wavelengths. Therefore the used linear resonator is a single pump pass cavity and it is operating in doubly resonant regime. Various lengths were tested, as it will be seen in Sec. 5.1.2. However, for the most part of the thesis, the cavity was set to a physical length of 46 mm. Considering the refractive index of ZGP for the signal and idler wavelengths ($n \approx 3.16$), the optical round-trip was calculated to be ≈ 178 mm when the 20 mm ZGP was used. This guarantees a short build-up time (thus good efficiency) and similar optical length with respect to the RISTRA. The main drawback of such resonator geometry concerning practical operation lies in the power stability. Indeed, the back-reflection of the pump beam from the flat mirrors, even though less than 5%, was sufficient to prevent us to obtain stable operation at high powers (above ≈ 20 W of pump power). Therefore, in order to reach high output powers, the cavity was operated with a slight misalignment. Such operation however hampered the beam quality of the output beams, as it will be presented in the next chapter.

While the linear resonator has a length easy to change, the non-planar ones are monolithic structures, with an optical length defined by the mechanical design. However, they don't require any mirror adjustment. The first non-planar cavity used in this study is the Rotated Image Singly-resonant Twisted RectAn-

gle (RISTRA) [72] ring resonator (Fig. 4.10 (b)), based on 90° image rotation and composed of four flat mirrors in a non-planar configuration [58]. As the linear cavity, it is single pump pass. Contrarily to the latter, it is operated in singly signal resonant regime. The output coupler (OC) of the RISTRA is partially reflective for the signal beam ($R \approx 50\%$) and highly transmitting ($T > 95\%$) for the pump and the idler. The input coupling mirror (IC) is tilted by 32.7° and it is identical to the two other mirrors (M1, M2). They have high transmission for the pump ($T = 86.3\%$) and the idler ($T > 94\%$), and high reflectivity for the signal ($R > 99\%$). The uncoated, zero-order MgF_2 half-wave plate compensates for polarization rotations in the resonator and restore the initial polarization after one round trip of the signal wave. The physical length of the resonator is 130 mm, which corresponds to an optical round trip of around 173 mm for a ZGP with a length of 20 mm. Therefore its cavity length and build-up time is comparable to the linear resonator.

The second non-planar cavity studied is the Fractional Image Rotation Enhancement cavity (FIRE) [75], composed of 6 flat mirrors [59]. Two versions of such resonator were implemented. The first one, shown in Fig. 4.10 (c), have a physical cavity lengths of 222 mm, corresponding to an optical round trip of 265 mm. Likewise the RISTRA, the IC mirror ($T = 84\%$) allows the pump beam to enter and pass through the ZGP crystal while reflecting the signal beam. The OC has again a reflectivity of $\approx 50\%$ for the signal beam and it's high transmittive for pump and idler. The other 4 mirrors that make the round trip in the resonator are all identical to the IC, and a half-wave plate compensates the polarization rotation. Since the cavity length of this resonator is longer than the previously mention cavities, its build-up time, thus its threshold, is higher. Therefore, a new miniaturized design of the FIRE (named mini-FIRE) was conceived and built. Its picture is shown in Fig. 4.10 (d). It was thought to combine the non-planar geometry of the FIRE with a small cavity length and it will be presented in Sec. 6.1.3. Its design implements a water cooling system for the ZGP crystal. The half-inch cavity mirrors used in this case have a high reflectivity ($R > 99\%$) for the signal beam and high transmission ($R < 5\%$) for the pump and idler wavelengths. The OC is partially reflective ($R \approx 50\%$) for signal and transparent for pump and idler. In order to have a smaller cavity dimensions, the ZGP used in this resonator has a length of 16 mm. The resulting optical round trip is in this case 135 mm (101 mm of physical length). In Tab. 4.2 the resonators studied are summarized.

OPO resonator type	Operational regime	ZGP length [mm]	Physical cavity length [mm]	Optical round trip length [mm]
Linear	doubly resonant	20	46	178
RISTRA	singly resonant	20	130	173
FIRE	singly resonant	20	222	265
Mini-FIRE	singly resonant	16	101	135

Table 4.2.: Resume of the resonators studied in this thesis.

4.2. Simulation softwares

Despite the large number of theoretical and experimental studies, numerical simulations are essential when it comes to design and improvement of nanosecond OPOs, since simple analytic expressions for threshold and conversion efficiency are crude approximations. In this thesis, two main simulation tools were used to simulate the beam propagation in the non linear crystal and the OPO behavior. The first one was the SNLO software and it was used to simulate and validate the experimental results when working with linear resonators. Although in principle it could be used also to simulate non-planar cavities, its functioning was not straightforward. Therefore, to simulate the RISTRA and FIRE cavities, the OPODESIGN code was utilized.

In this section, both software are presented and explained.

4.2.1. SNLO

The first software used to simulate the behavior of OPOs is the freely available SNLO code, developed by *A. Smith* [67]. It solves the nonlinear partial equations (see Chap. 3) through the split-step integration method in order to numerically simulate various applications, accounting for diffraction and walk-off effects. In the program there are two types of functions coded. The first type helps in computing crystal properties and they were used to evaluate quantities such as phase-matching angles, refractive indices, walk-off angles etc. These information were then used as inputs for the second class of functions, that models the performances of nonlinear crystals for various applications. The software can be used to characterize linear and planar ring resonators for an extensive set of applications such as OPO, OPA, injection seeded OPO etc. Moreover, SNLO could also simulate the RISTRA cavity. However, this function is not publicly available and so it was not utilized in this thesis.

In the context of this work, as we will see in Chap. 5, we used this program in order to simulate the behavior of a linear OPO resonator under different operation conditions. Validating the simulation results with experimental data, we aimed to implement the most performing cavity for our pumping conditions in terms of output power and M^2 value. In order to model the OPO behavior, we

used the function named 2D-cav-LP. In Fig. 4.11 a common table of inputs is shown.

	Red1	Red2	Blue
Wavelengths (nm)	3800	4522	2085
Indexes of refraction	3.148	3.143	3.146
Crystal left reflectivity	0	0	0
Crystal right reflectivity	0	0	0
Crystal loss (per mm)	0	0	0.0033
Enrgy/Pwr left (J/W)	1.00E-9	0.00E0	1.0E-3
Enrgy/Pwr right (J/W)	0.00E0	0.00E0	
Pulse duration (ns)	0	0	25
Pulse delay (ns)	0	0	
Beam diameter (FWHM mm)	0.59	0.59	0.59
Supergaussian coefficient	1	1	1
Walk off angle (mrad)	11.3	11.31	0
Beam offset (mm)		0	0
Beam radius of curv. (mm)	1.00E10	1.00E10	1.00E10
Left mirror reflectivity	0.99	0.99	0.05
Right mirror reflectivity	0.5	0.5	0
Phase L-C (radians)	0	0	0
Phase C-R (radians)	0	0	0
Phase R-L (radians)	0	0	0
Mirror roc L R (mm)	1.00E10	1.00E10	
Dist. L-C C-R R-L (mm)	13	13	0
Grid numbers z x y	30	64	64
Crystal/grid sizes (mm)	20	0	0
Cavity type/inversion	1	0	
Deff (pmV)/delta k (1/mm)	77	0	

Size of grid in walk-off direction in mm.
Set to zero for auto scaling.

Figure 4.11: Input table of the SNLO function named 2D-cav-LP, that models the linear OPO resonator.

The model simulates the parametric generation from noise by using a low power signal seed beam. The power level of such seed was set to 10^{-9} W, corresponding approximately to one photon per mode [67, 87]. Inputs as refractive indices and walk-off angles are straightforwardly evaluated through the Q_{mix} function. A common mistake is on the definition of the beam diameter as input. The values reported in this thesis are obtained according to the $D4\sigma$ formalism, which in the case of Gaussian beams is equivalent to the $1/e^2$ method. The SNLO calculations however require the FWHM diameter as input. Therefore one has to

convert according to the relation $D_{FWHM} = \sqrt{2 \ln 2} \omega_{1/e^2}$. Hence in our case we have $D_{FWHM} = 0.59 \text{ mm}$. For the highest pulse energies (above 3 mJ), the results can vary widely depending on the number of grid lines used and their size, so attention must be paid in order to choose them. For our simulations, usually a 64×64 or 128×128 grid number is used, while their size are auto-scaled (as shown in Fig. 4.11). Increasing the grid lines would be unpractical, since the computation time would increase up to several hours, without changing the results significantly.

The main limitation of this simulation software is that it does not account for any thermal effects inside the crystal. This can hamper the quantitative agreement with the experimental data, especially concerning the beam propagation factors and conversion efficiencies at highest pump powers. Moreover, the OPO oscillation thresholds could be underestimated because of this [78].

Agreement at the highest powers ($> 30 \text{ W}$) is also hampered if we consider the finite width of the spectra involved. Technically, it is possible to simulate broad band spectra with SNLO. However, this computation usually requires a lot of time and a big amount of memory dedicated, as specified also in the manual [67]. Indeed, with the default amount of memory dedicated (256 Mb), SNLO does not compute our experimental conditions. Increasing it up to 10 Gb would solve the memory problems. However, the highest pulse energies (above 2 mJ) are still not solvable. Therefore, in our simulations we considered monochromatic spectra, as done in other past studies [88, 89]. This decision however makes it tough to properly simulate high pulse energies ($> 3 \text{ mJ}$). Above that value SNLO predicts an exaggerated back-conversion effect, never experienced experimentally. The conversion efficiencies for the lower pulse energies are however trustful and in agreement with the experiments. In Fig. 4.12 it is presented a comparison of the output power simulated by SNLO and the corresponding experimental measurement. The specific data refers to a linear resonator of 46 mm length, a flat OC, and with a ZGP length of 20 mm. Such measurement will be discussed in detail in Chap. 5. The graph presents the results up to 20 W of input pump power. We can note that in this power regime, even though the simulated oscillation threshold is lower than the experimental, the two slope efficiencies are comparable. However, since the simulated curve has a slightly lower slope, it can be anticipated that the agreement between the two curves will get worse at higher pump powers.

4.2.2. OPODESIGN

The second software used in this thesis is called OPODESIGN. It was developed by G. Spindler [61] in partnership with ISL and it is written in the FORTRAN programming language. Regarding its working principle, the code solves the paraxial wave equation (Sec. 3.1.2) with the fast Fourier transform (FFT) method, propagating the signal, idler and pump beams in a non-planar

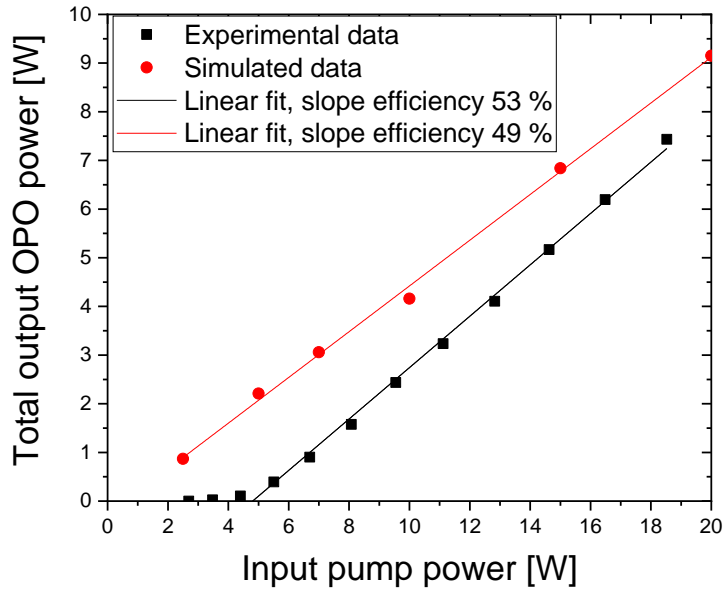


Figure 4.12: Simulated and experimental total OPO output power as function of the input pump power for a 46 mm, linear resonator with flat OC. The ZGP is 20 mm long.

ring cavity with image rotation. The program assumes a perfect signal polarization rotation compensation by the internal half-wave plate both for RISTRA and FIRE. The spatial walk-off effect is taken into account [90]. The temporal evolution of the pump pulse is realized by sampling slices of round-trip time duration. This code was used successfully to simulate high energy OPOs in the past [61, 52] and it is of particular utility to model the performances of the non-planar ring cavities RISTRA and FIRE. In this thesis it was used in order to evaluate the performances when designing the mini-FIRE cavity, as we will see in detail in Chap. 6.

An additional feature that the OPODESIGN accounts for, contrarily to SNLO, is the thermal effects. A thermal lens can be added in the calculations, depending on the conditions considered. The thermal lens is accounted for by inserting a lensing effect with a constant focal length into the beam propagation computations. Hence, it is not determined by any calculation of the temperature and refractive index distributions inside the crystal. In order to account for the variation of thermal effects as the power increases, we considered an effective focal length given by Eq. 3.37. The asymmetry and aberrations of a real thermal lens are neglected.

The main limitation of OPODESIGN lies when considering the finite widths of the OPO spectra, since it is based on single-frequency method. As a consequence, the code exaggerates the back conversion in the crystal. Thus, the

slope efficiency can only be roughly estimated. This behavior of the code is moreover promoted by the small diameter of the pump beam used during the experiments. Therefore, although threshold and slope efficiency can be roughly estimated, the code has limitations when it comes to model the beam propagation factors of the output beams, especially when considering the higher pump power levels.

5. High power ZGP OPO comparison in different cavities

This chapter is dedicated to the first part of experimental results, in which we study high power ZGP OPO cavities.

The first part of the chapter is focused on a linear resonator. Aiming at the most performing cavity, in terms of power and output beam quality, we investigated different cavity designs. We therefore implemented several linear resonators, varying their length, output wavelengths and curvature of the mirror output coupler (OC). As a result, a flat doubly-resonant linear cavity with a physical length of 46 mm was implemented. Then, various ZGP were tested under the same conditions, highlighting the influence of crystal quality on the OPO performances. The results obtained with the best performing crystal are finally presented and discussed in detail.

The second part of the chapter is dedicated to the study of the non-planar ring resonators. To improve the beam quality of the output beams for high power OPOs, we examined two non-planar cavities: RISTRA [72] and FIRE [75]. Although they demonstrated good results in high energy operation, they were never tested in high repetition rate, high average power systems. Their performances are therefore fully characterized.

Finally, in the last section, a complete comparison of the performances of the three cavities is done, highlighting the main advantages and drawbacks of each resonator.

5.1. Influence of linear cavity design on its performances

5.1.1. Motivation

In order to achieve high efficiency and high power ZGP OPOs, we implemented, as first step, a linear cavity resonator. Despite being the simplest OPO design, its performances can vary widely depending on the features implemented in its design. The pump beam size is constrained to not exceed the laser damage threshold of the optics and coatings involved. However, to obtain the highest performances, the pump beam should ideally be able to excite only the

transverse fundamental mode of the resonator [71, 91]. The size of such fundamental mode is determined by the geometry of the resonant cavity. Therefore, the pump beam diameter and its divergence within the cavity strongly affect the resonator design. Hence, we have to evaluate the most suitable configuration considering our pumping conditions ($D = 1 \text{ mm}$). Consequently, we tested and compared different linear designs.

The first characteristics to be taken into account is the resonant regime. According to the theoretical and experimental literature, a doubly-resonant (DR) operation would decrease the threshold [64, 92] of OPO operation, at the expense of the operational stability. Additionally, a design with a double pass of the pump beam would further increase the efficiency. In this thesis however, we choose to operate with single pass of the pump beam to minimize the risk of destabilization of the pump source due to strong feedback. All the linear resonators implemented in this thesis are DRO cavities.

For the cavity design, we mainly focused on three factors influencing the performances: the physical cavity length, the radius of curvature of the OC, and the output wavelengths. The IC used is always flat. The dependence on these factors is understood by the use of both simulations and experimental validations. Finally, a linear resonator is implemented and different ZGP crystals are tested. The best performing crystal is then chosen to characterize the cavity performances.

5.1.2. Influence of cavity length

The first aspect to be considered on designing a linear OPO is the length of the resonant cavity. On one hand, the shorter the cavity, the lower would be the oscillation threshold [93]. On the other hand, having a longer resonator assures a better beam quality [94, 95]. Thus, the length is usually chosen by a trade-off between these two effects, depending on the application.

In order to properly decide which length is the most suitable for our experimental setup, we used the SNLO software to simulate the OPO performances, focusing on the output power achievable. The simulation was ran for different cavity lengths and their results were compared. We considered for simplicity a linear resonator made by two flat mirrors. The IC is highly transmissive for the $2 \mu\text{m}$ pump ($R = 0 \%$) and high reflective ($R = 99 \%$) for the signal and idler wavelengths. The OC was instead considered transparent for the pump and partially reflective ($R = 50\%$) for the output beams. We only simulated a ZGP with a length of 20 mm. In particular, we simulated the CH#1, with absorption coefficient $\alpha = 0.033 \text{ cm}^{-1}$ (see Tab. 4.1). Before running the OPO simulation, we used the SNLO function Q_{mix} to evaluate the walk-off angles (around 11.3 mRad for both signal and idler) and the efficient nonlinear coefficient d_{eff} (77 pm/V) before using them as inputs in the 2D-cav-LP function. The physical lengths of the resonant cavity were varied, setting them to the values:

30 mm, 46 mm, 60 mm, 80 mm, 120 mm and 220 mm. The output power as a function of the input pump power obtained from this modeling is presented in Fig. 5.1.

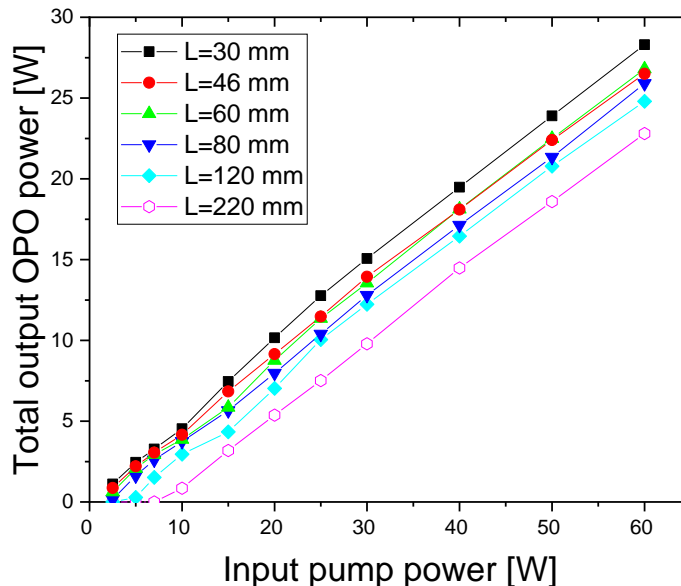


Figure 5.1: Simulated total (signal + idler) output power as function of the input pump power. Simulation by SNLO for various values of cavity length L .

We can observe that the threshold increases when the cavity length is increased, as expected. However, for values of L lower than 60 mm, the threshold remains virtually unchanged. The slope efficiencies also are comparable for such cavity lengths. The main difference is found when considering the highest output powers, where there is some variance between different resonator lengths. The shortest cavity length simulated ($L = 30$ mm) leads to the highest OPO output power obtainable, reaching a value of $P_{OPO} = 28$ W when considering 60 W of input power. However, when simulating $L = 46$ mm and $L = 60$ mm cavities, the maximum output power is equivalent, 27 W. For $L = 80$ mm, it drops to 26 W. We can therefore see that the absolute value of L does not affect dramatically the performances of the OPO in the range between 46 mm and 80 mm. As mentioned earlier, the SNLO software exaggerates the back-conversion in the crystal. This is evident when we consider the peak power as a function of time simulated by the program. In Fig. 5.2 they are presented for two input average power: 5 W and 20 W. From the temporal profile of the transmitted pump, we can see that after some nanoseconds of depletion, its power rises again. This is a clear sign of strong back-conversion. This effects is always present, but becomes more evident above 30 W of input average power. This behavior is the

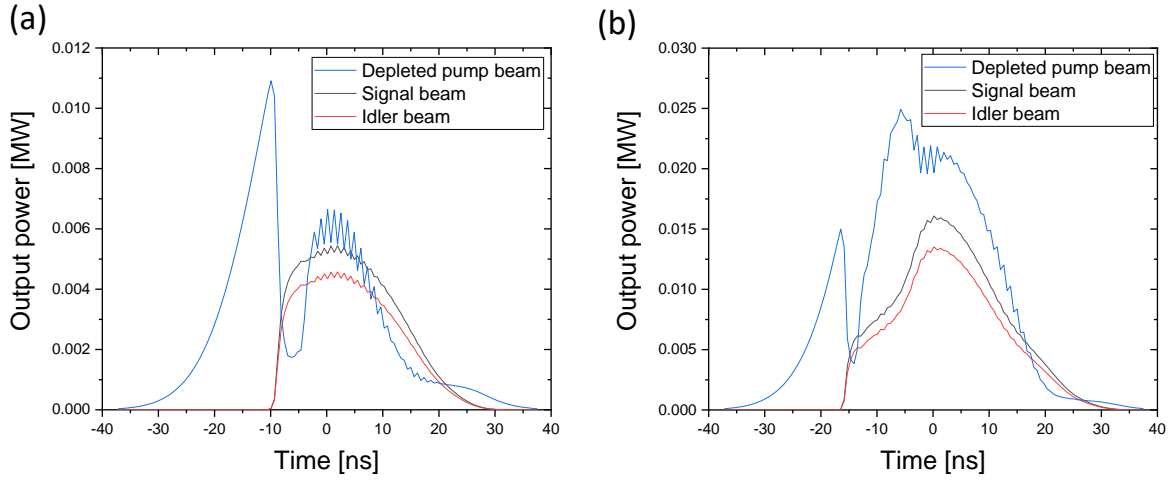


Figure 5.2: Simulated beams temporal profile of the three output beams taken at different input average power. (a) 5 W. (b) 20 W.

result of the fact that the spectra have been considered monochromatic. As a consequence, the back-conversion is greatly exaggerated in the program. Moreover, since SNLO does not take into account any thermal effects, the results at the highest input powers can only be roughly estimated. However, there is no reason to doubt the conversion efficiency at low powers ($P_{in} < 30$ W). As consequence, we might chose to implement the longest cavity length possible in this range in order to have the best beam quality of the outputs. However, we aim to compare the results from the linear cavity with the ones of non-planar ring resonators. As shown in Tab. 4.2, the RISTRA has a cavity round-trip of 173 mm. Hence, we decided to set the linear resonator to a physical length of 46 mm, corresponding to 178 mm optical round-trip. This assures to have good conversion efficiency and eventually to be able at the same time to compare the performances of the two resonators.

5.1.3. Influence of output coupler curvatures

The next aspect to be considered in the cavity design is the OC radius of curvature. As mentioned earlier in Chap. 3, to have the best performances, the pump beam should not excite transverse cavity modes different from the fundamental one. Thus, depending on the pump size, different OC mirror curvatures could be used. In our experimental setup, the pump beam diameter was set to $D = 1$ mm in order to avoid damage of the optics coatings used. Therefore, we want to find which is the best OC in order to allow good overlap between the fundamental cavity mode and the propagating pump beam.

To assess the issue, we utilized the function 2D-cav-LP of the SNLO software to simulate the OPO behavior for different curvatures radius of the OC (R_{OC}).

In addition to a flat mirror, we used the following values for the radius R_{OC} : 500 mm, 250 mm, 100 mm and 50 mm. During the simulation, we used the same set of inputs as used in Sec. 5.1.2 (DR regime, crystal absorption etc.). The length of the cavity was kept at a constant value of $L = 46$ mm. The output energy as function of the input energy for different R_{OC} is presented in Fig. 5.3.

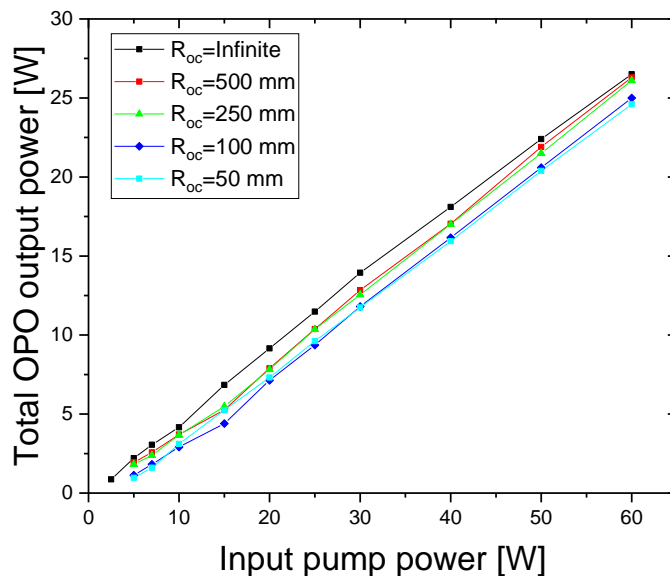


Figure 5.3: Simulated total output power as function of the input pump power simulated by SNLO for five values of OC radius of curvature R_{OC} .

We note that decreasing the OC curvature leads to higher threshold, which consequently leads to less OPO output power obtainable. For higher powers considered, mentioned in Sec. 5.1.2, we find that the back-conversion, exaggerated by the SNLO, hampers a trustful result. Despite this, we can notice that for our pumping conditions, it seems that the best would be to implement a resonator made by flat mirrors. However, we observe that an OC with $R_{OC} = 500$ mm and $R_{OC} = 250$ mm would lead to similar performances, at least for what concerns maximum output power.

This behavior is confirmed when we consider the fundamental mode size for the different R_{OC} . Using the LASCAD software [96], we simulated a planar-concave resonant cavity with different OC radius of curvatures. The ZGP crystal was accounted for by inserting a region of 20 mm between the two mirrors with a refractive index of 3.15. The simulation was done considering a beam $M^2=1$ and at the wavelength of 4.13 μm . The results of such simulation are presented in Fig. 5.4. The simulated values for the R_{OC} are: 50 mm, 100 mm, 250 mm, 500 mm, and 1000 mm. We can clearly see how according to the model

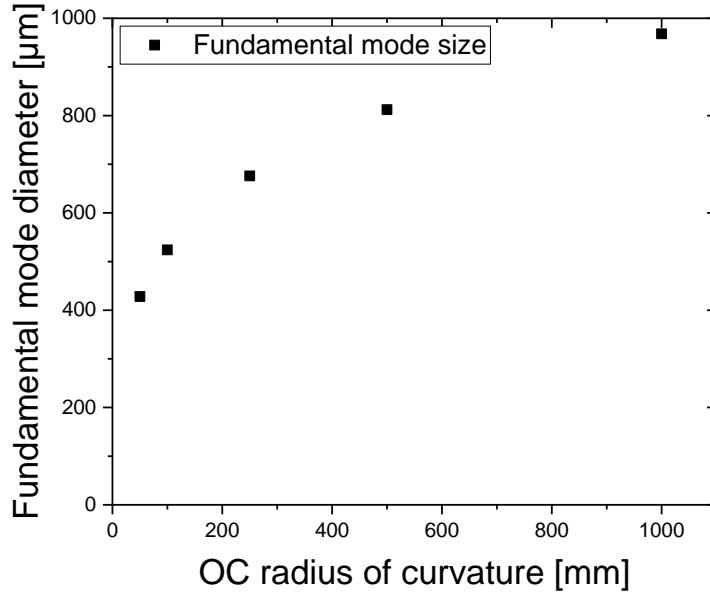


Figure 5.4: Simulated diameter of the fundamental mode in the resonator as a function of the OC radius of curvature. The input coupler was considered flat.

only when $R_{OC} = 1000 \text{ mm}$ the mode diameter is close to 1 mm, which is the size of our pump beam. The flat OC was simulated considering a radius of curvature of 10^6 mm , obtaining a mode diameter of approximately 4.6 mm. During these simulations, the thermal lens was neglected. If taken into account, the resulting mode size would be smaller. Since in the case of a flat OC the fundamental mode diameter is determined by the thermal lens, the simulation was improved in this case by inserting a relatively weak thermal lens with a focal length of 1000 mm. The resulting cavity mode size diameter is $968 \mu\text{m}$, the same value obtained when simulating $R_{OC} = 1000 \text{ mm}$. From these considerations, in our setup we can expect that the best performing resonator would be made by a flat OC.

To validate the simulations and to verify which OC is the most suitable for our setup, we experimentally tested the performances of them. We used the ZGP CH#1. We focused on the two best performing mirrors according to the simulations: flat and $R_{OC} = 500 \text{ mm}$ mirror. In Fig. 5.5 the output OPO power as a function of the input pump power obtained experimentally is presented for both OCs. To compare the performances, we limited the studies to the lower input powers (20 W). The experimental data were linearly fitted in order to recover slope efficiency and threshold. The flat OC leads to a threshold $P_{th} = 5 \text{ W}$ and to a slope efficiency of 54 %. The $R_{OC} = 500 \text{ mm}$ OC has a conversion slope efficiency of 53 % and threshold of $P_{th} = 4.5 \text{ W}$. Their conversion efficiencies

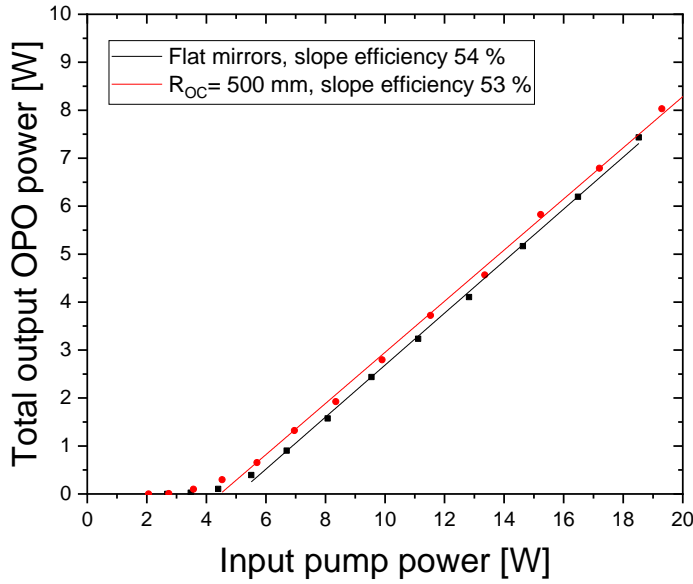


Figure 5.5: Experimental total OPO output power as function of input power obtained from a linear cavity with flat OC and a $R_{OC} = 500 \text{ mm}$.

and thresholds are very similar.

Judging only from the conversion efficiencies, we are not able to discriminate which OC to use. Hence, we analyzed the beam quality of the OPO output beams. In order to do that, as mentioned in Chap. 4, we focused the two beams with a $f = 250 \text{ mm}$ CaF_2 lens into the camera and we collected the focusing beam images at different distances from the lens. The beam diameters were then plotted and fitted according to Eq. 3.35. In Fig. 5.6 this measurement is presented for both types of OC considered. Both the signal and idler were investigated. The measures were taken at a comparable output power of approximately 2 W, so that the thermal effects were comparable between the two measures. This corresponds to an input power of approximately 8 W. The averaged signal M^2 value obtained using flat mirrors was $M^2 = 1.65$, while with the curved OC we obtained $M^2 = 1.9$. The same behavior was noticeable when considering the idler beams: $M^2 = 1.7$ (flat OC) vs $M^2 = 1.95$ (curved OC). Therefore, it is clear that in this conditions, the resonator with flat OC leads to a better beam propagation factor. An additional observation, independent of the used OC, is that the idler presents higher divergence with respect to the signal, resulting in a slight higher beam propagation factor, of around 0.1. This is expected when dealing with DR linear cavities [49].

The observations of these studies, taking into account the results of both the SNLO simulations and experiments, indicates that a pump diameter of 1 mm is better overlapping with the fundamental mode when using flat mirrors. There-

fore, we decided to implement a linear resonator made by two flat mirrors for the rest of the results presented.

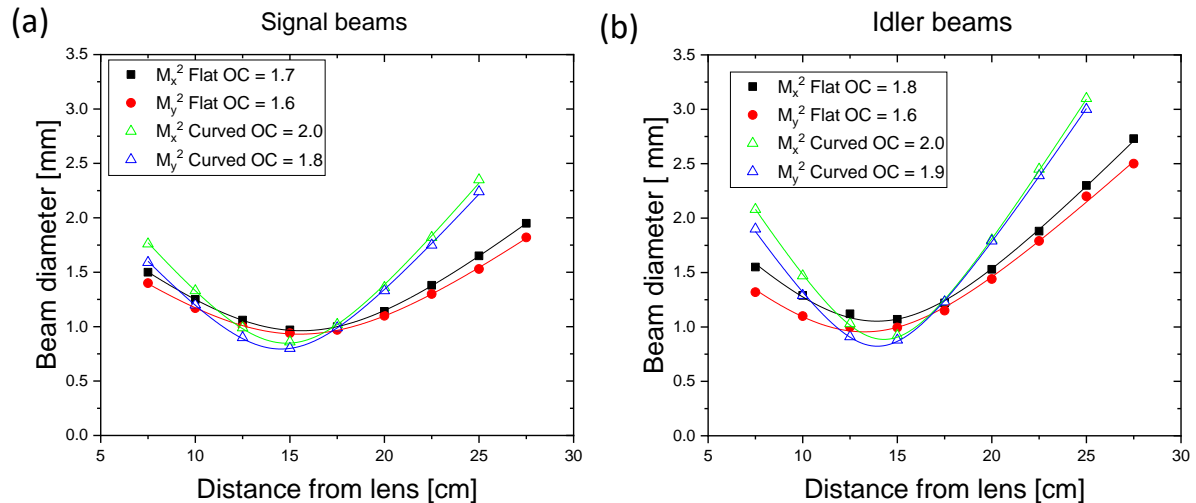


Figure 5.6: M^2 value measurement of the output beams of a linear resonator with flat and curved ($R_{OC} = 500 \text{ mm}$) OC. (a) Signal beam. (b) Idler beam.

5.1.4. Influence of output wavelengths

In the previous sections we have evaluated and chosen the design of a linear OPO. However, its performances depend also on the output wavelengths. In this section we will focus on this aspect.

As we know from theoretical considerations (see Eq. 3.15), the optical parametric gain depends on many quantities, among which are the output wavelengths [63]. This can also be simulated by the SNLO program, which calculates only the coupling constant from Eq. 3.15. To find the real parametric gain Γ , we need to multiply the SNLO data by the square root of our pump intensity, expressed in W/cm^2 . In Fig. 5.7 the result of such calculation is presented as a function of the signal wavelength. We considered 60 W of input pump power. The parametric gain reaches its maximum value at degeneracy, corresponding to $\lambda_s = 4.13 \mu\text{m}$. However, the variations are small, of the order of $10^{-4}/\text{cm}$. Therefore, to better model the behavior of the OPO, we simulated its performances, as we did in the past sections. The cavity was considered a DR, $L = 46 \text{ mm}$ linear resonator. The OC were considered to be flat. Different output wavelengths were reproduced. The output power as a function of the input power is presented in Fig 5.8. For simplicity, in the legend only the

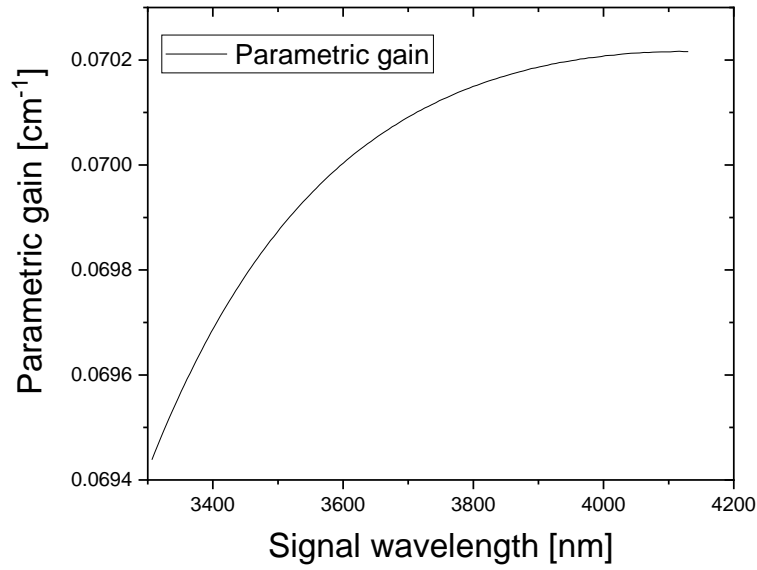


Figure 5.7: Simulated parametric gain as function of the signal wavelength.

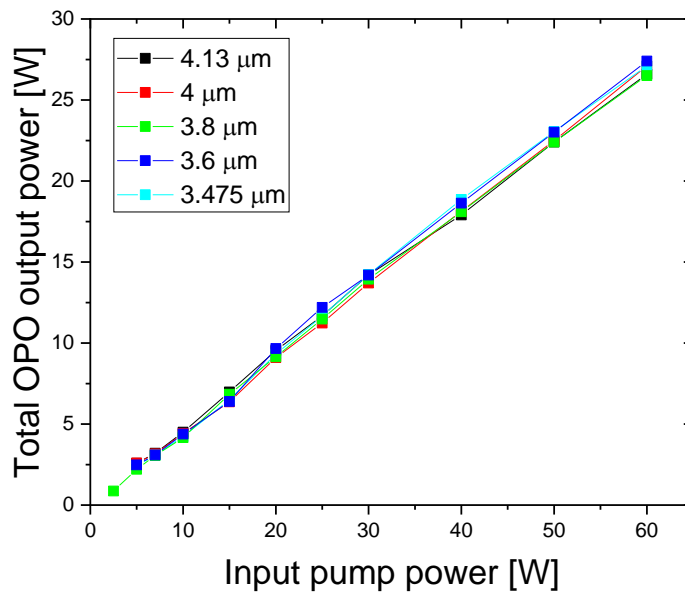


Figure 5.8: Simulated total OPO output power as function of input power for five different signal wavelengths.

value of the signal wavelength is depicted: $3.475 \mu\text{m}$, $3.6 \mu\text{m}$, $3.8 \mu\text{m}$, $4 \mu\text{m}$ and $4.13 \mu\text{m}$. Depending on the wavelength simulated, we replaced the refractive indices and walk-off angles according to the Q_{mix} function. We can immediately observe that the threshold doesn't depend on the wavelength used. Concerning

the slope efficiencies, the total output powers are visibly very similar, showing negligible dependence on the output wavelength. We can therefore state that the change in parametric gain given by the change of the output wavelengths is negligible in this wavelength range.

As we did when considering R_{OC} , we experimentally verified what would be the best operational conditions. Therefore, we compared the performances of a linear OPO with four different signal central wavelength: $3.475 \mu\text{m}$, $3.6 \mu\text{m}$, $3.8 \mu\text{m}$ and $4 \mu\text{m}$. In order to do that, we tuned the angle of the ZGP through the use of a rotational stage. We utilized the CH#1 and we implemented the usual cavity design: DR, flat, $L = 46 \text{ mm}$ linear cavity. In Fig. 5.9 the total OPO power as function of the input power is presented.

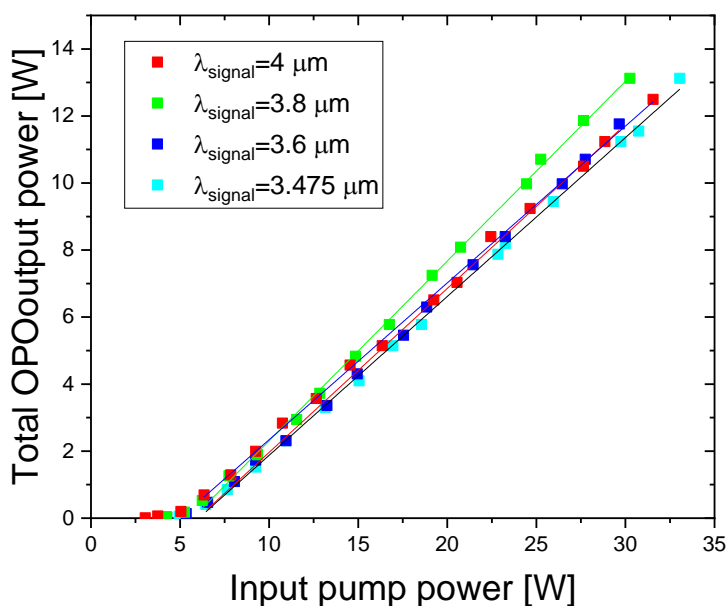


Figure 5.9: Experimental total OPO output power as function of input power obtained from a linear cavity when having different output signal wavelengths.

According to the manufacturer data, the reflection of the OC has the following values at the wavelengths considered: 50 % ($3.475 \mu\text{m}$), 49 % ($3.6 \mu\text{m}$), 47 % ($3.8 \mu\text{m}$) and 45 % ($4 \mu\text{m}$). The reflection of the IC at such wavelengths is instead constant at a value $> 99 \%$. As we can see, from the experiments no change in the oscillation threshold is observed, as expected from simulations. Its value is around 6 W of input pump power. Moreover, this proves how small variations in the OC reflection (of the order of few percents), does not affect the OPO performances. The slope efficiencies also are comparable. The only configuration the OPO is performing slightly better is where $\lambda_s = 3.8 \mu\text{m}$. Hence, for the rest of the results concerning the linear resonator in this thesis, we will implement a

cavity with this output wavelength.

5.1.5. Influence of crystal quality

Previously we mentioned that the performances of an OPO can vary depending on the quality of the specific crystal used. In this section we will therefore focus on this aspect. In order to do that, using the linear resonator implemented from the past sections, we experimentally tested the four available crystals, already presented in Tab. 4.1. All the experiments were conducted with $L = 46 \text{ mm}$, flat mirrors, DR regime, and output wavelengths of $\lambda_s = 3.8 \mu\text{m}$ and $\lambda_i = 4.52 \mu\text{m}$. The graph in Fig. 5.10 shows the total OPO output power as a function of the pump power for all the ZGPs tried.

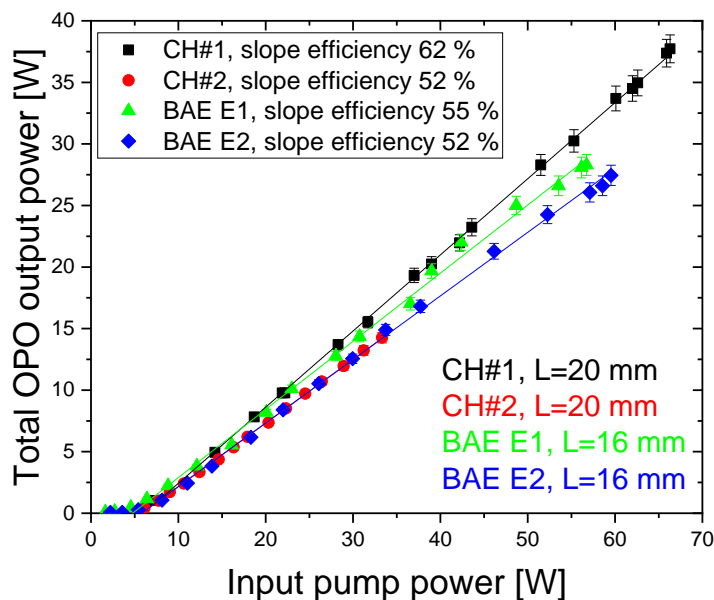


Figure 5.10: Experimental total OPO output power as a function of input pump average power for the four ZGP crystals used in linear resonator (178 mm optical round-trip, doubly resonant regime, flat output coupler).

It appears from the graph that strong back-conversion is absent in our experiments, as visible from the always-linear behavior for the OPO output. This is in contrast with the previous SNLO simulations, highlighting how considering monochromatic spectra hampers the trustfulness of the modeling for highest power values. The oscillator thresholds are comparable between the four crystals (around 6 W), but the slope efficiencies are different. We notice that there is one crystal that is performing better than the others, the CH#1. The OPO, based on this 20 mm ZGP crystal, has a slope efficiency of $62.2 \pm 0.3 \%$. This crys-

tal is also the one with the lowest absorption at the pump wavelength (6.4 %). As expected, the absorption has an influence on the maximum output power achievable from the OPO. The ZGP with the highest absorption leads to the lowest slope efficiency. Indeed, the CH#2 and the BAE E2 crystals, both with approximately 8.4 % pump absorption, have a lower 52 % slope. Their curves visibly superimposed each other in Fig. 5.10. Since it was having the same results than BAE E2, the CH#2 crystal was not tested up to full pump power in order to avoid any risk of damage. Despite being only 16 mm long, the BAE E2 crystal gives the same results than the 20 mm long CH#2 crystal. The reason could be that in a longer crystal the back-conversion and walk-off effects, although small, play a negative role. Further investigations are needed in order to explore this feature. It should be possible to find an optimal crystal length for OPO operation. The last ZGP tried was the one named BAE E1, with a power absorption of 7.5 %. Consequently, it has intermediate performances, with a slope efficiency of 55 ± 1 %.

The CH#1 crystal appears to be the best candidate for high power generation. However, we have to consider also the beam propagation factors of the two output beams. The beam quality of the signal and idler at low average power, i.e. negligible thermal effects, depends exclusively on the cavity length and geometry [81, 97]. Therefore the M^2 factor just above threshold should not differ between the crystals. Up-scaling the output power leads to a deterioration of the output beam quality due to the rise of a thermal gradient in the ZGP and consequently thermal lens [71]. This effect should be more evident for the crystals having higher absorption coefficients. However, the difference of pump absorbed between the crystal of lowest (CH#1) and highest (CH#2) absorption is around 2 %, corresponding to approximately 1.2 W if we consider 60 W of input power. So, we wonder if this leads to a measurable difference between the M^2 values or it is instead negligible. To ascertain it, we did experimental measurements on the M^2 factor. In Fig 5.11 the variation of the signal beam quality M^2 value as function of the pump power is presented for three crystals. The CH#2 was not measured since its performances are comparable to BAE E2. The values depicted are the average between horizontal (X) and vertical (Y) directions. Above threshold, where the thermal effects are low, the beam propagation factors is around 1.5 for the three ZGPs. Then, as the thermal load into the crystals increases, the beam quality factor deteriorates due to the arise of a thermal lens. The M^2 value for a input power of approximately 60 W is 2.2. This is independent on the crystal used. From this results we can conclude that, even though the beam quality factor is deteriorated by the absorbed pump power, the difference between the crystals used in our case is negligible. Therefore, in the same operational conditions, they yield the same M^2 output values.

As a conclusion, in the next section we will characterize the linear OPO cavity with the crystal giving the highest output power, i.e. CH#1.

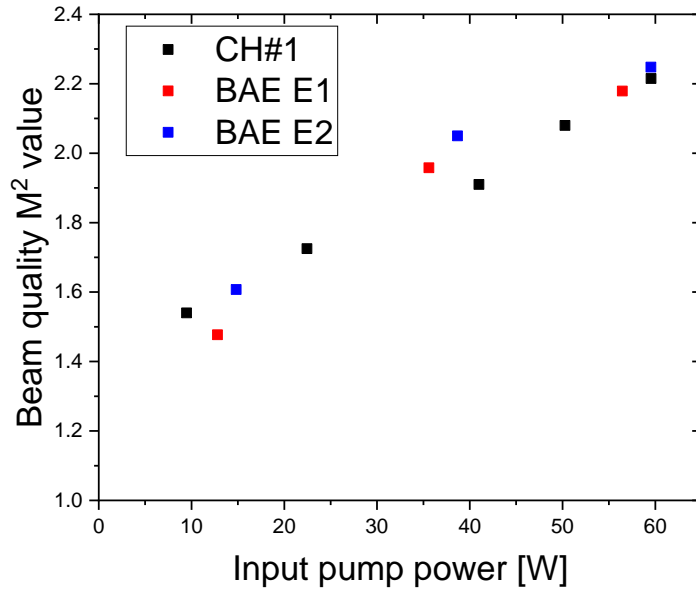


Figure 5.11: Experimental variation of the signal beam quality M^2 factor with input pump power for three different ZGPs: CH#1 (black squares), BAE E1 (red circles), and BAE E2 (blue triangles).

5.1.6. Characterization of the linear OPO cavity

In this section we present and discuss in detail the experimental results obtained from a linear resonator with the best performing ZGP, the CH#1. It was grown and coated at the Harbin Institute and has an absorption coefficient of $\alpha = 0.033 \text{ cm}^{-1}$. The total output power (signal + idler) as a function of the pump power is presented in Fig. 5.10 (black squares). Operating at a repetition rate of 10 kHz, we achieved a total output power of 38 W (3.8 mJ) for 66 W of input power, corresponding to a slope efficiency of 62 %. The optical-to-optical efficiency is calculated as the ratio between the input pump power and the total OPO output power. Its maximum value, achieved at the maximum power, is 57 %. As mentioned in Sec. 4.1.4, this resonator geometry presented power instabilities due to back-reflection. The IC indeed reflects approximately 5 % of the $2 \mu\text{m}$ power back into the pump source. At power levels above 20 W, this hampers the stability of the $\text{Ho}^{3+}:\text{LLF}$. Hence, in order to operate above these power levels, we had to slightly misalign the cavity and the pump beam, since optical isolators are not commercially available at this power level (they are typically limited at approximately 40 W). This was done acting on the IC, tilting the back reflection in the Y direction. The resulting power fluctuations of the OPO and the pump source are presented in Fig. 5.12. The stability of the OPO was not measured at maximum output power in order to monitor the pump source at the same time in order to correlate their fluctuations. The measure was done

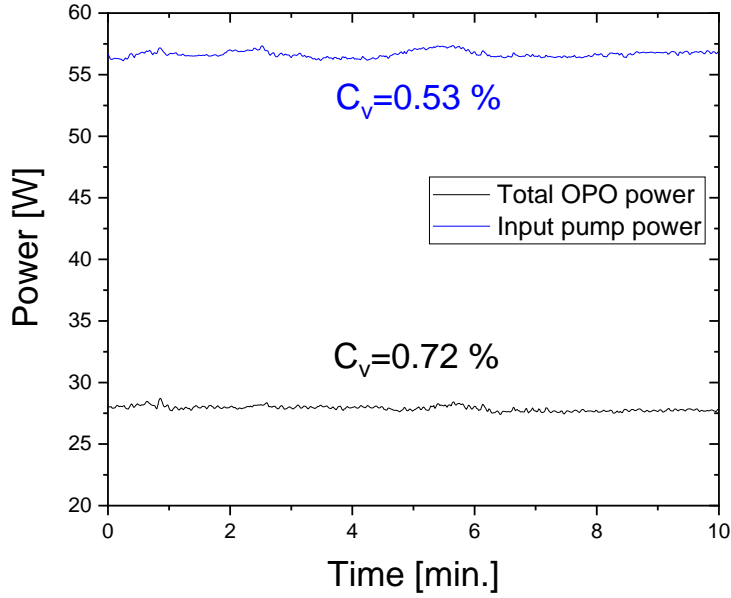


Figure 5.12: OPO and pump stability measurement at $P_{OPO} = 28 \text{ W}$ over 10 minutes. The labels indicate the corresponding relative standard deviation.

over a period of 10 minutes, with 1 second sampling time. For an average input power of $56.7 \pm 0.3 \text{ W}$, we measured an average OPO output of $27.9 \pm 0.2 \text{ W}$. Therefore the OPO output power has a higher relative standard deviation (C_v) than the pump power over a period of 10 minutes (0.72 % vs 0.53 %). From the graph, it is visible that the OPO output fluctuations follow the trend of the pump. This power stability confirms how our flat, linear resonator is in a stable operation condition. In addition, HgCdTe infrared detectors were used to collect the OPO pulses at various output power levels: 2.8 W, 11.8 W, 23.5 W and 35 W. In Fig. 5.13 these measurements are presented.

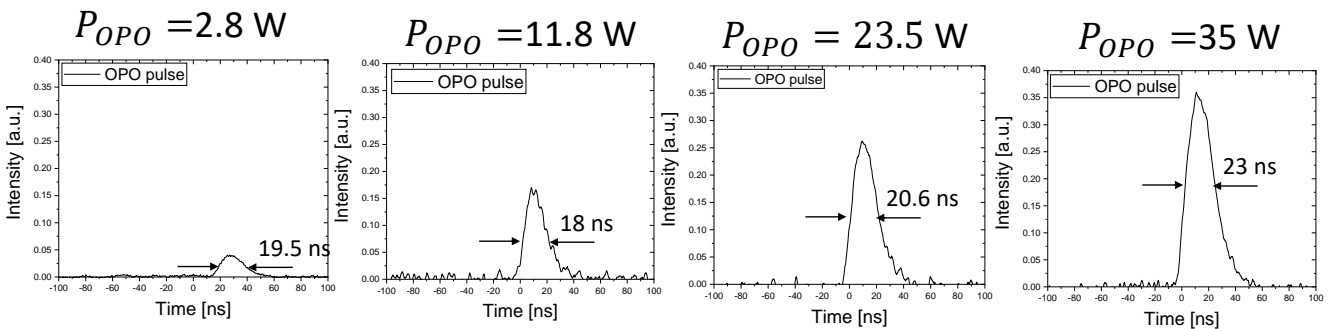


Figure 5.13: Temporal pulse profiles of the OPO (signal + idler) at various output power.

The pulses were fitted according to the standard Gaussian function in order to evaluate their widths, which are indicated in the corresponding labels. As the power increases, the pulse widths also increase, as a consequence of the additional power converted. The shape of the pulses measured clearly show that there is no strong back-conversion during our experiments, in contrast with the SNLO simulations previously done. At maximum power, the FWHM was measured to be 23 ns, corresponding to a peak power of 165.2 kW.

To better characterize the cavity, we must also measure the beam quality of the two output beams. In the previous section, we saw that as the amount of heat in the nonlinear crystal scales with the input power, it induces a positive thermal lens. As a consequence, the beam quality deteriorates as the incident power increases. In Fig. 5.14 this dependence on the input power is presented for both signal and idler beams.

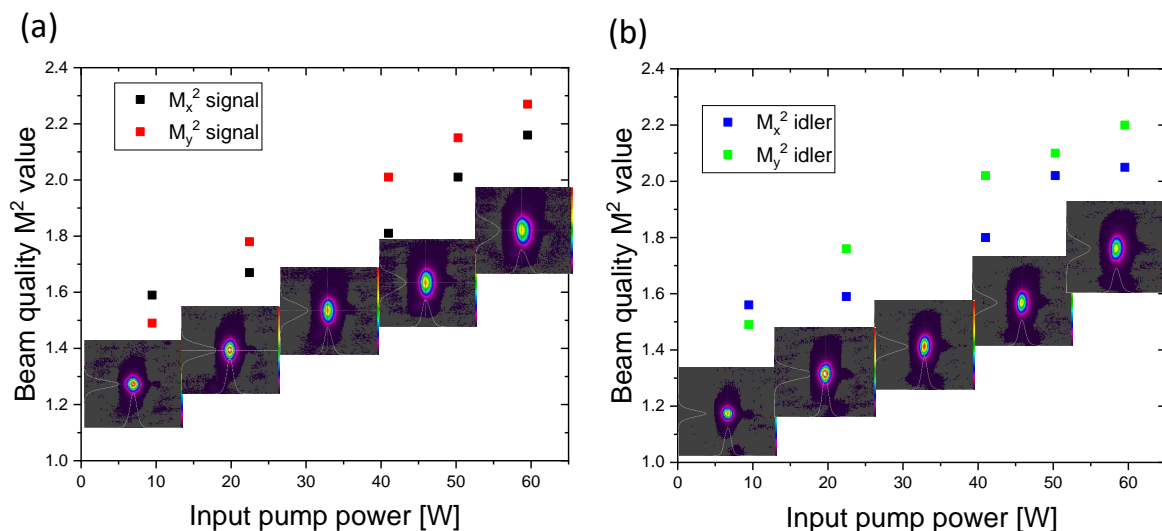


Figure 5.14: Variation of the beam quality M^2 factor with input pump average power. The corresponding near field images at a distance of 25 cm from the lens are shown. (a) Signal. (b) Idler.

We can notice that the signal and idler do not present any significant difference between each other. Their beam propagation factors are comparable in the two perpendicular directions. The average M^2 values at 9.5 W of input power are 1.5 for both beams. With the increase of the power, both propagation factors deteriorate, reaching a value of 2.2 and 2.1 for signal and idler, respectively. The M^2 value measurements at maximum input power of the two beams are presented in Fig. 5.15. From the beam diameters measurements, we can notice that the beams shapes present ellipticity and are not symmetric. This behavior appears more clearly as the power increases, as we can see when looking at the beam

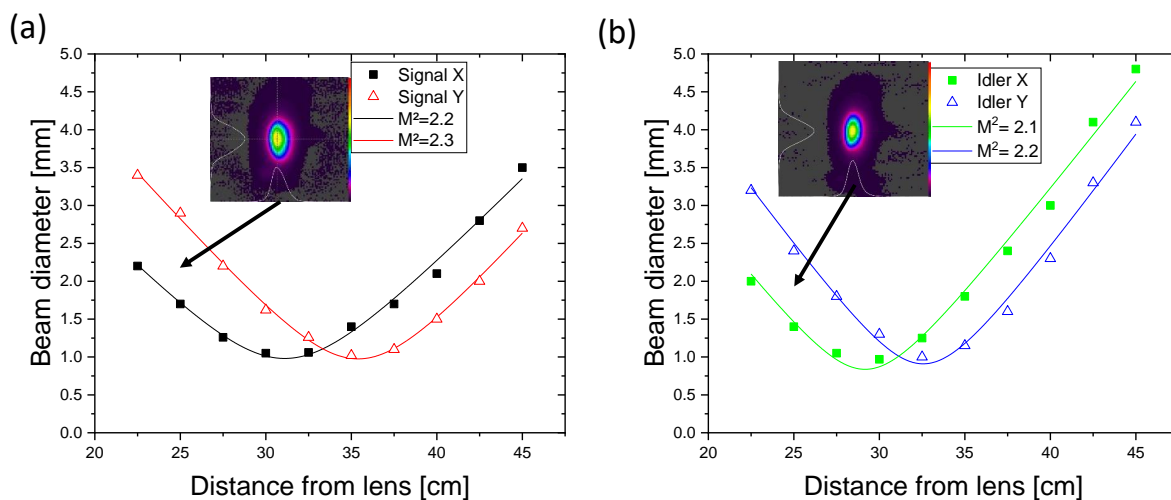


Figure 5.15: M^2 value measurement at maximum input power of 60 W. (a) Signal. (b) Idler.

spatial profile at different pump powers, depicted in Fig. 5.14 close to the corresponding data point. The beam images shown are near-field images taken at a distance of 25 cm from the lens, corresponding, for the last picture of signal and idler, to the second data point in Fig. 5.15. The distortion of the beam shapes is due to two reasons: the walk-off effect, and the cavity misalignment, deliberately introduced to avoid back reflection and optical feedback to the pump laser. Such misalignment, done in the vertical direction, did not affect dramatically the M^2 values in the Y direction, which remained comparable with the M_x^2 .

The output power and the beam quality reported here exceeds previous reports from linear doubly-resonant ZGP OPOs [49, 98]. The demonstrations of higher output powers from single-stage ZGP OPOs used different resonant regime and planar ring resonators [54, 53]. However, the reported beam quality factors were $M^2 \approx 4$ at 30 W of output power and $M^2 \approx 4.3$ at 41 W, respectively. Therefore, at comparable output powers, we recorded better beam quality, despite the use of a linear resonator. In accordance with our results are those reported by Lippert et al. [56]. They obtained 22 W of output power with M^2 of 1.4 in a V-shaped 3-mirror ring cavity.

All aforementioned studies demonstrate how challenging is to conciliate high power operation and low beam propagation factors. The results presented in this study are currently pump power limited and they could be further up-scaled. The main limitations are the laser damage threshold of the optics involved, and the back-conversion. The latter is still a weak effect in our experimental conditions, but could become an issue for higher pump powers, as pre-

dicted by SNLO.

5.2. Performances of non-planar ring resonators

5.2.1. Motivation

As the previous discussions on the linear resonator demonstrated, the main challenge in the development of high average power OPOs is to maintain a good beam quality with a simple and compact architecture. In principle, the mode discrimination could be improved by increasing the OPO cavity length. However, when the efficiency and compactness of the overall system are crucial, this method is not applicable. The most troublesome are the thermal effects leading to the build-up of higher order modes in the cavities and consequent degradation of the beam quality. One way to counter the thermal lens is direct compensation with intracavity negative lens. This approach was proven effective in the demonstration of a 102 W MOPA system [55]. However, the compensation with elements of fixed dioptric strengths is limited to systems of well-characterized and known thermal lens, but very often its dynamic nature is not studied carefully. Another well-established technique to improve beam quality in OPOs is a ring resonator with a non-planar configuration of mirrors. Such resonators and their effect on beam quality improvement were first investigated by *Smith et.al.* [57]. Two particular types of non-planar image rotating ring resonators have been proposed and proved successful in beam quality improvement: the 90° Rotated Image Singly-resonant Twisted RectAngle (RISTR) [58] and the Fractional Image Rotation Enhancement (FIRE) [59] cavities. The RISTR as an OPO resonator was proven to be effective and advantageous compared to planar resonators in many later demonstrations of high power and high energy OPOs [62, 73]. Alternatively, the FIRE cavity is of particular interest as it has never been tested before at high power operation, although it has proven to deliver good beam quality in high energy low repetition rate systems [85]. Additional studies for the FIRE resonator implemented intracavity negative lens [61] and a Galilean telescope [52].

In this context, we have experimentally tested these two non-planar ring cavities, characterizing their performances. The main aim is to improve the beam quality of the signal and idler beams. The first choice was to use the best performing ZGP (CH#1). However, dust contamination caused coating damage at moderate pump power during the previous experiments. This damage prevented us from using it in the RISTR and FIRE cavities. Therefore, a second ZGP had to be used. Although from Fig. 5.10 we can see that the BAE E1 is performing slightly better, we decided to implement the CH#2. The reason was that in order to compare with the previous results obtained in the linear cavity, we preferred to keep the crystal length unchanged (20 mm).

5.2.2. The RISTRA resonator

The first non-planar ring cavity studied was the RISTRA. Its physical cavity length is 130 mm, corresponding to 173 mm optical round-trip. In this case the resonator was operating in singly resonant regime, with the OC being partially reflective ($R = 50\%$) at signal wavelength and highly transmissive for pump and idler. The input power available in this case was lower (59 W) due to the transmission of the input coupler ($T = 86.3\%$). The total output power as function of the input average power is presented in Fig. 5.16.

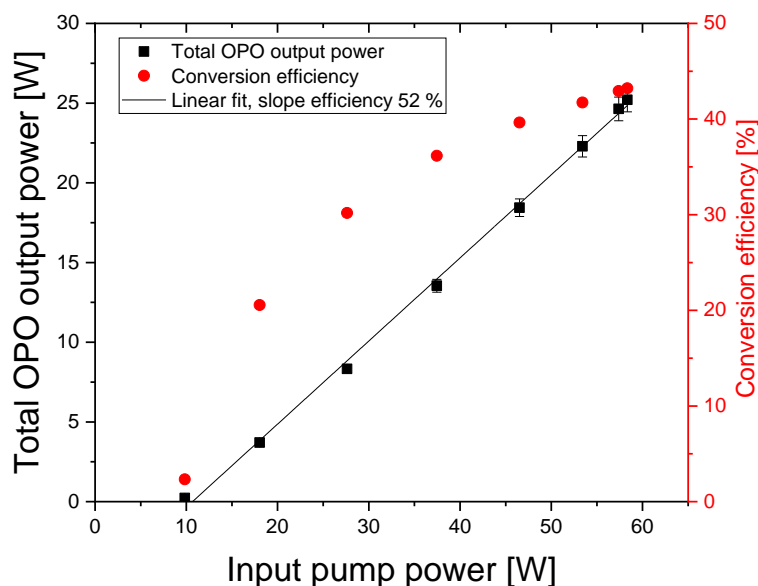


Figure 5.16: Total OPO output power and conversion efficiency as a function of the input pump power in RISTRA.

We achieved a total output power of 25.2 ± 0.7 W for 58 W of input power, with a slope efficiency of 52 %. The optical-to-optical efficiency is presented as red circles and its value at the maximum output power was 43 %. The threshold, calculated from the linear fit, was 10.7 W. Contrary to the linear resonator, the RISTRA did not need any misalignment in order to obtain stable operation. In Fig. 5.17 (a) the stability measurement done at an intermediate output power level, to monitor at the same time the pump power, is presented.

The average input pump power was 36.1 ± 0.3 W, corresponding to a relative standard deviation $C_v = 0.83\%$. The OPO power instead was measured at an average value of 13.4 ± 0.3 W ($C_v = 2.23\%$). We can notice a small drift in power with time, that however is related to the pump source, which also presents such a drift. The pulses at different output powers were also collected. The average of 128 pulses was recorded, normalized and fitted according to the Gaussian statistics. They are presented in Fig. 5.17 (b). They were measured at the P_{OPO}

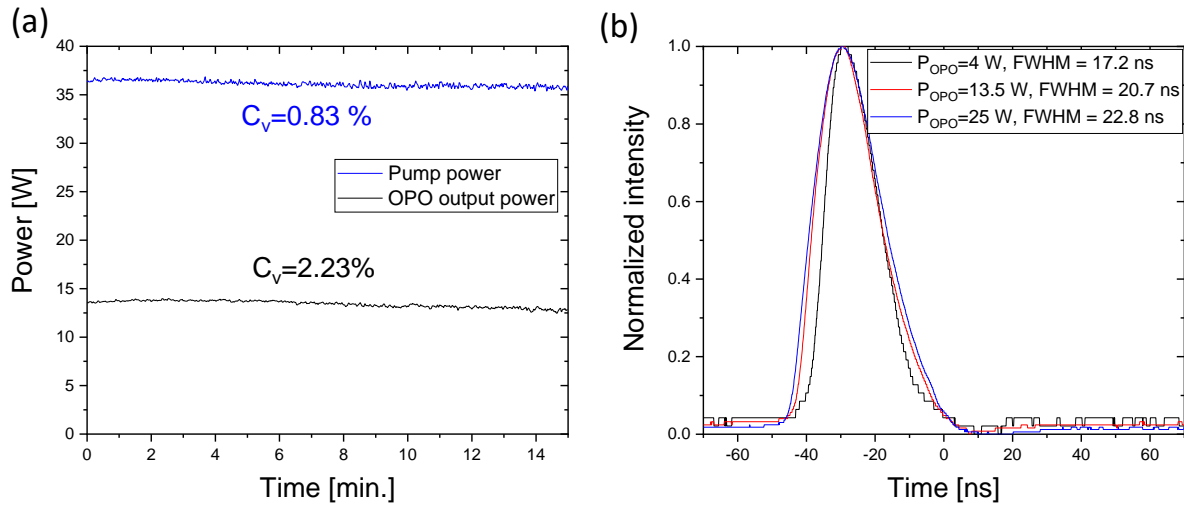


Figure 5.17: (a) OPO and pump power stability measured over 15 minutes. The labels indicate the corresponding relative standard deviation. (b) Normalized temporal pulse profiles of the OPO output at different power levels.

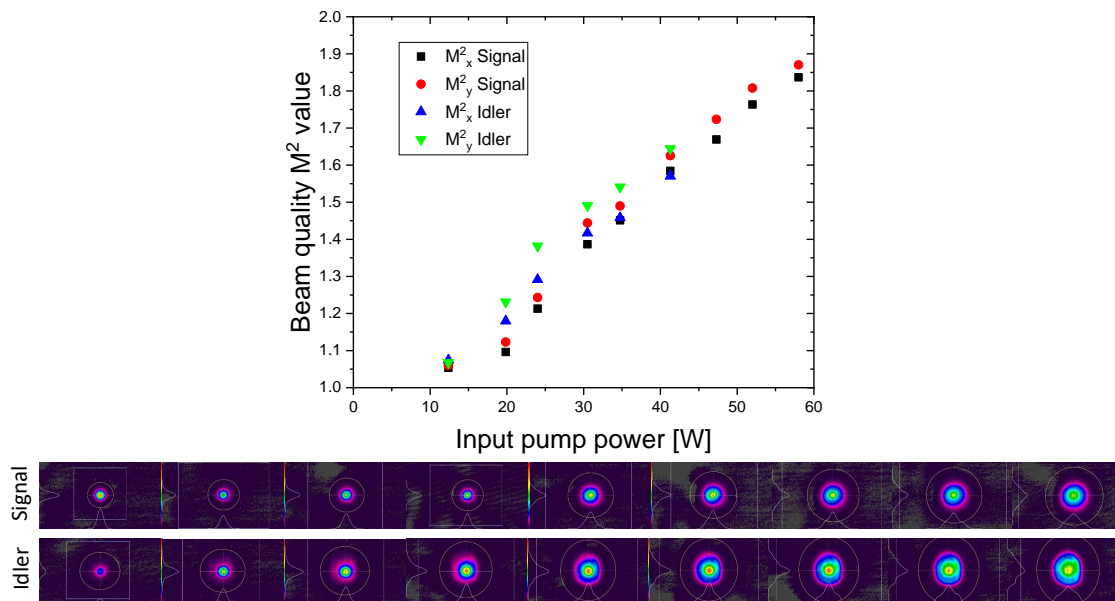


Figure 5.18: Variation of the beam quality M^2 factor with input pump power for signal and idler in the RISTRA resonator. Below are near-field beam images (taken 80 cm after the focusing lens) corresponding to each data point.

of: 4 W, 13.5 W, and 25 W. The pulse widths increases as the power increases, similar to how they behaved for the linear resonator in Sec. 5.1.6. The pulse duration (FWHM) measured at maximum power was 22.8 ns, corresponding to a peak power of 110.5 kW. The beam quality factors M^2 of the OPO signal and idler beams as a function of the pump average power are presented in Fig. 5.18. The two rows of images in the bottom are near-field signal and idler beam images taken at the position 80 cm after the focusing lens. Close to threshold, at a pump power of 12 W, corresponding to 1.6 W of output power, the beams are nearly diffraction limited. For the signal beam, they assume an M^2 value of 1.06 in both directions. The beam propagation factors then increase, reaching at the maximum power ($P_{in} = 58$ W) a value of 1.84 and 1.87 in the horizontal and vertical direction, respectively. If we consider the idler, from the first data points we can see that it follows the same trend as the signal beam. However the beam propagation factors measured are slightly higher, as already seen when studying the linear resonator in Sec. 5.1.6. Because the idler beam has a much larger divergence than the signal, it was clipped by the 1-inch optics. This can be clearly noted when looking at the corresponding beam images. Consequently the M^2 measurement at the highest power could not be performed, that is the reason for a lack of the last 3 data points for the idler in the graph. There is no reason for a deviation from the trend, thus similar behavior can be anticipated.

As mentioned previously, the RISTRA cavity operates in singly signal resonant regime. The ZGP was tuned to have a central wavelength of the signal $\lambda_s \approx 3.6 \mu m$. We investigated how the thermal load affects the spectra of the output beam. Therefore, we collected the signal spectra at different output power levels. The corresponding measurements are presented in Fig. 5.19. According to available data for non-critical phase-matching in ZGP, as the crystal temperature increases, the wavelengths should shift closer to degeneracy. We have hence to determine if the central wavelength is moving with the input power. The envelope of the peaks is given by Eq. 3.14. Thus, we can evaluate the central λ_s at each power level by fitting such equation. The position of each individual peak inside the envelope is instead given by the resonator geometry, as explained in Chap. 3. Indeed, since the crystal is not cooled, we can notice a red-shift of the signal output wavelength. Its initial value close to threshold is $\lambda_s = 3562$ nm, it then increases with the power, reaching $\lambda_s = 3592$ nm at the maximum output power of 25 W. As explained in Sec. 3.2.1, the cluster effect is typical of DRO cavities. However, the RISTRA is singly resonant and this modulation can still be seen in the spectra. A possible explanation could be that a small portion of the idler is still circulating within the resonator, adding an additional constrain on the wavelengths. If we calculate the cluster frequency spacing according to Eq. 3.23 for our experimental conditions, we obtain a $\Omega_s \sim 1$ THz, which if we consider $\lambda_s = 3.6 \mu m$ corresponds to around 40 nm. The experimental value obtained by Gaussian fitting the multiple peaks in Fig. 5.19 is approximately 25 nm, therefore the same order of magnitude.

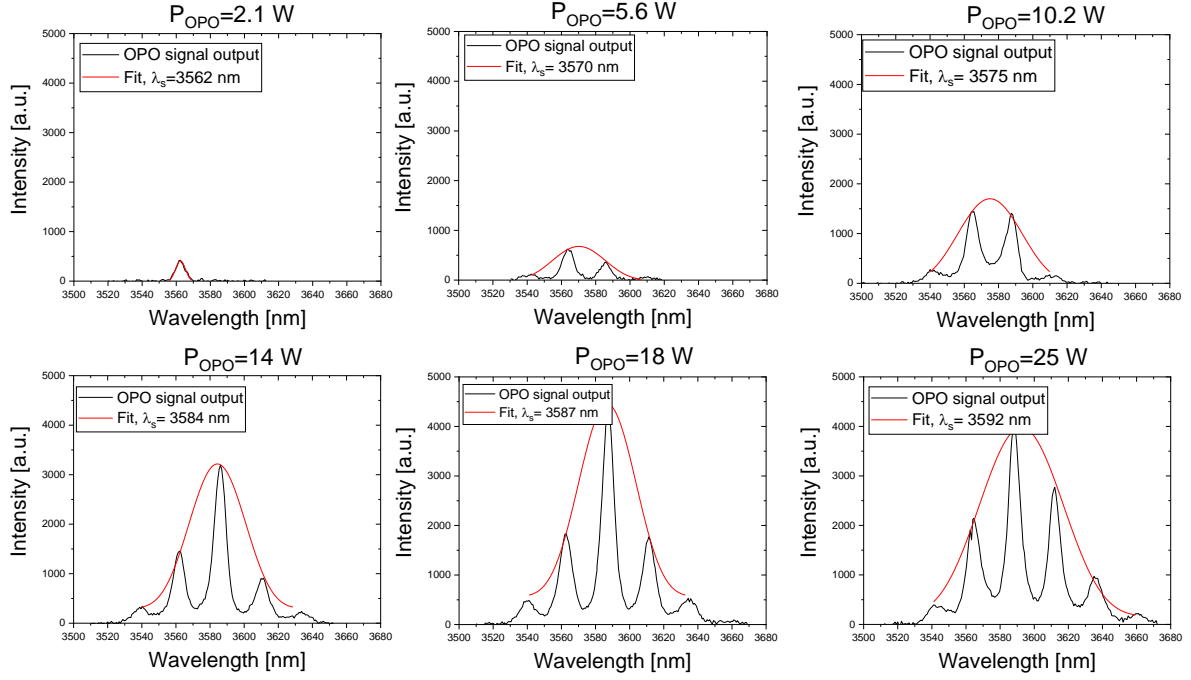


Figure 5.19: Output spectra of the signal beam in the RISTRA for different OPO output powers.

Further studies are however needed in order to address the difference between these experimental and theoretical values.

5.2.3. The FIRE resonator

The second non-planar ring cavity studied was the FIRE. Contrary to the RISTRA, it was never tested at high average power in the past, but it has proven that it could further improve the beam quality factor in low repetition rate systems [59, 61]. The physical cavity length is 222 mm, corresponding to an optical round trip of 265 mm. The same mirrors used for the RISTRA were employed. Hence, the FIRE is operating in singly signal resonant regime as well. The IC in this case has a transmission at the pump wavelengths of 84 %, lowering the pump power available (55 W). The total output power as a function of the input average power is presented in Fig. 5.20. Pumping with a maximum input power of 52 W, we achieved an OPO output of 21.1 ± 0.6 W, corresponding to a maximum optical-to-optical efficiency of 40 %. According to the linear fit, the threshold is 12 W, while the slope efficiency is 50 ± 1 %. Concerning the operation stability, in Fig. 5.21 is presented the stability measurement done at an intermediate power level. For an average power of input 42.25 ± 0.05 W ($C_v = 0.12$ %), the OPO output power was measured to be 10.7 ± 0.2 W, corresponding to a $C_v = 1.87$ %. Pulses of the OPO at different power levels were also

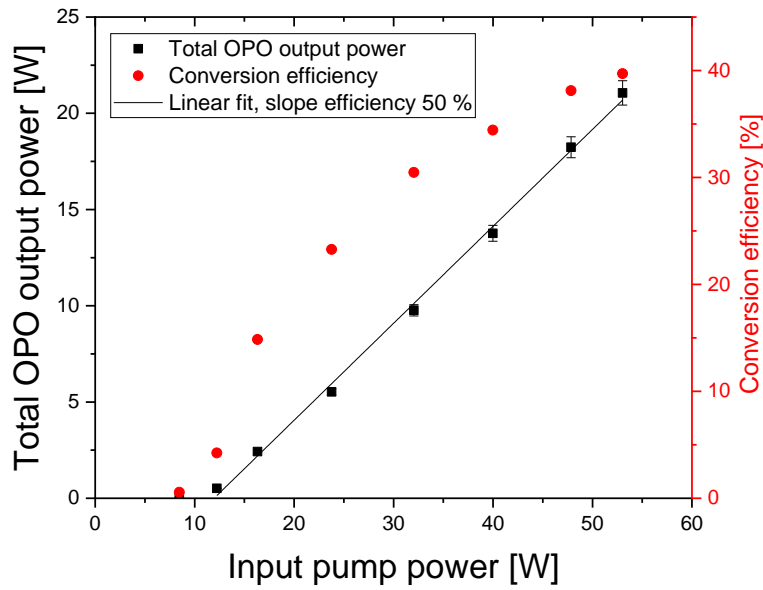


Figure 5.20: Total OPO output power and conversion efficiency as a function of the input pump power in FIRE.

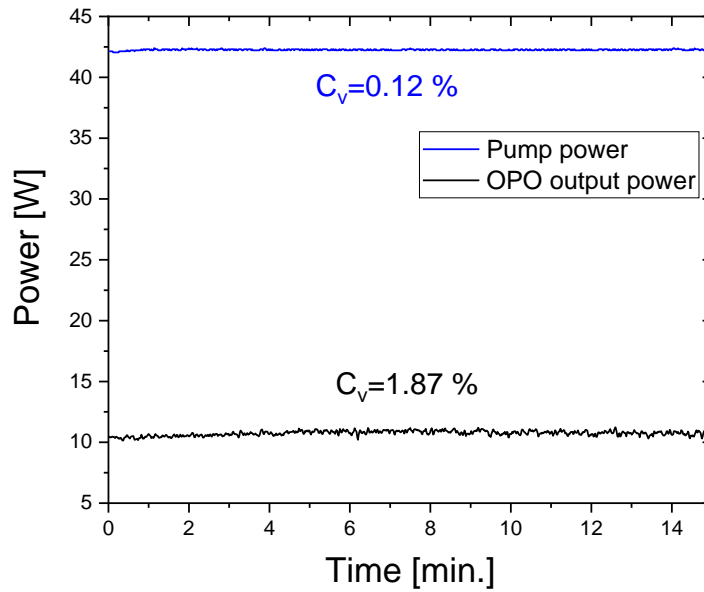


Figure 5.21: OPO and pump power stability measure over 15 minutes. The labels indicate the corresponding relative standard deviation C_v .

collected, and their are shown in Fig. 5.22 (a). They were recorded at an output power of : 3 W, 10.6 W and 21 W. The pulse width at maximum output power is 16.7 ns, corresponding to a peak power of 125.7 kW. However, in this case,

the increase of the pulse duration with the power is less significant. To exclude problems of back-conversion, we recorded the depleted pump pulse profile at maximum power, presented in Fig. 5.22 (b).

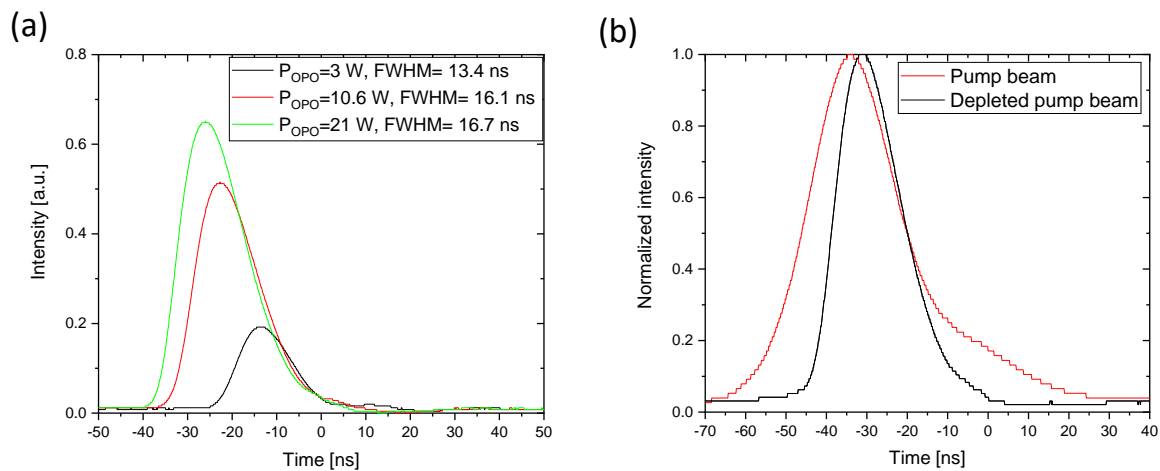


Figure 5.22: (a) Temporal pulse profiles of the OPO output at different power levels. (b) Temporal pulse profile of the input and depleted pump beam. The measures were done with a 5 ns time resolution.

Its shape shows no sign of such effect. For comparison, the pump pulse before the entering the OPO is also shown. The rising slope of the two pulses recorded are different due to the different detector used.

The signal beam quality variation as a function of the input power was measured, finding a similar scaling as for the other cavities. In Fig. 5.23 the measurement at maximum power level is presented. Since in the linear and RISTRA resonators the idler beam followed the same trend as the signal, we did not perform beam quality analysis of the idler for the FIRE. An M^2 factor of 1.4 was found in both direction at maximum power. The beam diameters indicate small ellipticity of the beam, as we can also see from the images recorded.

The crystal angle, as well as its copper mount, were not changed with respect to the RISTRA experiment. Therefore the output wavelengths are identical. The thermal load responsible for the shifting and broadening of λ_s with the power seen in Fig. 5.19, also remains unchanged.

5.3. Comparison of linear, RISTRA and FIRE resonators

In the previous sections we studied the performances of three different OPO cavities. In order to highlight the main advantages and drawbacks of each res-

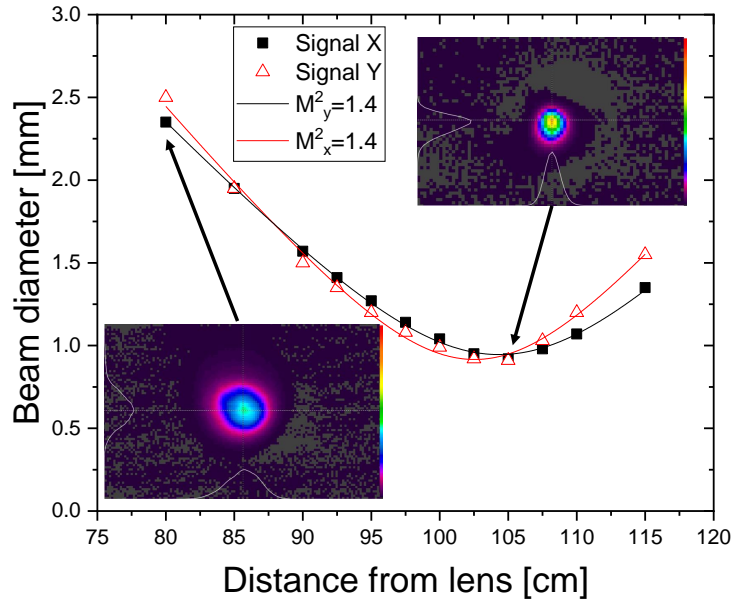


Figure 5.23: Signal M^2 value measurement at maximum input power of 52 W.

onator, their results must be directly compared.

The total OPO output power as a function of pump average power for the three cavities is presented in Fig. 5.24. Using the CH#2 crystal, we achieved a total output power of 25 W (RISTRA) and 21 W (FIRE) in the 3-5 μm range. The input power available in this case was lower due to the transmission of the ICs. The crystal was not tested at full pump power in the linear cavity to avoid any possible damage. However, from the slope and threshold it can be anticipated that it would give approximately 28 W of total output power when pumped with 60 W (dashed line). The slope efficiency is around 50 % for each resonator. More specifically, their values are: 52 % (linear and RISTRA) and 50 % (FIRE). It neither depends on the cavity resonant type nor the cavity geometry. The main difference among the cavities is the oscillation threshold. As the optical length per round trip of the linear and RISTRA cavities are comparable, it can be stated that the doubly-resonant regime lowers the oscillation threshold. This agrees with previous theoretical [64] and experimental [92] reports. Additionally, if we compare the FIRE and RISTRA cavities, the dependence of the threshold on the cavity length can be observed. Since FIRE is singly-resonant and the longest, its threshold is the highest. The results for the CH#1, presented in Sec. 5.1.6, are also showed.

Concerning the stability, all the three cavities were stable and could operate for several tens of minutes. However, it must be reminded that in order to obtain stable operation, the linear resonator had to be misaligned, while the RISTRA and FIRE had not such issue. The normalized pulse at maximum power

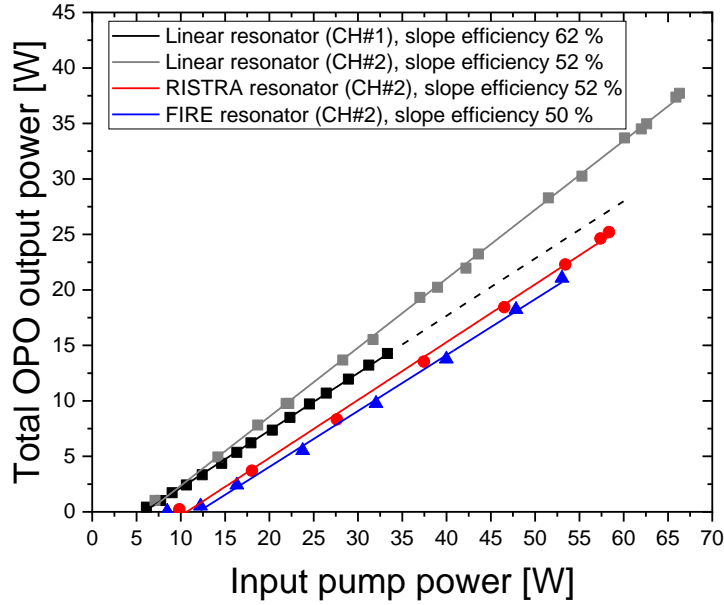


Figure 5.24: Total output power as function of the input power in three cavities: a linear cavity (black squares), a RISTRA cavity (red circles), and a FIRE cavity (blue triangles). The grey squares represent the performances of the CH#1 in linear cavity, as shown in Fig. 5.10.

is presented for the three cavities in Fig. 5.25. Having the RISTRA and linear comparable optical round-trip length, their build-up time is similar. Hence, the output pulses also present no significant difference, with comparable widths at maximum power. The FIRE instead, having a higher L , leads to shorter pulses duration [99].

Concerning the beam propagation factors, Fig. 5.26 shows the variation of the M^2 value as a function of pump power for the three cavities, averaged between X and Y directions. As seen in Sec. 5.1.5, the beam quality of the output beams is identical regardless of the specific ZGP used. Therefore, even though we haven't measured the M^2 value for the CH#2 in the linear resonator, we can assume same scaling and not better beam propagation factors with average input power as the CH#1, presented in Sec. 5.1.6. The idler beam quality was measured for the linear resonator and at lower powers for the RISTRA. Since there were no differences with respect to the signal beam, such measurements were not performed for the FIRE, assuming same M^2 values as the signal beam.

A direct comparison between linear and RISTRA cavity has already been done at low repetition rate [74, 73], resulting in an improvement of the beam quality of the non-resonant idler beam for the RISTRA cavity. However, in the low power limit this improvement was marginal. Here, such comparison is extended to high repetition rate regime and done mostly considering the res-

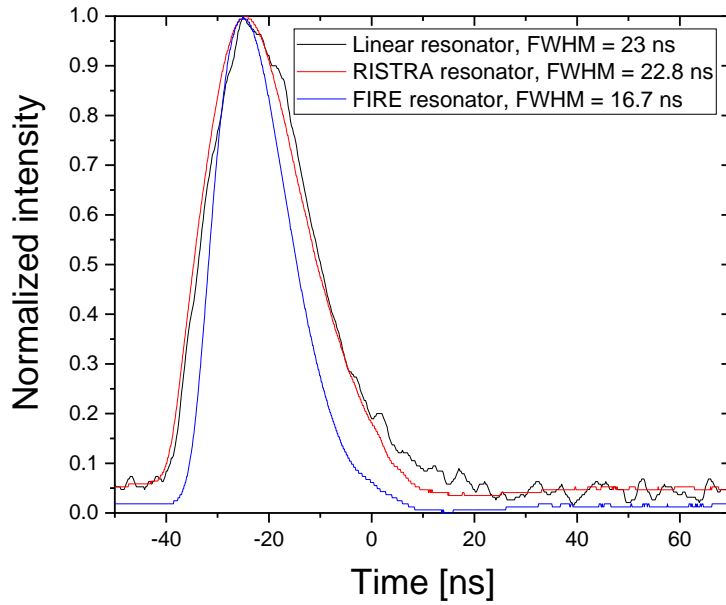


Figure 5.25: OPO output temporal pulses at maximum power for the three resonators.

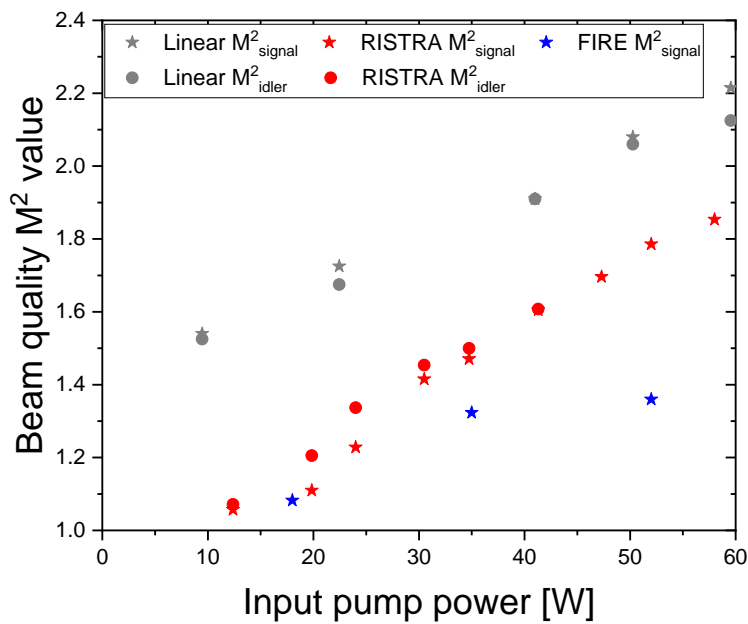


Figure 5.26: Variation of the signal and idler beam quality M^2 factor with input pump power for the three resonators.

onant signal beam. Moreover, we include also the FIRE cavity, never tested at high average power. The results on the beam qualities show a significant improvement on the M^2 value due to the non-planar geometry. This can be clearly

seen if we compare the beam quality of the output beams above threshold for the three cavities. Close to the threshold the thermal effects are negligible, thus the beam quality mostly depends on the geometry of the resonant cavity. This leads to a nearly diffraction-limited M^2 factor for both RISTRA and FIRE, despite their different threshold and build-up time. On the contrary, the linear resonator presents an M^2 factor of around 1.5. Although they operate in different resonant regimes, since the RISTRA and linear cavity have comparable round trip lengths, this result gives further insights that image-rotating configuration helps suppressing higher order modes and enhances the beam quality of the OPO output beams. At higher powers levels, with the arise of thermal effects inside the ZGP, there is a deterioration of the beam quality of the output beams. Regardless of the different total output power of each cavity (with the linear resonator giving the highest output), if the pump power is similar, so are the thermal effects inside the ZGP (considering negligible absorption for signal and idler). Thus, in similar conditions (see Fig. 5.26), the beam quality factor M^2 of the output beams improves from an initial value of 2.1 in the linear cavity ($P_{in} \approx 50$ W) to a value of 1.4 in the case of the FIRE ($P_{in} \approx 53$ W). The additional improvement of the FIRE with respect to the RISTRA cavity (1.4 vs 1.8) confirms preliminary conclusions of previous works, which stated that the fractional image rotation provides a better mode suppression at low repetition rates than the 90° rotation [59].

In Tab. 5.1 the main results of the three cavities are summarized.

OPO resonator type	P_{max}^{in} [W]	P_{th}^{in} [W]	P_{max}^{OPO} [W]	Slope efficiency [%]	Opt-to-opt efficiency [%]	M_{signal}^2 (at P_{max}^{in})
Linear (CH#1)	66	6.2	38	62	57	2.2
Linear (CH#2)	60	6	28 (extrapolated)	52	47	2.2
RISTRA (CH#2)	58	10.7	25	52	43	1.8
FIRE (CH#2)	52	12	21	50	40	1.4

Table 5.1.: Resume of the performances of the three resonators studied in this thesis.

The results of the linear resonator using the crystal CH#2 were extrapolated from the linear fit done.

As conclusion, the slope efficiency is not affected by the type of the resonator used. Therefore the P_{max}^{OPO} is mostly dependent on the oscillation threshold power. This latter is lowest for the linear resonator, hence it yields the highest output power. On the other hand, the non-planar cavities have better output beam quality, at comparable input powers, consequence of the image-rotating technique. The FIRE in particular has proven to improve the M^2 factor significantly. So, it would be beneficial to power up-scale such resonators, keeping their beam quality as low as possible. In the next chapter we will therefore fo-

cus on investigate possible improvements of the RISTRA and FIRE, considering both the output power and the output beam quality.

6. Investigations on non-planar ring cavities

This chapter is dedicated to the second part of the experimental results, in which we aim at improving the performances of the non-planar ring cavities RISTRA and FIRE. The first part of the chapter deals with power up-scaling using the same pump source as before. We tested two methods for it. The first attempt was to modify the Ho^{3+} :LLF pump spot size, decreasing its diameter from 1 mm to 0.7 mm in order to increase the peak fluence in the crystal. The performances of RISTRA and FIRE cavities were studied with the smaller spot size. As a result, we obtained a power increase, but we reached the laser damage threshold of the optics involved so no complete characterization could be done. Then, a second method for power up-scaling was to design a novel non-planar cavity. This resonator, named mini-FIRE, was based on the FIRE design and had reduced optical round-trip length. Its performances were studied and compared with the ones of the previous FIRE design.

The second part of the chapter is dedicated to the factors influencing the beam quality of the output beams in the RISTRA and FIRE. The main effects causing the deterioration of the M^2 factor are the thermal effects inside the ZGP. Hence, we firstly focused on the influence of the water cooling on the beam propagation factors. We studied both the RISTRA and FIRE, which have no crystal cooling, and compared them with the mini-FIRE (cooled and not cooled). Then, we focused on the dependence of the M^2 factor on the pump repetition rate. Using the Pockels cell, we studied the beam quality of the signal beam at a constant pump pulse energy for different frequencies. As a result, we found that there is a combining effect of the thermal lens and gain guiding and an optimal operation condition can be found. These findings are supported by simulations done by OPODESIGN.

Finally, conclusions are drawn.

6.1. Power scaling

6.1.1. Motivation

In Chap. 5 we have studied the performances of the non-planar ring cavities RISTRA and FIRE. As a result, we found that their particular geometry can

greatly improve the beam quality of the signal and idler output beams with respect to the linear resonator. However, their oscillation threshold is higher, leading to a lower maximum output power achievable. It is therefore interesting to find methods for up-scaling the power of such non-planar resonators, keeping at the same time a good beam quality.

Since oscillation threshold and conversion efficiency are dependent on the peak fluence inside the crystal, one approach would be to decrease the pump spot size. Previously we set the pump diameter to $D = 1 \text{ mm}$, assuring a maximum peak fluence $< 2 \text{ J/cm}^2$ in the ZGP crystal. However, the reported damage threshold for ZGP with AR coatings exceeds 4 J/cm^2 [21]. Hence, even though we don't have specific laser damage data for our crystals, we can reasonably still decrease the pump spot size and not exceed their damage thresholds. Therefore, we studied the performances of RISTRA and FIRE with a smaller pump spot diameter.

Another way to reduce the oscillation threshold of the non-planar cavities would be to decrease their optical round-trip length to assure shorter build-up time. This is true especially considering the FIRE, which has the longest cavity length. Thus, it is interesting to design and build a miniaturized version of such resonator. This new adaptation, named mini-FIRE, is then implemented in our setup and fully characterized, comparing its performances to the FIRE ones.

6.1.2. Different pump diameter

In Chap. 4, we set the pump beam diameter to $D = 1 \text{ mm}$, having a maximum peak fluence of 1.75 J/cm^2 (Sec. 4.1.2). In order to power up-scale the RISTRA and FIRE performances, we reduced it to a value of $D = 0.7 \text{ mm}$. This means that at the maximum input power (68.7 W), the fluence in the crystal is 3.6 J/cm^2 , lower than reported laser damage thresholds for ZGP [21]. With this new pump spot size, we tested the two cavities as we did in Sec. 5.2. Previously, in Chap. 5, we used the ZGP CH#2, since the best performing CH#1 crystal presented a surface damage. In this section, we use again the CH#1 (after re-coating). The comparison of the performances of the two crystals is presented in Fig. 6.1. The graphs show the total OPO output power obtained in a linear resonator using a beam diameter of 1 mm, as presented in Sec. 5.1.5. In particular, we can note that the two crystals have similar oscillation threshold. In Fig. 6.2 the output power as a function of the input pump power with the small pump spot size is presented for RISTRA and FIRE (CH#1). Their results are compared with the previous ones obtained with the bigger pump diameter (CH#2). We can immediately notice a lowering of the oscillation threshold in the new setup. Indeed, in the RISTRA we see that the threshold power shifts from a value of 10.7 W for a 1 mm spot size to 5.3 W in the case of $D = 0.7 \text{ mm}$. For the FIRE cavity the power threshold values are 12 W and 8.6 W, respectively. The slope efficiencies are also quite different from the previous measured val-

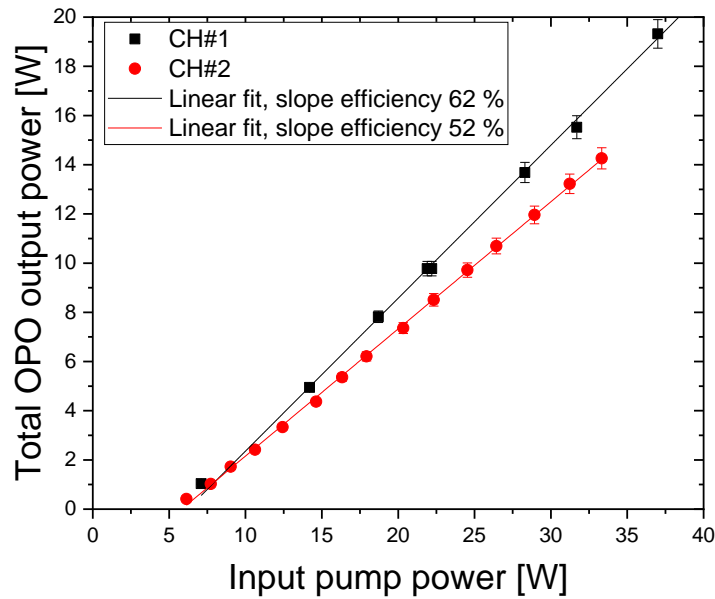


Figure 6.1: Total output power as a function of the input power in a linear resonator for the CH#1 and CH#2 crystals.

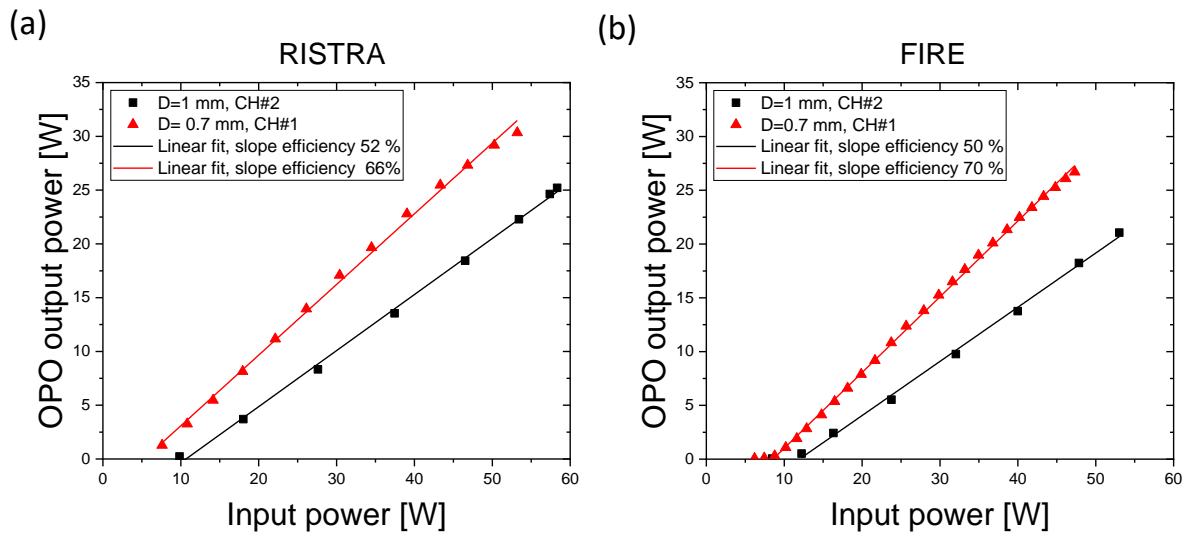


Figure 6.2: Total output power as a function of the input power for two values of pump beam diameter. (a) RISTRA. (b) FIRE.

ues, increasing to 66 % and 70 % for RISTRA and FIRE, respectively. The higher slope efficiencies can be partially explained because of the different ZGP used (see Fig. 6.1). However, for the linear cavity crystal CH#1 was giving a slope efficiency of 62 %. Therefore, the beam diameter affects the slope efficiency. Concerning the maximum output power achievable with the smaller pump di-

ameter, in RISTRA we obtained 30.3 ± 0.9 W for an input power of 53.2 W, corresponding to an optical-to-optical efficiency of 57 %. In the FIRE, for an input pump power of 47.3 W, we achieved 26.7 ± 0.8 W of total output power (opt-to-opt efficiency of 56 %). These values are however not obtained with the maximum input power available. The reason of the lower input power used lays in the main drawback of this operating OPO conditions: the laser damage threshold of the optics. Indeed, pumping with higher powers resulted in damaging either the OC mirror or the ZGP AR coating. These damages occurred multiple times and always around an input power of ≈ 50 W, corresponding to an energy peak fluence of ≈ 2.6 J/cm². In Fig. 6.3 pictures of the damages are shown.

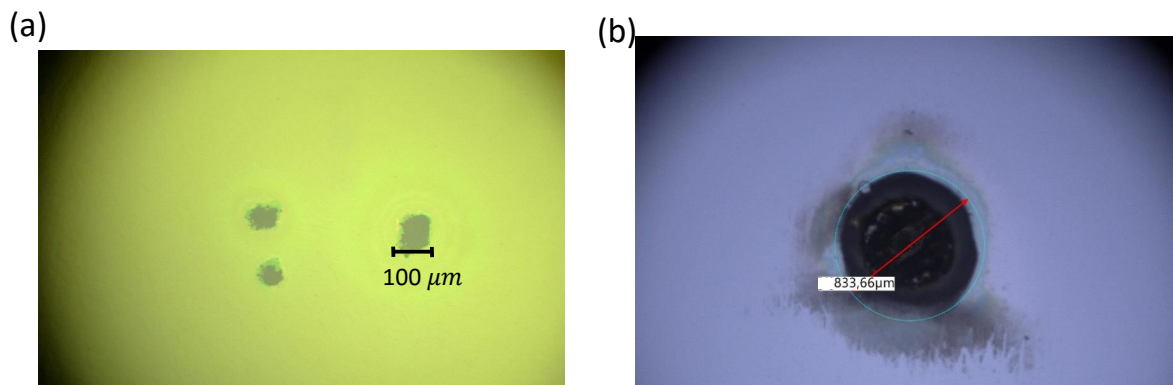


Figure 6.3: Damages induced by the pump beam diameter of 0.7 mm. (a) Picture of 3 damage spots on the OC taken with a microscope. (b) Damage picture of the ZGP coating taken through a microscope.

The first image is a picture of the OC after being damaged, where three small damages spots can be noticed. They were inspected through a microscope (VHX digital microscope, Keyence). The second image is a microscope image of a damage on the ZGP coating. Its diameter was measured to be around 800 μm, comparable with the size of the pump beam. As consequence of the damages, the beam quality measurement of the signal and idler beams could not be performed.

As a conclusion, even though the improvement in power obtained by decreasing the pump beam diameter is evident, the laser damage threshold of the optics hampers it to be a solution for further power up-scaling in our setup. In the previous chapter, the OPOs performances were pump power limited and further up-scaling could in principle be done pumping with higher pump power. The damages occurred in this section gives us insight of the technical limits of the setup. A laser damage threshold of ≈ 2.6 J/cm² would correspond in fact to a possible maximum pump power of approximately 102 W with

$D = 1 \text{ mm}$ pump diameter. Assuming no strong back-conversion problems, according to the slope efficiencies found in Chap. 5, we could achieve a maximum output power from the CH#2 of around 50 W (linear), 48 W (RISTRA), and 45 W (FIRE). To achieve the maximum output power using our existing pump source (68.7 W), we could set the pump spot diameter to $D = 840 \text{ }\mu\text{m}$, assuring a maximum fluence of 2.5 J/cm^2 .

6.1.3. Different cavity length: mini-FIRE

In Sec. 5.3 we have seen how the FIRE cavity yields the best beam quality for the OPO beams but has the lowest output power due to the high oscillation threshold. In order to decrease the latter, we designed a novel, miniaturized version of the resonator, named mini-FIRE (see Fig. 4.10 (d)). Since, as seen in Sec. 5.1.5, a 16 mm ZGP has good performances, the new resonator was thought to operate with these smaller crystals. In particular, we used the crystal BAE E1, with lower absorption with respect to the BAE E2. As mentioned previously, the RISTRA and FIRE do not have any cooling of the crystal, which affected the spectra, as seen in Sec. 5.2.2. Therefore, the mini-FIRE was conceived also to improve this aspect, implementing the possibility of water cooling of the ZGP crystal. The crystal mount, as well as the monolithic resonator, was built in an aluminum alloy to assure good thermal conductivity and heat dissipation. The cavity was fabricated by a 3-D printing technique and was then post processed to obtain the final version. As result, the cavity has a physical length of 101 mm, corresponding to an optical round-trip of 135 mm. It was operated in singly resonant mode, with the OC partially reflective at the signal wavelength ($R = 50 \%$) and highly transmissive for idler and pump beams. The pump diameter was set back to 1 mm. The total output power as a function of the input power is presented in Fig. 6.4. For a maximum input power of 60.2 W, a total output power of $23.8 \pm 0.7 \text{ W}$ was achieved, resulting in a slope efficiency of $48.6 \pm 1.6 \%$. The optical-to-optical efficiency was 40 %. From the linear fit, the oscillation threshold for OPO conversion was calculated to be 11.8 W. As the other non-planar ring cavities, the mini-FIRE did not need any misalignment for the mirrors in order to avoid back-reflection and obtain stable operation. Its stability measurement is presented in Fig. 6.5 (a). The measurement was done over a period of one hour at an intermediate power level. The OPO output power was measured at a value of $12.54 \pm 0.13 \text{ W}$, corresponding to a relative standard deviation of $C_v = 1.04 \%$. The corresponding input power was $47.1 \pm 0.2 \text{ W}$. We can notice a higher stability with respect to the previous measurements for the RISTRA and FIRE. The reason is probably due to the presence for the mini-FIRE of a thermal cooling system of the ZGP. To verify the absence of back-conversion, we recorded the OPO temporal profile at maximum output power. The average of 128 pulses was collected and it is presented in Fig. 6.5 (b). The pulse width (FWHM) was $\tau = 20.7 \text{ ns}$, corresponding to a peak power of

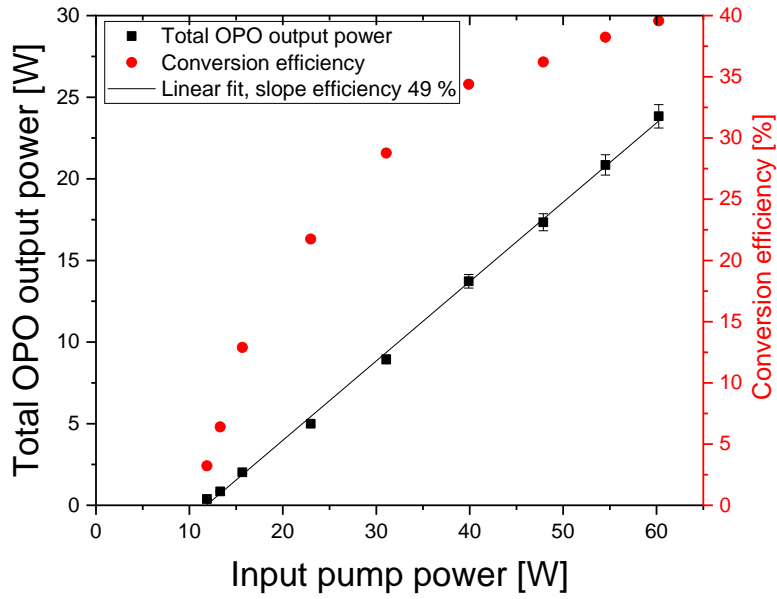


Figure 6.4: Total output power and conversion efficiency as a function of the input pump power in mini-FIRE.

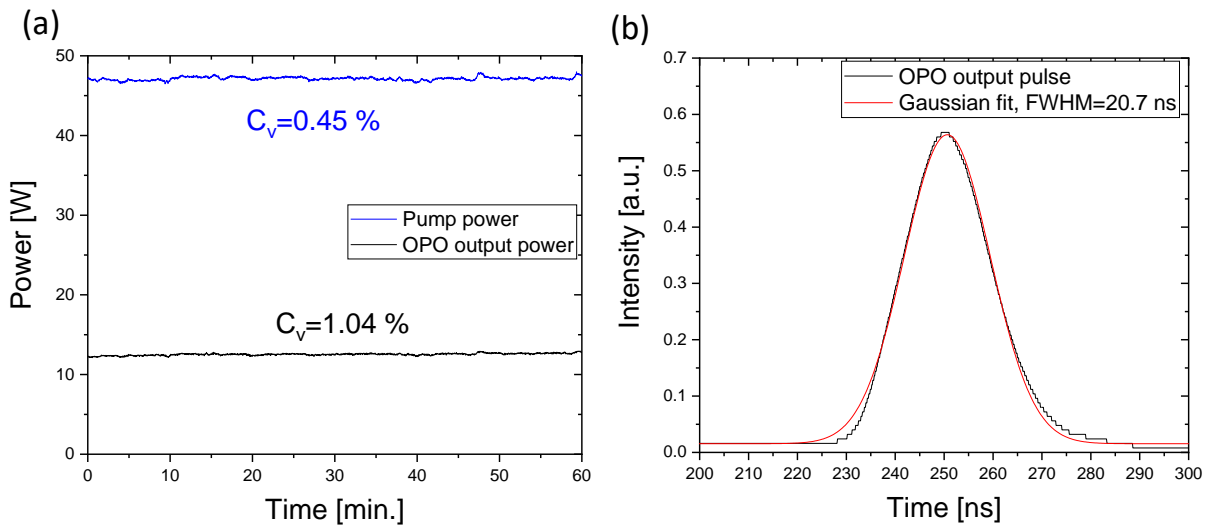


Figure 6.5: (a) OPO and pump power stability measurement over 1 hour operation time with water cooling. The labels indicate the corresponding relative standard deviation. (b) Temporal pulse profile of the OPO at the maximum output power of 23.8 W.

115 kW. Its pulse duration is higher than the pulse width of the FIRE (16.7 ns), as expected from a smaller cavity length [99].

The beam propagation factor M^2 of the signal and idler beams was measured

at different power level. Their variation is presented in Fig. 6.6 (a).

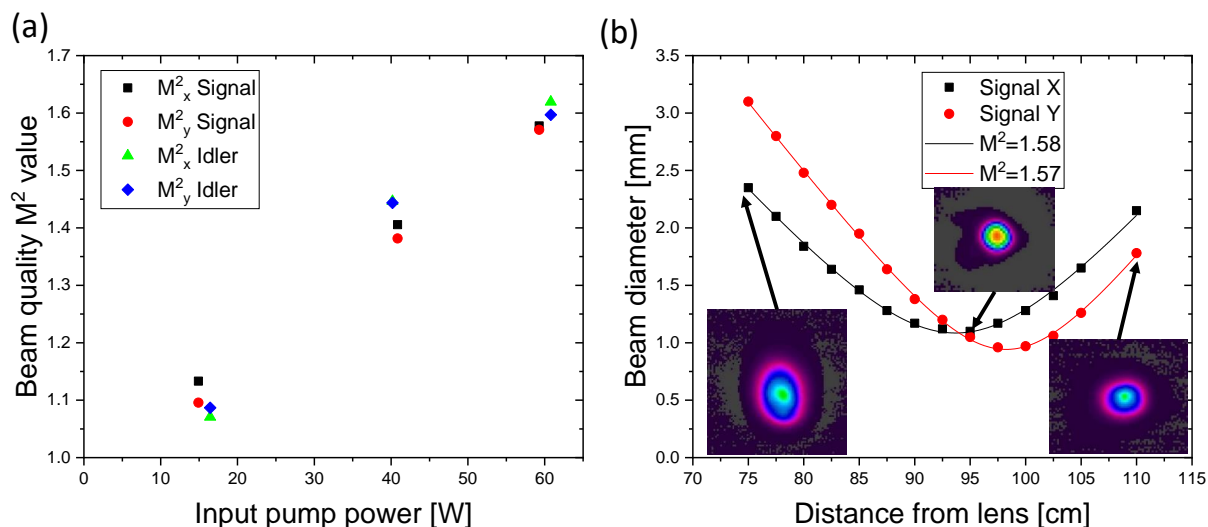


Figure 6.6: (a) Variation of the signal and idler beam quality M^2 factor with input pump power for the mini-FIRE resonator. (b) Signal M^2 value measurement at maximum input power of 60 W.

As for the other non-planar cavities, above threshold the beam quality factor is close to the diffraction limit. At an input power of 15 W ($P_{OPO} = 1.3$ W), the M^2 values of the signal beam in X and Y direction were 1.13 and 1.09, respectively. In the case of the idler, they were $M^2_x = 1.07$ and $M^2_y = 1.09$ at the input pump power of 16.4 W ($P_{OPO} = 2$ W). The beam quality then deteriorates as usual due to the thermal effects inside the crystal, reaching an M^2 factor of around 1.6 for both beams at the maximum power. In Fig. 6.6 (b) such measurement for the signal beam is presented. We can notice some ellipticity of the beam.

Although these performances of the mini-FIRE appear encouraging, we have to compare them with the FIRE ones (Sec. 5.2.3). The two cavities were tested using ZGPs of different lengths and absorption coefficient. So, in order to have a proper comparison, we used the software OPODESIGN to simulate the performances of the two cavities under the same conditions. As mentioned in Sec. 4.2.2, this software has the possibility to add into the calculation a thermal lens effect. At first, the simulations were done by considering a fixed thermal lens with focal length of 10 m. We simulated the FIRE and mini-FIRE performances with $D = 1$ mm and a crystal length of 16 mm. In Fig. 6.7 the output power as a function of the input pump power obtained from the modeling is presented. From the slope efficiency, we can immediately notice the exaggerated back-conversion predicted by OPODESIGN, which affects the curve at high input powers (> 30 W). However, the oscillation thresholds are trustful and in particular for the mini-FIRE, close to 11 W, is conform to the experimental data. We may therefore conclude that, using the same 16 mm crystal, the

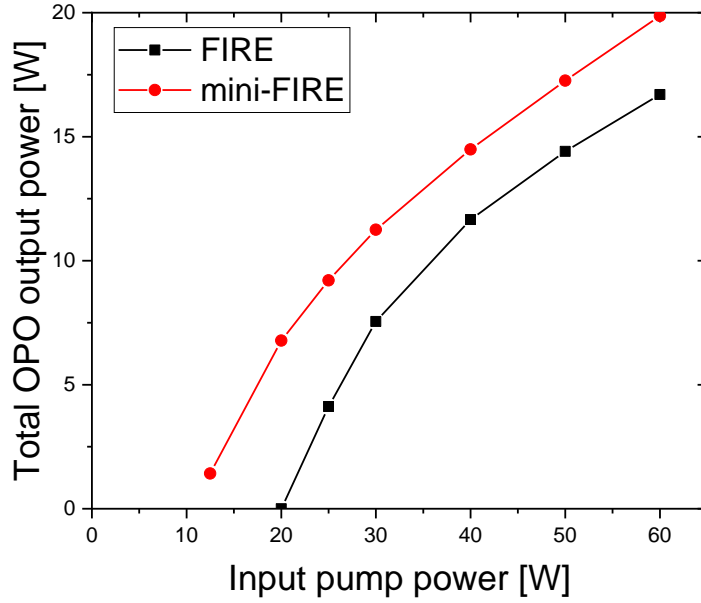


Figure 6.7: Simulated total OPO power as function of the input power for the mini-FIRE and FIRE with a 16 mm ZGP. A fixed thermal lens with $f = 10\text{ m}$ has been considered.

mini-FIRE has a lower oscillation threshold with respect to the FIRE by approximately 10 W, corresponding to 50 % of its value.

A more accurate simulation can be obtained if we consider the variation of the thermal lens, as described in [79]. As discussed in Chap. 3, we can estimate the focal length in our conditions using Eq. 3.37. However, even though the above formula can give an idea of its strength, the thermal lens is often not known in real experiments and can differ much from the theoretical one. If we consider a pump diameter of 1 mm, an input power of 30 W and a crystal absorption of 8 % (as BAE E1), we obtain for our experimental conditions a focal length $f \approx 157\text{ mm}$. This value however, appeared to be too small to properly simulate our experimental data. We therefore decided to change its value in order to match our experimental data. Thus, we assigned a focal length of $f = 1000\text{ mm}$ at an input pump power of 30 W. The focal length f was then scaled as $1/P_{in}$, as according to Eq. 3.37. In Fig. 6.8 the comparison between such simulation and the experimental results is presented for both resonators. Since the BAE E1 and CH#2 have similar absorption (see Tab. 4.1), between the mini-FIRE and FIRE simulations only the crystal length was changed. All the other parameters were kept unchanged. In the case of the mini-FIRE, the two curves have good agreement, even though some back-conversion can still be notice from the shape of the simulated slope. This effect is due to the large widths of the OPO spectra, which are neglected by the OPODESIGN code, based on single frequency op-

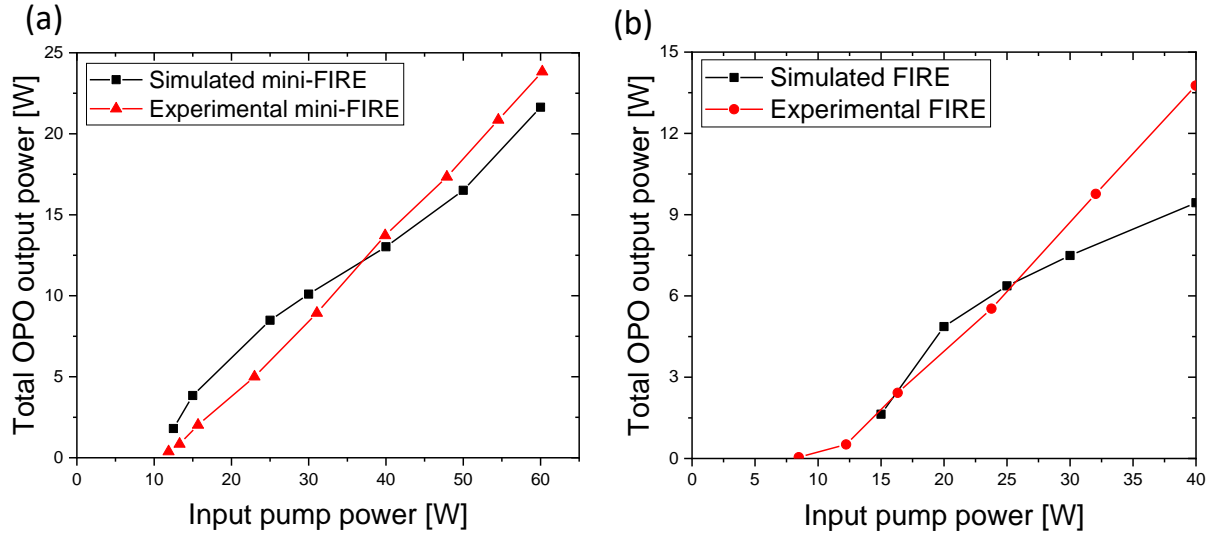


Figure 6.8: Experimental and simulated total OPO output power as function of the input pump power. A varying thermal focal lens has been considered. (a) Mini-FIRE with 16 mm long ZGP. (b) FIRE with 20 mm long ZGP.

eration. The simulations of the FIRE of Fig. 6.8 (b) are even more affected by this effect, given by the longer crystal length used during the experiments. As consequence, the simulation was not run above 40 W, since there was already discrepancy with experimental data at that power level.

In order to compare properly the FIRE and mini-FIRE, we have additionally to model the output beam qualities of the two resonators. The results of the simulation of the signal M^2 factor for the mini-FIRE, together with the experimental data, are presented in Fig. 6.9. At low input powers the simulations are in good agreement with the experiments, finding a beam quality close to the diffraction limit. Above 40 W however, it is clear how the exaggerated back-conversion of OPODESIGN hampers trustful M^2 modeling. In the FIRE, this effect would be even more evident. This limitation of the code constraints us to be able to compare properly the two resonators at high powers. The improvement of the M^2 value for the FIRE (≈ 1.4) with respect to the mini-FIRE (≈ 1.6) is probably due to the longer cavity length. Further studies are however needed in order to confirm it.

The performances of the mini-FIRE have to be also compared with the other cavities studied in Chap. 5. As seen in Sec. 5.1.5, the crystal used in the mini-FIRE (BAE E1) was tested in the linear resonator. Despite the longer optical length, it had a lower oscillation threshold, around 5 W (11.8 W for mini-FIRE), and a higher slope efficiency (55 % vs 49 %). This is principally due to the different operational regime (doubly vs singly resonant) [64, 92]. The mini-FIRE however greatly improves the beam quality of the output beams from an M^2

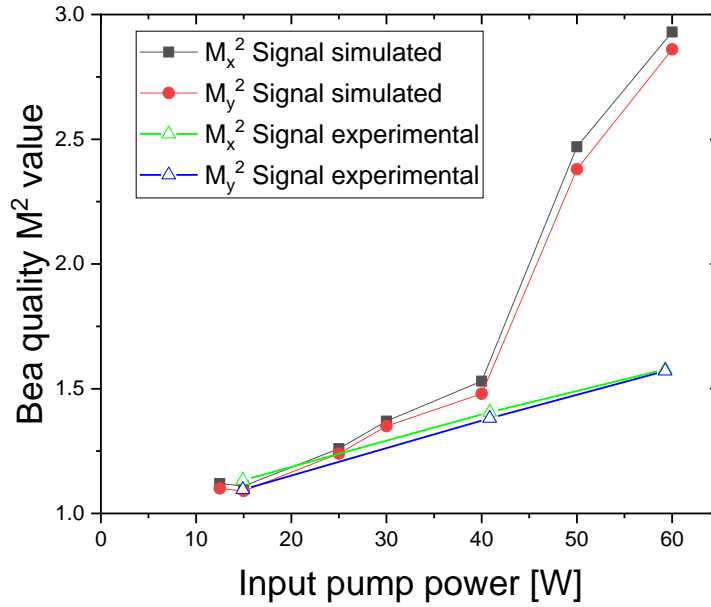


Figure 6.9: Experimental and simulated variation of the signal beam quality M^2 factor with input pump power for the mini-FIRE.

factor of 2.2 to 1.6 at the same input power. This latter result is an improvement with respect also to the RISTRA cavity. Indeed, despite the longer cavity length, in RISTRA the beam quality factor at maximum power was $M^2 = 1.8$, higher than the mini-FIRE.

To conclude, a novel miniaturized FIRE resonator was designed, built and tested. From comparison between experiments and simulations with OPODESIGN, it can be stated that the mini-FIRE lowers the oscillation threshold by a value of approximately 10 W when using a 16 mm ZGP. This value is around half of the threshold power of the FIRE. The beam quality M^2 factors of the output beams however are slightly worse than the FIRE (1.6 vs 1.4). Nevertheless, the mini-FIRE yields a better beam quality of the output beams with respect to the other two resonators studied in this thesis: the linear and RISTRA cavities. Finally, the presence of the water cooling improves the mini-FIRE power stability with respect to the other non-planar ring cavities. Its effect on the beam quality will be investigated in the next section.

6.2. Thermal management for improved beam quality

6.2.1. Motivation

As seen in the previous sections, the thermal effects inside the crystal deteriorate the output beam quality. It is therefore interesting to investigate methods to influence thermal effects in order to be able to improve the M^2 factors.

The first aspect to be considered is the thermal load in the ZGP. As mentioned in Sec. 4.1.4, the RISTRA and FIRE do not have a water cooling system, causing a drift of the wavelength, as seen in Sec. 5.2.2. The increase of the temperature in the crystal however could in principle affect the beam propagation factors. Since the thermal load out of equilibrium is proportional to the operating time and input power, we investigated this effect by monitoring the evolution of the M^2 factor as a function of time. The measurements were carried out for the three non-planar cavities studied in this thesis. The mini-FIRE in particular, highlighted the influence of water cooling of the crystal.

As mentioned in Chap. 3, in the deterioration of the M^2 with the power, two main effects are to be accounted for. These are the thermal lensing [100] and gain guiding [82, 81]. The latter depends only on the pump pulse energy but not on the average power of the pump. On one hand, this effect can be minimized by increasing the pump spot size in the crystal, but on the other hand, the greater the pump spot size is, the higher is the threshold and more difficult to maintain good beam quality [81]. The thermal lens instead depends on the heat absorbed by the crystal, thus it is proportional to the pump repetition rate for a given pulse energy. Hence, investigating the evolution of the M^2 factor with the pump pulse frequency at a constant pump pulse energy would allow to isolate the contribution of the thermal lens from the gain guiding effect. Such measurements were therefore done for the RISTRA and FIRE resonators.

6.2.2. Influence of water cooling

In Chap. 5 we have mentioned how the RISTRA and FIRE cavities are not cooled during their operation. This affected their stability and output wavelengths, as seen in the previous sections. To understand the influence of the absence of cooling on the beam quality, we monitored the M^2 as a function of time. The procedure to reconstruct the beam quality as a time function is as follows. After opening the pump with a mechanical shutter, the beam profiles at a certain position of the camera are captured with a 20 ms resolution. Then, the camera is moved to the next position along the signal beam, while the crystal is allowed to cool down and come back to the initial equilibrium conditions. The intervals required for this were determined experimentally to be around 5 min-

utes. After data is collected for enough points, we retrieve the time evolution of the beam quality factor in post-processing by combining the profiles for the same time frame. All the measurements were done at maximum power level, so to accentuate the effect.

The result of such procedure for the RISTRA and FIRE is presented in Fig. 6.10. After the pump was unblocked, the measurements were taken over a period of

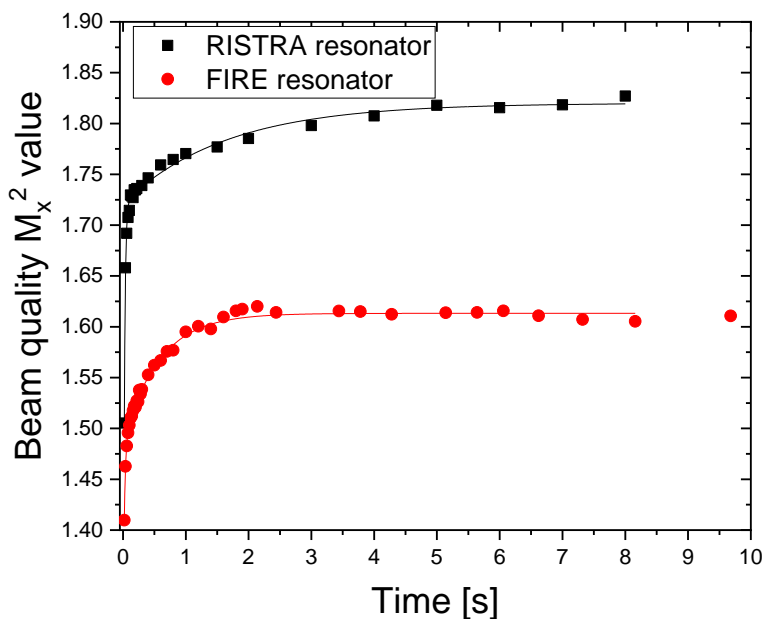


Figure 6.10: The evolution at maximum power of the beam quality M^2 factor for the RISTRA and FIRE with 20 ms time resolution (not all the points are plotted).

10 seconds. The M_x^2 of the signal beam is presented in the graph. Not all the collected data points are plotted for visual reasons. We can notice that the M^2 values after some seconds are comparable with the ones measured in Sec. 5.2. In the dependence of the M^2 we can notice that there are two timescales of the process. The first, fast exponential behavior (showed as a fit to the data) is related to the build-up of the thermal lens to its steady-state value [80, 79]. After it, we observe a deterioration of the M^2 factor, which can be likely attributed to heat accumulation and a rise in the overall temperature of the crystal and its holder. The heat accumulation leads to a slow change of the boundary conditions for a temperature profile inside the crystal, thus a change in the shape of the thermal lens. As a consequence, a slow deterioration in the M^2 value is observed. This appears to be evident in the RISTRA resonator, while the propagation factors of the FIRE seems to remain constant. This is probably due to their different mounts. Both of them are built by a monolithic piece of steel. The FIRE however has an increased size compared to RISTRA, hence a greater heat

capacitance. This results in a longer time scale for the slow M^2 deterioration. This slow drift depends only on the water cooling of the crystal holder, absent in our setup. The presence of a water cooling system would assure constant boundary conditions for the transient thermal lens. Therefore, it is interesting to investigate this behavior in the presence of cooling. Thus, we repeated the measurements for the mini-FIRE resonator. In this cavity the cooling could be turned off and on as wanted. The measurements were done in both cases for comparison. Common city tap water was used for the scope, with a temperature of around 20°C . The water flow on the crystal mount when cooled is 0.35 L/minute . In Fig. 6.11 (a) the result of such study is presented.

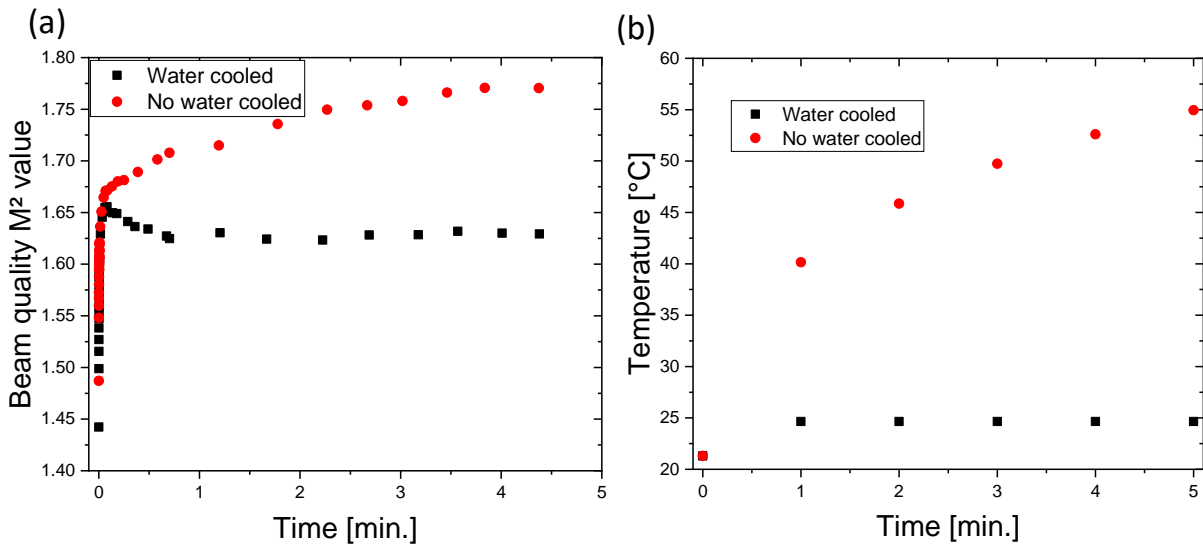


Figure 6.11: (a) The evolution of the beam quality M^2 factor for the mini-FIRE in the presence and absence of water cooling for the ZGP mount. (b) Evolution of the temperature of the external wall of the crystal mount in presence and absence of water cooling.

The beam profiles were recorded over 5 minutes. The first exponential growth is unchanged by the presence of water cooling, as expected. The effect of the water cooling is evident when considering the slow M^2 drift. In the case of no water cooling a deterioration of the beam quality is observed, similar to the previous measurements. The effect is even more evident in this case due to the physical size of the mini-FIRE, that results in less passive heat dissipation. On the opposite, with a cooling system we can notice how after a period of approximately 1 minute, it reaches a steady state where the M^2 factor stabilizes to a value of around 1.63, similar to the result obtained in Sec. 6.1.3. The "hump" shape that appears during the first minute of operation is probably due to an initial power spike. The same kind of stabilization can be seen if we consider the temperature close to the ZGP. Even though it can't be measured, we can

have an indication of its evolution by measuring the temperature of its mount. Hence, we glued a temperature sensor (RTD Pt100) externally on the crystal mount and we assessed its temperature during OPO operation. In Fig. 6.11 (b) the results are shown. We can notice that, while in the presence of water cooling the temperature is stable to a value of $24.7\text{ }^{\circ}\text{C}$, in the absence of water cooling it slowly increases. After 5 minutes, it reaches a value of $T = 55\text{ }^{\circ}\text{C}$. The temporal response of the thermal resistor (of the order of seconds) was not fast enough to investigate properly the behavior during the first fast M^2 deterioration.

To conclude, the time-resolved beam quality studies in this section revealed the steady-state thermal lens build-up. This feature is usually masked in other high power experiments, where beam quality measurements show only the system performance at stationary conditions in equilibrium. The water cooling has a significant effect on the beam qualities. Passive water cooling results in more stable output beam propagation factors. The knowledge of this dynamic behavior could be useful when designing and optimizing the duty cycle for a particular application, e.g. the ability to focus the laser output over long distances can be enhanced by appropriate timing control. Another possibility would be to apply to the OPO an active cooling system, which could even further improve the beam quality control.

6.2.3. Pulse repetition rate dependence

As mentioned previously in Chap. 3, two main effects contribute to the deterioration of the beam quality: the thermal lens [100] and the gain guiding [82, 81]. The first depends on the power absorbed by the crystal, while the second depends on the pump pulse energy, i.e. gain distribution. During the measurements of Chap. 5 we studied the deterioration of the M^2 factor as a function of the input pump power. This however does not allow us to discriminate between the two effects, since both the pulse energy and the input power are varied.

In this section we focus on separating the contribution of gain guiding and thermal lens. In order to do it, we investigated the dependence of the beam quality on the pump repetition rate in the non-planar ring cavities. Using a Pockels cell (see Fig. 4.6), the pump pulse frequency is controlled by pulse picking without affecting the pulse properties. We set the frequencies to: 0.1 kHz, 0.5 kHz, 1 kHz, 2.5 kHz, 5 kHz and 10 kHz. The pump pulse energy was kept at the constant value of 6 mJ for the RISTRA. Due to the lower transmission of the IC, for the FIRE it was set to 5.3 mJ. No other pulse property was modified. The measured beam quality M^2 factor as a function of the pump repetition rate is presented in Fig. 6.12 for the two cavities.

This study could not be performed in the linear resonator: the back reflection of the IC was heating the Pockels cell, affecting the polarization of the pump beam. Only the M^2 of the signal beam, averaged between X and Y direction, is

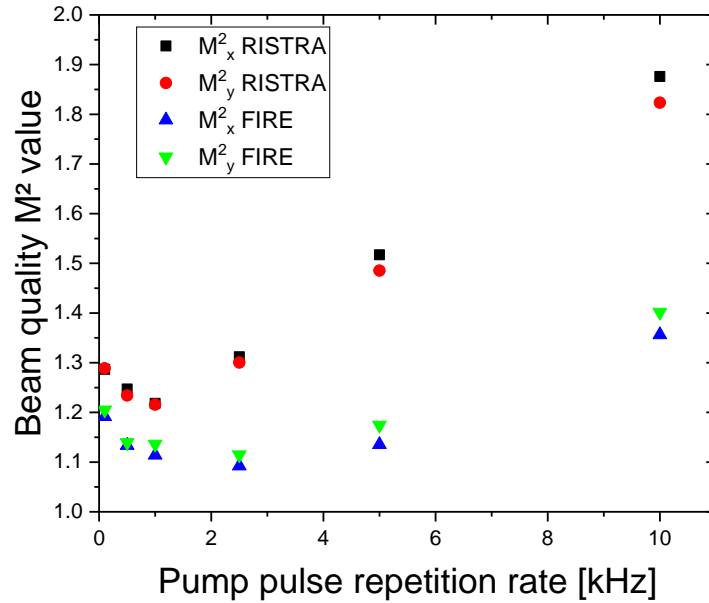


Figure 6.12: Experimental evolution of the M^2 value with pump pulse repetition rate at a constant input pulse energy of: 6 mJ for RISTRA, 5.3 mJ for FIRE.

depicted in the graph. Intuitively, lowering the repetition rate, one might expect an improvement of the beam quality as the one found when the average power is lowered in Chap. 5. However, the measured beam quality value shows a minimum at different frequencies for the two cavities. For the RISTRA, starting from an initial value of 1.3 at 0.1 kHz, the M^2 drops to a minimum value of 1.2 at 1 kHz, then increases for higher repetition rates reaching the final value of 1.8 at 10 kHz. In the FIRE cavity, the initial M^2 value at 0.1 kHz is 1.2, it drops to a minimum of 1.1 at 2.5 kHz and then increases to 1.4 at 10 kHz. At low repetition rate, the thermal lens is weak and the beam quality is dominantly governed by the gain guiding effect at the pump pulse energy of 6 mJ. The two effects cause a narrowing of the resonant signal beam, which results in a stabilization of the resonant cavity, despite the use of flat mirrors. Moreover, the gain guiding effect in the absence of thermal lens (low repetition rate) at 6 mJ pump pulse is not enough to obtain a perfect overlap between the pump beam waist and the cavity mode size. As the repetition rate, hence thermal lens, slightly grows, this effect becomes more and more accentuated and improves the spatial overlap with the fundamental cavity mode, improving the beam quality. A further rise of the repetition rate makes the thermal lens even stronger, causing a growing destabilizing effect on the OPO cavity.

In order to confirm this behavior, we did numerical simulations with the OPODESIGN software. As seen in Sec. 6.1.3, the software can not model prop-

erly the beam quality at such pump energies due to back-conversion. Hence, in order to minimize this bad conversion effect, we reduced the crystal length to 12 mm. We considered again a thermal lens varying with the pump power accordingly to Eq. 3.37. The gain guiding was kept constant by simulating only at a fixed value of input pulse energy. The result of the simulation for the RISTRA are presented in Fig. 6.13, together with the experimental results. The numerical

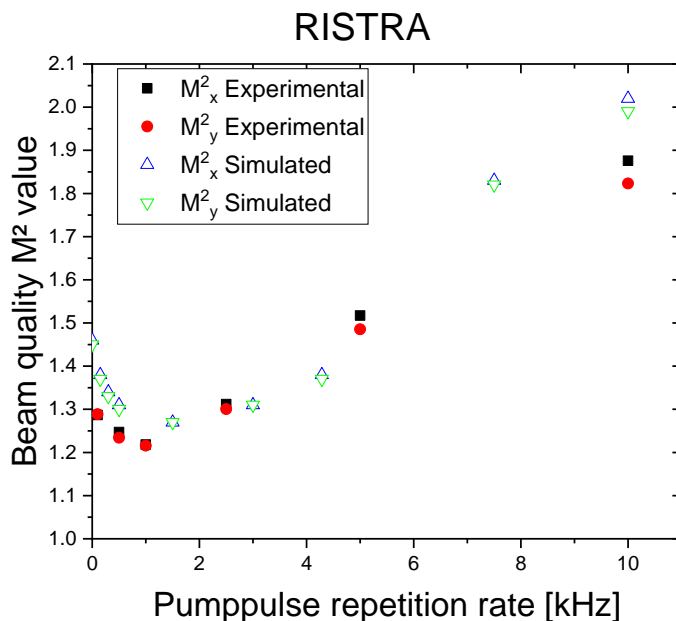


Figure 6.13: Simulated and experimental evolution of the beam quality M^2 factor with the pump pulse frequency at the constant pulse energy of 6 mJ for the RISTRA. Simulation done with OPODESIGN.

simulations confirm the experimental data.

Previous reports on the dependence on the pump pulse frequency in OPO systems were limited to monitoring the conversion efficiency at low repetition rates for the RISTRA resonator [62]. Moreover, they tuned the Q-switching frequency of the pump laser, thus varying the pump pulse duration simultaneously with the repetition frequency. In this section we focused on the dependency of the beam quality on the pump repetition rate. We found that an optimal condition given by the thermal lensing and the gain guiding exists, which delivers the best beam quality. The different positions of the M^2 minimum between the RISTRA and FIRE experimental data is related to the different cavity length, hence different fundamental mode size. The slightly different pump pulse energy used in the two resonators contribute to explain the difference. Additionally, these measurements supports the improvement of the beam quality in the FIRE compared with the RISTRA. Indeed, at all repetition rates, the FIRE resonator presented a better M^2 factor.

6.3. Conclusions

In this chapter, we investigated methods to improve the performances of the non-planar ring cavities RISTRA and FIRE, studied in Chap. 5.

First, we focused on increasing the output power in the mid-IR region. Being limited by the pump source, we reduced the pump spot diameter from an initial value of 1 mm to a value of 0.7 mm. This allowed us to obtain 30 W of total OPO output power in the RISTRA and 27 W in the FIRE. However, in doing so we reached the laser damage threshold of the optics involved in our experiments, which hampered the beam quality measurements. As second method to power up-scale the system, we designed and built a miniaturized version of the FIRE resonator and we characterized its performances. We used a smaller, 16 mm long crystal inside this cavity, obtaining 24 W of output power with an $M^2 = 1.6$. A comparison with the previous FIRE design has been done with the use of simulation. This results proves that similar performances as the one with the FIRE cavity can be achieved by the use of a much more compact resonator.

In the second part of the chapter, we focused on the study of the thermal effects which deteriorates the beam propagation factors at high powers. To achieve this, two studies were done. The first one was on the influence of the water cooling on the degradation over time of the M^2 factor. This effect was studied in the RISTRA, FIRE and mini-FIRE cavities, highlighting the significant difference between the cases where the water cooling is present and the ones when it is not. The second influence on the M^2 studied was on the pump repetition rate. Such study allowed us to discriminate between the contribution of the thermal lens and gain guiding effect. As a result, we revealed an optimal condition to have a good beam quality.

7. Conclusions and outlook

7.1. Conclusions

In this thesis, we demonstrated a compact OPO system delivering high average power in the mid-IR region with good beam quality. This result was achieved by implementing a nonlinear crystal of ZGP in different OPO resonators.

Although high power, high repetition rate OPOs have been demonstrated in the past using different cavity geometries, there have been no exhaustive studies comparing them. Using a 10 kHz, diffraction limited, Ho^{3+} :LLF MOPA system as a pump source, we tested different OPO resonators and compared their performances in similar conditions. A maximum output power of 38 W in the mid-IR (66 W of input power) was obtained in a doubly-resonant, 46 mm long linear cavity. The beam quality factor at maximum output power was $M^2 = 2.2$. Two kind of non-planar ring cavities were then implemented, proving to be capable of significantly improve the beam propagation factors: $M^2 = 1.8$ in the RISTRA, and $M^2 = 1.4$ in the FIRE. Their conversion efficiencies were comparable with the linear resonator, but the output power obtained was lower due to their higher oscillation threshold. We obtained 25 W of output power in the RISTRA and 21 W in the FIRE. This is the first demonstration of such cavities at high repetition rate and high average power regime.

From these first demonstrations of beam quality improvement, in the FIRE and RISTRA cavities, we carried out studies to further increase their performances. Being limited by the pump source output power, the first approach to increase the OPO output power was to lower its oscillation threshold. We therefore increased the pump peak fluence in the ZGP by reducing its beam diameter from 1 mm to 0.7 mm. This allowed us to achieve 30 W of total output power in the RISTRA and 27 W in the FIRE. However, we reached the laser damage threshold of the optics. Hence, we explored another method to power up-scale the system. We designed, built and tested a miniaturized version of the FIRE cavity (mini-FIRE), with a smaller cavity round-trip length (222 mm vs 101 mm of physical length). A water cooling system for the nonlinear crystal was also added to the resonator. In this setup, using a 16 mm long ZGP, we obtained 24 W ($M^2 = 1.6$) in the mid-IR. Using the software OPODESIGN, this results were compared to the FIRE ones, proving that the mini-FIRE reduces the threshold power by approximately 50 % when using a 16 mm ZGP. The power

obtained in the two cavities were comparable due to the use of a shorter crystal in the mini-FIRE.

In addition to these studies, we investigated the factors that contribute to deteriorate the OPO beam quality. First, we studied the dependence of the beam propagation factor on the water cooling of the ZGP. This was done by doing time-resolved studies on the M^2 factors at full power for the RISTRA, FIRE and mini-FIRE. The mini-FIRE in particular was investigated in the presence and in the absence of water cooling, finding that a cooling system is crucial to deliver a beam with stable and reduced M^2 . This study, conducted with a 20 ms time resolution, unraveled the dynamic behavior of the thermal lens before reaching equilibrium. In applications where the beam quality is critical, this result could be useful when considering the duty cycle of such systems. As a second study, we investigated the two factors that concur on the M^2 deterioration. The contributions of the thermal lensing and gain guiding effect on the beam quality were separated. This was done by inspecting the dependence of the M^2 factor on the pump repetition rate at a constant pump pulse energy. As a result, we revealed conditions for optimal beam quality. The findings were supported by numerical simulations.

As a final resume, in Tab. 7.1 the main results obtained in this thesis are listed and compared with previous results obtained in the literature (see Chap. 2).

Author	Year	P_{max} [W]	M^2	$P_{max}/(M^2)^2$	Reference
Liu et al.	2021	161	3.6	12.4	[48]
Lippert et al.	2010	22	1.4	11.2	[56]
This thesis, FIRE	2021	21	1.4	10.7	Chap. 5
This thesis, mini-FIRE	2021	24	1.6	9.4	Chap. 6
This thesis, linear	2021	38	2.2	7.9	Chap. 5
This thesis, RISTRA	2021	25	1.8	7.7	Chap. 5
Yao et al.	2014	41	4.4	2.1	[53]
Zhao et al.	2018	110	8 (at 100 W)	1.6	[54]
Hemming et al.	2013	27	4.4	1.4	[50]

Table 7.1.: Resume of the results presented in this thesis compared to the state of the art.

The results presented in this thesis are highlighted in blue. A particular focus must be posed to the column $P_{max}/(M^2)^2$. As explained in Sec. 3.3.1, if we consider a target at a certain distance, the fluence on it depends on the power and divergence of the laser beam. Thus, for applications such as IRCM, the ratio between the power and beam propagation factor is extremely important. The study with the highest $P_{max}/(M^2)^2$ ratio is [48]. However, it must be reminded that the author implemented an amplification stage in an OPO-OPA system. Therefore, we can observe how the results of this thesis are comparable to the

state of the art in the field, with a compact and robust design.

7.2. Outlook

The results presented in this thesis pave the way for additional investigation and improvements in the field of mid-IR OPOs.

As our results proved, power up-scaling attempts of the RISTRA and FIRE resonator have clashed with the laser damage threshold of the optics. Not being able to decrease the pump spot size, another method to reduce the oscillation threshold would be to provide the OPO with a small signal beam as seed. According to initial simulations, the threshold power would decrease significantly even for a small amount of seed power (some hundreds of mW). We can therefore think about using a QCL to provide it, keeping the system as compact as possible without having to implement an amplification stage. Otherwise, further power up-scaling efforts could focus on improving the pump source. Here we used an Ho^{3+} :LLF MOPA laser, delivering almost 70 W of average power at 2.065 μm . Both solid-state and fiber lasers can be considered. Ho^{3+} :YAG lasers have proven to be able to reach hundreds of watts, so they could be interesting pump sources. If instead we aim at improve the compactness and robustness of the overall system (pump source + OPO), pulsed all-fiber lasers could be used, such as Tm^{3+} , Ho^{3+} -codoped fiber lasers.

Other attempts for power up-scaling can include the use of an OC with higher reflectivity. In the present work a $R \sim 50\%$ at signal wavelength has been used for the RISTRA and FIRE resonators. Implementing mirrors with higher reflectivity would decrease the oscillation threshold of such cavities. However, simulations with SNLO showed that the slope efficiency would decrease for higher reflectivities. The highest power obtainable at 60 W according to the model is when using an OC with $R \sim 50\%$. Knowing however the issues of the simulation software above 30 W, further experimental studies are needed in order to determine the most performing OC reflectivity. A final idea in order to decrease the oscillation threshold of the non-planar ring cavities would be to implement them in a doubly resonant regime. Although nothing hampers this try, there is a practical issue to do this. As presented in Chap. 3, the RISTRA and FIRE resonators need an intra-cavity half-wave plate in order to compensate for the polarization rotation after one round-trip. If a DRO is wanted, we need a wave-plate at both the signal and idler. Considering that their wavelengths can be distant hundreds of nanometers, such optics feature may not be possible to achieve easily.

In addition to the output power, the beam quality of the output beams can also still be further improved. The study on the M^2 as a function of pump frequency done in Chap. 6 revealed the gain guiding and thermal lensing effects, caused by the focusing behavior of the resonant signal beam. Keeping the sig-

nal beam size equal to the pump beam at all power levels would assure a good overlap between the two beams, causing good beam quality. We can therefore think about implementing a telescope with moving lenses inside the OPO cavity. Modifying the distances between the two lenses could assure an optimal M^2 factor at all power levels.

As last consideration, in this thesis we focus mostly on signal resonant resonators. However, in the literature there has been some proof that idler-resonant (IR) cavities could lead to better performances, especially concerning the beam quality [92, 101]. Hence, in the future it could be interesting to operate the RIS-TRA and FIRE in that resonant regime.

A. ZGP crystal data

As presented in Chap. 2, the zinc germanium phosphide (ZGP) crystal presents several good properties for mid-IR generation. In this appendix informations and data sheet of this particular crystal are presented.

The ZGP is a crystal belonging to the 42m crystal class and with a tetragonal symmetry. As an uniaxial positive crystal, at a certain wavelength the extraordinary refractive index n_e is greater than the corresponding ordinary index n_o : $n_e > n_o$. When we consider the dependence of the refractive index on the wavelengths and temperature, two equations can thus be distinguished, depending on the polarization of the considered ray. According to [102], in the interval $2 \mu m \leq \lambda \leq 9 \mu m$, the Sellmeier equations are:

$$n_o^2 = 8.0409 + \frac{1.68625 \cdot \lambda^2}{\lambda^2 - 0.40824} + \frac{1.288 \cdot \lambda^2}{\lambda^2 - 611.05} \quad (\text{A.1})$$

$$n_e^2 = 8.0929 + \frac{1.8649 \cdot \lambda^2}{\lambda^2 - 0.41468} + \frac{0.84052 \cdot \lambda^2}{\lambda^2 - 452.105} \quad (\text{A.2})$$

The thermo-optic dispersion relations in the interval $1.5 \mu m \leq \lambda \leq 10.25 \mu m$ [103]:

$$\frac{dn_o}{dT} = \left(\frac{11.4188}{\lambda^3} - \frac{12.8971}{\lambda^2} + \frac{7.2947}{\lambda} + 14.2082 \right) \cdot (1 + 3.36 \cdot 10^{-3} \cdot (T - 20)) \cdot 10^{-5} \quad (\text{A.3})$$

$$\frac{dn_e}{dT} = \left(\frac{10.3798}{\lambda^3} - \frac{10.1785}{\lambda^2} + \frac{6.3877}{\lambda} + 15.6688 \right) \cdot (1 + 3.28 \cdot 10^{-3} \cdot (T - 20)) \cdot 10^{-5} \quad (\text{A.4})$$

where T is the temperature, expressed in Celsius degrees.

Only few terms in the nonlinear coefficient tensor are relevant and different from zero. If we consider as wavelength $\lambda = 4.8 \mu m$, the complete tensor is represented as [104]:

$$d = \begin{pmatrix} 0 & 0 & 0 & 75 & 0 & 0 \\ 0 & 0 & 0 & 0 & 75 & 0 \\ 0 & 0 & 0 & 0 & 0 & 75 \end{pmatrix} \quad (\text{A.5})$$


where the terms have the unit of pm/V. We can notice how $d_{14} = d_{25} = d_{36}$, which is a consequence of the crystal symmetry [66]. In this case the effective nonlinear coefficient is easily retrieved: $d_{eff} = d_{36} \sin(2\theta_{PM}) \cos(2\phi)$, with θ_{PM} the phase-matching angle.

B. Publications

1. M. A. Medina, M. Piotrowski, M. Schellhorn, F. R. Wagner, A. Berrou, and A. Hildenbrand-Dhollande. Beam quality and efficiency of ns-pulsed high-power mid-IR ZGP OPOs compared in linear and non-planar ring resonators. *Opt. Express*, **29** (14):21727-21737, 2021.
2. M. Piotrowski, M. A. Medina, M. Schellhorn, G. Spindler, and A. Hildenbrand - Dhollande. Effects of pump pulse energy and repetition rate on beam quality in a high-power mid-infrared ZnGeP₂ OPO. *Opt. Express*, **29**(2):2577-2586, 2021.



Beam quality and efficiency of ns-pulsed high-power mid-IR ZGP OPOs compared in linear and non-planar ring resonators

MANUEL ALESSANDRO MEDINA,^{1,2,*}  MARCIN PIOTROWSKI,¹ 
MARTIN SCHELLHORN,¹ FRANK R. WAGNER,² ANTOINE BERROU,¹
AND ANNE HILDENBRAND-DHOLLANDE¹

¹French-German Research Institute, ISL, 5, rue du General Cassagnou, 68301 Saint-Louis, France

²Aix Marseille Univ., CNRS, Centrale Marseille, Institute Fresnel, Marseille, France

*manuel-alessandro.medina@isl.eu

Abstract: We compare the performance of ns-pulsed mid-infrared optical parametric oscillators (OPOs) based on ZGP crystals in a simple linear cavity and two non-planar image-rotating resonators. Our 2 μm pump source is a 68 W 10 kHz diffraction limited Ho:LLF MOPA system. In a linear cavity, it allows us to generate up to 38 W of the total average power with $M^2 < 2.2$ from the ZGP OPO in the 3-5 μm range. Beam quality and stability are significantly improved in both types of non-planar ring resonators ($M^2 < 1.8$ in RISTRA and $M^2 < 1.4$ in FIRE), while the total average power is above 21 W. Factors influencing the beam quality such as average power and pump repetition rate are studied in detail.

© 2021 Optical Society of America under the terms of the [OSA Open Access Publishing Agreement](#)

1. Introduction

Demand for laser sources in the middle-infrared (mid-IR) wavelength range stems from areas like remote sensing, free space communication or optronic countermeasures in defense [1]. Many of these applications require a high-average power source with good beam quality. A mature technique to deliver such radiation is frequency down-conversion through optical parametric oscillators (OPO) and amplifiers (OPA) [2]. Indeed, the availability of other solid state sources is restricted to quantum cascade lasers [3] and lasers based on chalcogenides doped with transition metals [4], which are limited to few watts of average power. Nonlinear crystal of zinc germanium phosphide (ZGP) is known for its high nonlinear coefficient and its thermal and mechanical properties [5,6]. It is particularly suitable for high power laser sources covering the mid-IR region by nonlinear conversion from 2 μm pump wavelength, where wide choice of high power pump lasers with excellent beam quality is available.

Few experimental high-power sources based on ZGP OPOs reaching more than 20 W have been demonstrated, but many suffered from limited stability or beam quality. The highest power currently reported is a two-stage ZGP OPO-OPA pumped by a 20 kHz pulse repetition rate Ho:YAG [7]. The first stage ZGP OPO delivered 78 W ($M^2 \approx 3$), while the amplifier stage had a maximum output of 161 W ($M^2 \approx 3.6$). However, since MOPA systems are relatively complex, it is valuable to investigate single stage OPOs. The highest average power demonstrated with such a setup reached 110 W [8], but beam quality at 100 W was very poor ($M^2 \approx 9$), and the operation at maximum output power lasted only few seconds before crystal damage. An $M^2 \approx 4$ for stable operation was reported at 30 W. All aforementioned experiments utilized 4-mirror planar ring resonators. In a similar cavity arrangement but with two separate ZGP crystals placed in series 41 W with $M^2 = 4.4$ was reported [9]. Other demonstrations of stable single-stage ZGP OPO include 27 W ($M^2 = 4$) with two ZGPs in a linear resonator [10] and 22 W ($M^2 = 1.4$) in a 3-mirror V-shaped planar ring cavity [11].

In principle, the mode discrimination could be improved by increasing the OPO cavity length. However, when the efficiency and compactness of the overall system are crucial, this method is not applicable. The most troublesome in above experiments are the thermal effects leading to the build-up of higher order modes in the cavities and as consequence degradation of the beam quality. The issue of thermal lens was addressed by compensation with negative lens [12] or Galilean telescope [13]. This approach was proven effective in the demonstration of a 102 W MOPA system [14].

Another technique to improve the beam quality is the use of ring resonators with a non-planar configuration, as first investigated by Smith *et al.* [15]. Two particular types of non-planar image-rotating ring resonators have been proposed and proved successful in beam quality improvement: the 90° Rotated Image Singly-resonant Twisted RectAngle (RISTRA) [16] and the Fractional Image Rotation Enhancement (FIRE) [17] cavities.

The type of resonator used for ns-pulsed OPO plays an important role in addressing the issues of stability and beam quality in high-power sources exceeding tens of watts in the mid-IR range, but few published studies adequately tested the performance of different types of resonators in OPO experiments. To date, the direct comparison of high-power OPO performance in different resonators has not yet been deeply examined. Most of the previous studies dealt with low-repetition pump sources and focused on increasing pulse energy in cases where high Fresnel number is required due to crystal damage constrains [18,19]. Other attempts include comparison of the RISTRA with the linear cavity at low repetition rate [20] or comparison between singly- and doubly-resonant regimes in a high-repetition rate ZGP OPO in planar ring cavity setups [21]. The FIRE cavity is of particular interest as it has never been tested before at high-power operation, although it has proven to enhance the beam quality in high-energy low-repetition rate systems [12].

The two main effects playing a role in the deterioration of the beam quality are thermal lens [22] and gain guiding [23,24]. The first depends on the heat absorbed by the crystal and is thus pump power dependent. On the contrary, gain guiding arises from the spatial intensity distribution of pump pulse energy. The influence of both effects on the beam quality has been studied in details in the RISTRA, under different pumping conditions [25].

In this article, we compare the performance of three OPO cavities: linear resonator, RISTRA and FIRE cavities. When possible, cavities with similar round trip are compared. We demonstrate a high average power ZGP OPO reaching up to 38 W of total output power in the linear cavity with an $M^2 = 2.2$ for the signal beam. The beam quality is then improved using the non-planar ring cavities, reaching a value of $M^2 = 1.4$ for 21 W of total output power in the FIRE cavity. This is the first demonstration of such cavity at high repetition rate. We investigate experimentally the scaling of the beam quality with output power and pulse repetition rate, expanding previous results of our group obtained using the RISTRA cavity [25].

2. Experimental setup

The scheme of our experimental setup is presented in Fig. 1(a). A 10 kHz pulse repetition rate high power Ho:LLF MOPA system [26] pumps a ZGP OPO. The 2 μm pump source delivers 68.7 W at 2065 nm in TEM₀₀ operation with an optical-to-optical efficiency of 61.5 % and has a diffraction limited beam quality ($M^2 \approx 1$) at maximum pulse energy of 6.9 mJ. The pulse duration is 25 ns. The 300 mm lens focuses the pump beam from the Ho:LLF to a spot diameter of ~ 1.1 mm in the center of the ZGP crystal, maintaining a pump fluence < 1.5 J/cm² to avoid any risk of damage and anticipating for possible thermal effects affecting the energy density. Even though the reported laser induced damage thresholds for the ZGP crystals are ~ 4 J/cm² [27,28], we operated safely below this limit. The Ho:LLF source is linearly polarized and a half-wave plate controls the polarization state. Then, a Pockels cell and a polarizer allow power adjustment and pulse picking without affecting the pulse properties. A second half-wave plate

controls the polarization state at the entrance of the OPO. Behind the OPO cavity, the residual pump is reflected by a dichroic mirror, transparent for the 3–5 μm output beams. Then, a CaF_2 wedge is used to pick off part of the two OPO beams for beam quality analysis. The pump beam power and the total OPO output power are monitored with a thermal power meter.

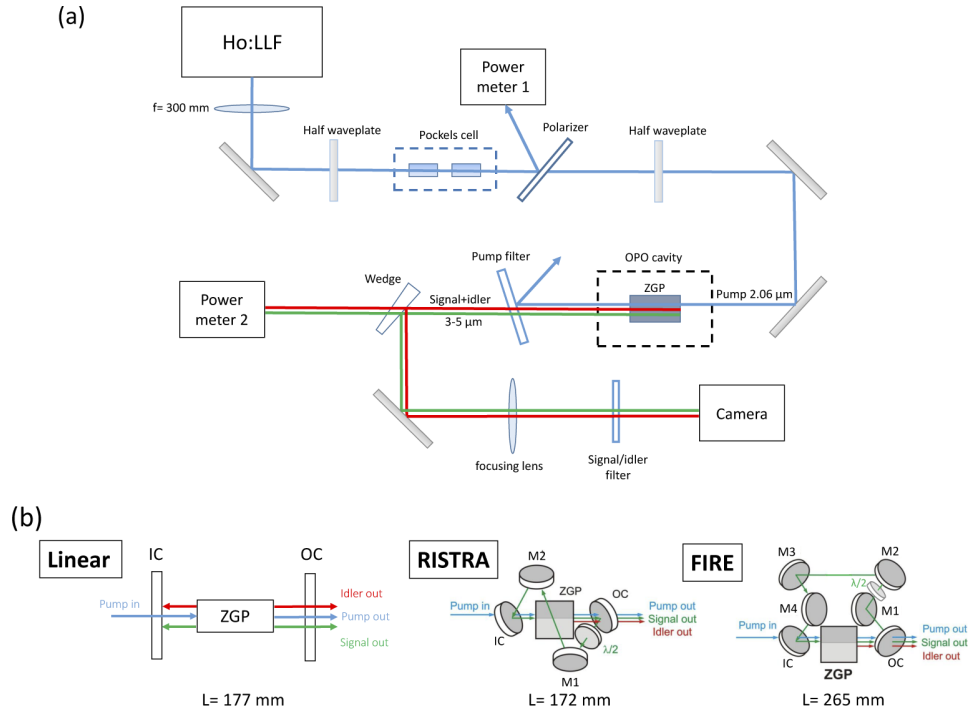


Fig. 1. (a) The scheme of the experimental setup. (b) The three different OPO cavities that were alternated in the experimental setup. L denotes the optical round-trip length of the cavities.

The beam quality measurements are performed by recording beam profiles along the focused output beams. The profiles are monitored with an infrared pyroelectric array sensor (mks Ophir Pyrocam IV Beam Profiling Camera). The camera resolution is 320x320 pixels with a pixel pitch of 80 μm . This camera is used in chopped (50 Hz) or triggered (100 Hz) mode for all beam images presented here.

2.1. Nonlinear crystals and OPO resonators

In the present study, we used two ZGP crystals with the size of 6 x 6 mm^2 (aperture) x 20 mm (length), and cut at 55° with respect to the optical axis to allow type-I phase matching. Their end faces are AR-coated for the pump and the output wavelengths (3–5 μm). They were purchased from the same manufacturer (Harbin Huigong Science & Technology Co., Ltd.). Considering negligible absorption of the coating layers and taking into account their reflection, by measuring the power transmitted through the crystals, we determined different absorption coefficient at 2.06 μm : $\alpha_1 = 0.033 \text{ cm}^{-1}$ and $\alpha_2 = 0.044 \text{ cm}^{-1}$. This corresponds to an absorption of $\approx 6.4\%$ and $\approx 8.5\%$ of the input power, respectively.

The ZGPs were wrapped in indium foil and mounted inside the optical cavities in copper holders, serving as heat sinks. The copper holders were then mounted in a rotational stage to allow angle tuning. For the measurements in the linear cavity, the holder was also water cooled.

The configurations of the cavities used in this study are shown in Fig. 1(b), with L denoting the optical round-trip of each one. It was calculated from the geometrical length of the resonators, accounting for the length and refractive index of the ZGPs. While the linear resonator gives the agility of its length, the non-planar ones are monolithic structures and do not require any mirror adjustment.

The linear cavity is composed of two flat mirrors, it is single pump pass and doubly-resonant. The input coupler (IC) is highly transmissive for the pump wavelength ($T > 95\%$) and highly reflective in the 3-5 μm range. The output coupler mirror (OC) is also highly transmissive for the pump and has $\approx 50\%$ reflectivity for both signal and idler wavelengths. For results presented here, the cavity was set to a physical length of 46 mm, corresponding to a 177 mm optical round trip length. This guarantees a short build-up time (thus good efficiency) and similar optical length with respect to the RISTRA. To avoid back reflection into the pump source, the cavity was operated with a slight misalignment.

The first non-planar cavity used in this study is the Rotated Image Singly-resonant Twisted RectAngle (RISTRA) ring resonator [16], based on 90° image rotation and composed of 4 flat mirrors in a non-planar configuration (Fig. 1(b)). Contrary to the linear cavity, it is operated in singly signal resonant regime. The pump beam enters via a dichroic input coupling mirror, which is tilted by 32.7° . It is highly transmissive for 2 μm ($T = 86\%$) and highly reflective for the signal beam. The output coupler mirror is transparent for the pump and idler and has a reflectivity of $\approx 50\%$ for the signal beam. The other two mirrors (M1 and M2) are identical to the IC. The half waveplate between OC and M1 compensates the polarization rotation in the resonator and keeps it constant after a cavity round trip. The physical length of the resonator is 130 mm, which corresponds to an optical round trip of around 172 mm.

The second non-planar cavity is the Fractional Image Rotation Enhancement cavity (FIRE), composed of 6 flat mirrors [17] (Fig. 1(b)). Likewise the RISTRA, the IC mirror ($T = 84\%$) allows the pump beam to enter and pass through the ZGP crystal while reflecting the signal beam. Again, the OC has a reflectivity of $\approx 50\%$ for the signal beam. The other 4 mirrors that make the round trip in the resonator are all identical to the IC, and a half waveplate compensates the polarization rotation. The physical length of this cavity is 222 mm, corresponding to an optical round trip of 265 mm.

3. Results and discussion

3.1. Comparison of two ZGPs with different absorptances

The two ZGP crystals were initially tested in the linear OPO cavity. The graph in Fig. 2 shows the total OPO output power as a function of the pump power for both. The conversion thresholds are equal, but the slope efficiency is different. The crystal with less absorption (the #1) gives better results. Thus the absorption has an influence on the maximum output power achievable from the OPO.

The beam quality of the output beams at low average power, i.e. negligible thermal effects, depends exclusively on the cavity length and geometry [24,29]. Therefore the beam quality close above threshold does not differ for the two crystals. Up-scaling the output power leads to a deterioration of the output beam quality due to the rise of a thermal gradient in the ZGP and consequently thermal lens [30]. This effect is more evident in the second crystal used, having higher absorption coefficient. That is why the first ZGP yielded the highest output power (see section 3.2). However, dust contamination caused coating damage at moderate pump power. This damage prevented us from using this crystal in the non-planar cavities. Instead, the second ZGP with higher absorption has been used for the rest of the results presented.

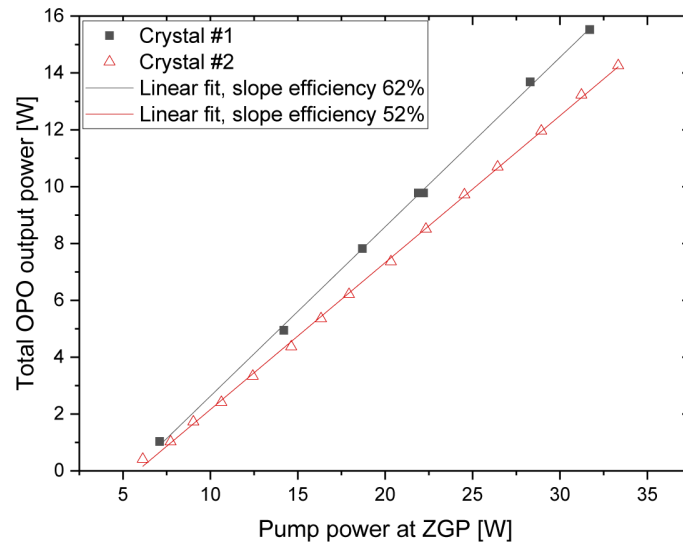


Fig. 2. Total (signal + idler) OPO output power as a function of input pump average power for the two ZGP crystals used in linear resonator (177 mm optical round-trip, doubly resonant regime).

3.2. 38 W linear cavity OPO

Using the ZGP #1, the performance of the linear cavity was studied. Operating at a repetition rate of 10 kHz, we achieved a total output power of 38 W for 66 W of input power, corresponding to a slope efficiency of 62%. The total output power (signal + idler) as a function of the pump power is presented in Fig. 3(a).

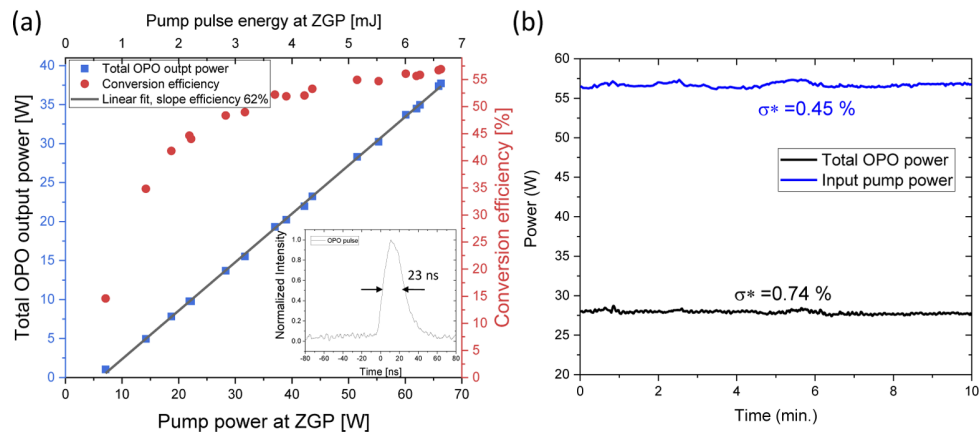


Fig. 3. (a) Total OPO output power and conversion efficiency as a function of pump power. The top axis displays the pump pulse energy. Inset shows the OPO temporal pulse profile at maximum output power. (b) OPO and pump power stability measurement at 28 W over 10 minutes. The labels indicate the corresponding relative standard deviation.

The optical-to-optical efficiency (red circles) is calculated as the ratio between the incident pump power and the total OPO output power. Its maximum value achieved at the maximum output power was 57%. The OPO temporal pulse width at maximum output power (38 W) is

presented as an inset of Fig. 3(a). Its duration is 23 ns (FWHM), corresponding to a peak power of 165.2 kW. The power fluctuations of the OPO and the pump source are presented in Fig. 3(b). The stability of the OPO was not measured at maximum output power in order to monitor the pump source at the same time. The OPO output fluctuations follow the trend of the pump and have a slightly higher relative standard deviation (σ^*) over a period of 10 minutes (0.74 % vs 0.45 %).

The amount of heat in the nonlinear crystal scales with the input power, inducing a positive thermal lens. As a consequence, the beam quality deteriorates as the incident power increases. Figure 4(a) shows this evolution. To measure the beam quality M^2 factor, the output beams were focused with a $f = 500$ mm CaF_2 lens and their diameters were measured in both X and Y directions. For clarity, only the signal beam is presented, but the idler showed similar behavior and M^2 values. The beam shapes are not symmetric, which is a consequence of walk-off and cavity misalignment, deliberately introduced to avoid back reflection and optical feedback to the pump laser.

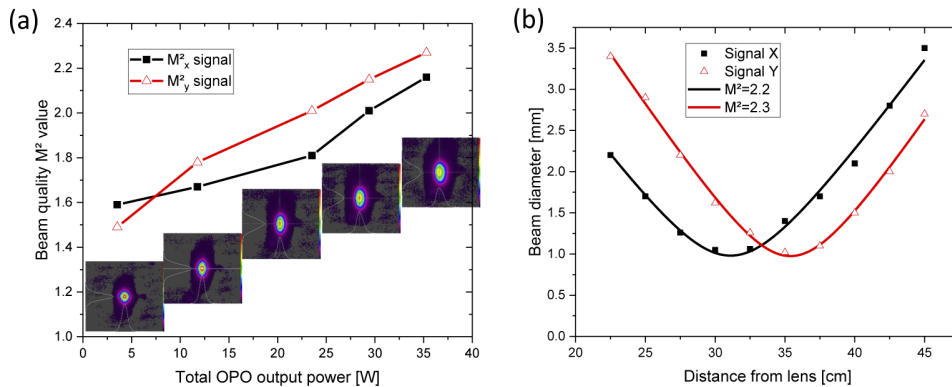


Fig. 4. (a) The variation of the signal beam quality (M^2) with total OPO output power. The corresponding near field beam images at a distance of 25 cm from the lens are shown. (b) M^2 value measurement at maximum output power of 38 W.

Above threshold, where the thermal effects are low, the $M^2 \approx 1.5$ for an output power of 3.5 W. Then, as the thermal load into the crystal increases, the beam quality factor deteriorates, reaching a value of $M^2 \approx 2.2$ at maximum output power. The beam quality measurement at maximum output power is depicted in Fig. 4(b).

The output power and the beam quality reported here exceeds previous reports from linear doubly-resonant ZGP OPOs [31,32]. The demonstrations of higher output powers from single-stage ZGP OPOs used different resonant regime and planar ring resonators [8,9]. However, the reported beam quality factors were $M^2 \approx 4$ at 30 W of output power and $M^2 \approx 4.3$ at 41 W, respectively. Therefore, at comparable output powers, we recorded better beam quality, despite the use of a linear resonator. In accordance with our results are those reported by Lippert *et al.* [11]. They obtained 22 W of output power with M^2 of 1.4 in a V-shaped 3-mirror ring cavity. Our report presents what is, to the best of our knowledge, the up to date best beam quality at this power level from a single stage ZGP OPO. The findings of this study are only pump power limited and they are promising for further up-scaling.

3.3. Performance comparison of the three cavities

The performances of the three cavities were compared using the same ZGP crystal (ZGP #2). Fig. 5(a) shows the total (signal + idler) OPO output power as a function of average pump

power for the three cavities tested. We achieved a total output power of 25 W (RISTRA) and 21 W (FIRE) in the 3-5 μm range. The input power available in this case was lower due to the transmission of the ICs. The crystal was not tested at full pump power in the linear cavity to avoid any possible damage. However, from the slope and threshold it can be anticipated that it would give ≈ 28 W of total output power when pumped with 60 W (dashed line).

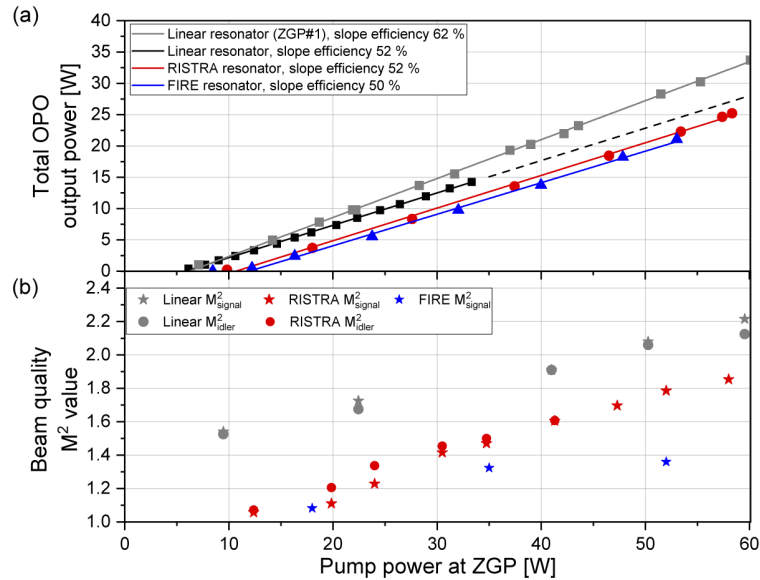


Fig. 5. (a) Performance comparison of the same ZGP crystal in different OPO cavities: a linear cavity (black squares), a RISTRA cavity (red circles), and a FIRE cavity (blue triangles). The grey squares represent the performances of the ZGP #1 in linear cavity, as shown in Fig. 3(a). (b) Variation of the signal and idler beam quality M^2 factor with input pump power for the three resonators.

The slope efficiency is around 50 % for each resonator. More specifically, their values are: 52 % (linear and RISTRA) and 50 % (FIRE). It neither depends on the cavity resonant type nor the cavity geometry. The pulses, similar to the one presented in Fig. 3(a), also present no significant difference between the three resonators. The main difference among the cavities is the conversion threshold. As the optical length per round trip of the linear and RISTRA cavities are comparable, it can be stated that the doubly-resonant regime lowers the conversion threshold. This agrees with previous theoretical [33] and experimental [21] reports. Additionally, if we compare the FIRE and RISTRA cavities, the dependence of the threshold on the cavity length can be observed. Since FIRE is singly-resonant and the longest, its threshold is the highest. Likewise the results recorded in the linear cavity, the maximum output power is limited by the pump.

The beam quality M^2 value for different output powers was measured for the three cavities. Their variation as function of pump power is presented in Fig. 5(b), averaged between X and Y directions. The evolution in the linear cavity was similar to the one presented in Fig. 4(a). Therefore, we assumed same scaling and M^2 values with average input power. The idler beam quality was measured for the linear resonator and at lower powers of the RISTRA. Since there were no differences with respect to the signal beam, such measure was not performed for the FIRE, assuming same M^2 values as the signal beam. For the RISTRA and FIRE, their beam quality measurements close to threshold and at maximum output power, corresponding respectively to the first and last point of Fig. 5(b), are presented in Fig. 6 for the resonant signal beam. Close to the threshold the thermal effects are negligible, thus the beam quality mostly depends on the

geometry of the resonant cavity. This leads to a nearly diffraction-limited M^2 factor for both RISTRA and FIRE, despite their different threshold and build-up time. At higher powers levels, with the arise of thermal effects inside the ZGP, there is a deterioration of the beam quality of the output beams. For the RISTRA cavity, at a total output power of 25 W (at 58 W of input power), we obtained stable operation with the signal M^2 value around 1.8. A similar effect is observed for the FIRE, where at the maximum output power of 21 W (at 53 W of input power), we obtained an M^2 factor of 1.4.

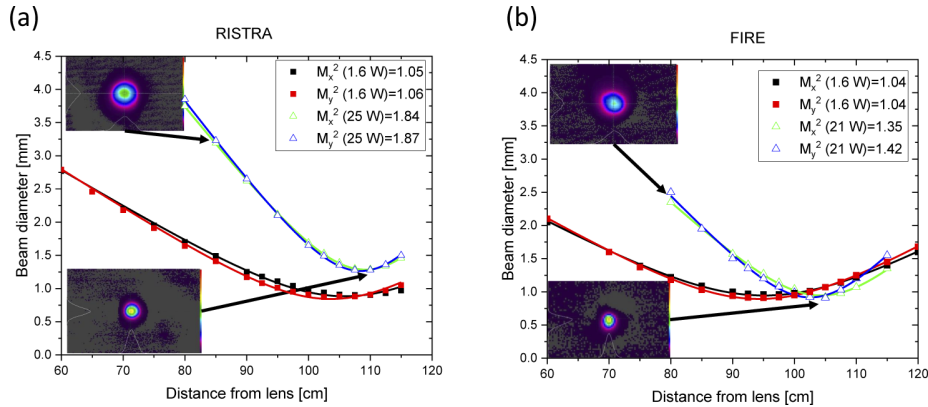


Fig. 6. (a) M^2 value measurement at total output power of 1.6 W and 25 W in RISTRA cavity. (b) M^2 value measurement at total output power of 1.6 W and 21 W in FIRE cavity.

A direct comparison between linear and RISTRA cavity has already been done at low repetition rate [20,34], resulting in an improvement of the beam quality of the non-resonant idler beam for the RISTRA cavity. However, in the low power limit this improvement was marginal. In our study, such comparison is extended to high repetition rate regime and done considering the resonant signal beam. Moreover, we include also the FIRE cavity, never tested at high average power. Our results on the beam quality show a significant improvement on the M^2 value due to the non-planar geometry. This can be clearly seen if we compare the beam quality of the output beams close to threshold for the three cavities. While for the non-planar cavities the M^2 values are diffraction-limited, in the case of the linear resonator it is around 1.5 (see Fig. 4(a)). Although they operate in different resonant regimes, since the RISTRA and linear cavity have comparable round trip lengths, this result gives further insights that image-rotating configuration helps suppressing higher order modes and enhances the beam quality of the OPO output beams.

Regardless of the different total output power of each cavity (with the linear resonator giving the highest output), if the pump power is similar, so are the thermal effects inside the ZGP. Thus, in similar conditions (around 50 W of input power, Figure 5(b)), the beam quality factor M^2 of the output beams improves from an initial value of 2.1 in the linear cavity ($P_{in} \approx 50$ W) to a value of 1.4 in the case of the FIRE ($P_{in} \approx 53$ W). The additional improvement of the FIRE with respect to the RISTRA cavity (1.4 vs 1.8) confirms preliminary conclusions of previous works, which stated that the fractional image rotation provides a better mode suppression at low repetition rates than the 90° rotation [17].

3.4. Beam quality scaling with repetition rate

The dependence of the beam quality on the pump repetition rate was also investigated, as done previously in the case of the RISTRA [25]. Using a Pockels cell, the pump repetition rate is controlled by pulse picking without affecting the pulse properties. To isolate the dependence of the beam quality on the frequency, the pump pulse energy was kept at the constant value of 6 mJ

and no other pulse properties were modified. The measured beam quality M^2 factor as a function of the pump repetition rate is presented in Fig. 7 for the RISTRA and FIRE cavities. This study could not be performed in the linear cavity: the back reflection of the IC was heating the Pockels cell, affecting the polarization of the pump beam.

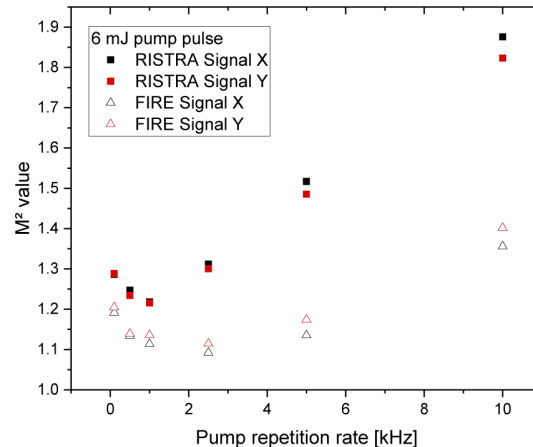


Fig. 7. M^2 values in FIRE and RISTRA resonators for different repetition rates of the pump source at constant pump pulse energy of 6 mJ.

Intuitively, lowering the repetition rate, one might expect an improvement of the beam quality as the one found when the average power is lowered. However, the measured beam quality shows a minimum at different frequencies for the two cavities. For the RISTRA, starting from an initial value of 1.3 at 0.1 kHz, the M^2 drops to a minimum value of 1.2 at 1 kHz, then increases for higher repetition rates reaching the final value of 1.8 at 10 kHz. In the FIRE cavity, the initial M^2 value at 0.1 kHz is 1.2, it drops to a minimum of 1.1 at 2.5 kHz and then increases to 1.4 at 10 kHz.

This counterintuitive behavior is the result of a trade-off between the thermal lensing and the gain guiding effects, as explained in our previous paper [25], where simulations supported our interpretation. The previous results were limited only to the RISTRA cavity, here we extend these conclusions to the FIRE resonator. The different positions of the minimum might be due to the different lengths of the cavities. Further studies are needed to confirm it. Additionally, the M^2 data presented supports the improvement of the beam quality in the FIRE compared with the RISTRA. Indeed, at all repetition rates, the FIRE resonator presented a better M^2 factor.

4. Conclusions

In this paper, we compared the performances of three different types of single stage ZGP OPO in similar pumping conditions. We achieved a maximum output power of 38 W with $M^2=2.2$ in the 3 - 5 μm spectral range using a doubly-resonant linear cavity. This is, to our knowledge, the best beam quality at this power level obtained with a linear resonator. Non-planar ring cavities have been used to improve the beam quality, obtaining $M^2=1.8$ ($P=25$ W) in RISTRA and $M^2=1.4$ ($P=21$ W) in FIRE. This is the first comparison of such cavities at high repetition rates and high average power. A low conversion threshold of the non-planar ring cavities is hampered by the fact that they are singly-resonant and for the FIRE additionally by the greater length. Therefore, a possible method to decrease the threshold and improve the performances would be to design and build a miniaturized version of these cavities. Additionally, a cooling system for the crystals, not present in current designs, could be implemented in order to improve the thermal management of

the ZGP. The dependence of the M^2 with the pump repetition rate for the FIRE cavity confirms that there is a trade-off between the thermal lensing and the gain guiding and suggests some optimal condition to operate with the best beam quality.

Up to now, the highest average powers reported in the mid-IR region are provided by complex MOPA systems with limited beam quality. Our report shows the feasibility of using simpler, quasi-monolithic OPO resonators with good conversion efficiency and with a significant improvement of the output beam quality. Our results are currently pump power limited and further developments can lead to a better management of thermal effects and further up scaling of the output power from ZGP OPO while maintaining good beam quality.

Funding. Direction Générale de l'Armement.

Acknowledgments. Portions of this work were presented at the *OSA Laser Congress* in 2020 [35], and the *9th EPS-QEOD Europhoton Conference on Solid-State, Fibre, and Waveguide Coherent Light Sources* in 2020 [36,37].

Disclosures. The authors declare no conflicts of interest.

Data availability. Data underlying the results presented in this paper are not publicly available at this time but may be obtained from the authors upon reasonable request.

References

1. K. L. Vodopyanov, *Laser-based mid-infrared sources and applications* (John Wiley & Sons, Inc., 2020), chap. 3.
2. V. Petrov, "Frequency down-conversion of solid-state laser sources to the mid-infrared spectral range using non-oxide nonlinear crystals," *Prog. Quantum Electron.* **42**, 1–106 (2015).
3. Y. Yao, A. J. Hoffman, and C. F. Gmachl, "Mid-infrared quantum cascade lasers," *Nat. Photonics* **6**(7), 432–439 (2012).
4. S. Mirov, I. Moskalev, S. Vasilyev, V. Smolski, V. Federov, D. Martyshkin, J. Peppers, M. Mirov, A. Dergachev, and V. Gapontsev, "Frontiers of mid-IR lasers based on transition metal doped chalcogenides," *IEEE J. Sel. Top. Quantum Electron.* **24**(5), 1–29 (2018).
5. P. G. Schunemann, K. T. Zawilski, L. A. Pomeranz, D. J. Creeden, and P. A. Budni, "Advances in nonlinear optical crystals for mid-infrared coherent sources," *J. Opt. Soc. Am. B* **33**(11), D36–D43 (2016).
6. G. Boyd, E. Buehler, F. Storz, and J. Wernick, "Linear and nonlinear optical properties of ternary $A^{II}B^{IV}C^V_2$ chalcopyrite semiconductors," *IEEE J. Quantum Electron.* **8**(4), 419–426 (1972).
7. G. Liu, S. Mi, K. Yang, D. Wei, J. Li, B. Yao, C. Yang, T. Dai, X. Duan, L. Tian, and Y. Ju, "161 W middle infrared ZnGeP₂ MOPA system pumped by 300 W-class Ho:YAG MOPA system," *Opt. Lett.* **46**(1), 82–85 (2021).
8. B.-R. Zhao, B.-Q. Yao, C.-P. Qian, G.-Y. Liu, Y. Chen, R.-X. Wang, T.-Y. Dai, and X.-M. Duan, "231 W dual-end-pumped Ho:YAG MOPA system and its application to a mid-infrared ZGP OPO," *Opt. Lett.* **43**(24), 5989–5992 (2018).
9. B.-Q. Yao, Y.-J. Shen, X.-M. Duan, T.-Y. Dai, Y.-L. Ju, and Y.-Z. Wang, "A 41-W ZnGeP₂ optical parametric oscillator pumped by a Q-switched Ho:YAG laser," *Opt. Lett.* **39**(23), 6589–6592 (2014).
10. A. Hemming, J. Richards, A. Davidson, N. Carmody, S. Bennetts, N. Simakov, and J. Haub, "99 W mid-IR operation of a ZGP OPO at 25% duty cycle," *Opt. Express* **21**(8), 10062–10069 (2013).
11. E. Lippert, H. Fonnum, G. Arisholm, and K. Stenersen, "A 22-watt mid-infrared optical parametric oscillator with V-shaped 3-mirror ring resonator," *Opt. Express* **18**(25), 26475–26483 (2010).
12. M. Schellhorn, G. Spindler, and M. Eichhorn, "Improvement of the beam quality of a high-pulse-energy mid-infrared fractional-image-rotation-enhancement ZnGeP₂ optical parametric oscillator," *Opt. Lett.* **42**(6), 1185–1188 (2017).
13. M. Schellhorn, G. Spindler, and M. Eichhorn, "Mid-infrared ZGP OPO with divergence compensation and high beam quality," *Opt. Express* **26**(2), 1402–1410 (2018).
14. C.-P. Qian, B.-Q. Yao, B.-R. Zhao, G.-Y. Liu, X.-M. Duan, T.-Y. Dai, Y.-L. Ju, and Y.-Z. Wang, "High repetition rate 102 W middle infrared ZnGeP₂ master oscillator power amplifier system with thermal lens compensation," *Opt. Lett.* **44**(3), 715–718 (2019).
15. A. V. Smith and M. S. Bowers, "Image-rotating cavity designs for improved beam quality in nanosecond optical parametric oscillators," *J. Opt. Soc. Am. B* **18**(5), 706–713 (2001).
16. A. V. Smith and D. J. Armstrong, "Nanosecond optical parametric oscillator with 90° image rotation: design and performance," *J. Opt. Soc. Am. B* **19**(8), 1801–1814 (2002).
17. S. Bigotta, G. Stöppler, J. Schöner, M. Schellhorn, and M. Eichhorn, "Novel non-planar ring cavity for enhanced beam quality in high-pulse-energy optical parametric oscillators," *Opt. Mater. Express* **4**(3), 411–423 (2014).
18. A. Dergachev, D. Armstrong, A. Smith, T. Drake, and M. Dubois, "3.4 μm ZGP RISTRA nanosecond optical parametric oscillator pumped by a 2.05- μm Ho:YLF MOPA system," *Opt. Express* **15**(22), 14404–14413 (2007).
19. M. Eichhorn, M. Schellhorn, M. W. Haakestad, H. Fonnum, and E. Lippert, "High-pulse-energy mid-infrared fractional-image-rotation-enhancement ZnGeP₂ optical parametric oscillator," *Opt. Lett.* **41**(11), 2596–2599 (2016).
20. G. Marchev, M. Reza, V. Badikov, A. Esteban-Martin, G. Stoppler, M. Starikova, D. Badikov, V. Panyutin, M. Eichhorn, G. Shevyrdyaeva, A. Tyazhev, S. Sheina, A. Agnesi, A. Fintsova, and V. Petrov, "Mid-infrared rotated

- image singly resonant twisted rectangle optical parametric oscillator based on HgGa₂S₄ pumped at 1064 nm,” *Appl. Opt.* **53**(33), 7951–7962 (2014).
21. Y. Chen, G. Liu, B. Yao, R. Wang, C. Yang, X. Duan, T. Dai, and Y. Wang, “Comparison of mid-infrared ZnGeP₂ rectangle ring optical parametric oscillators of three types of resonant regimes,” *Appl. Opt.* **58**(15), 4163–4169 (2019).
 22. J. P. Gordon, R. C. C. Leite, R. S. Moore, S. P. S. Porto, and J. R. Whinnery, “Long-transient effects in laser with inserted liquid samples,” *J. Appl. Phys.* **36**(1), 3–8 (1965).
 23. F. Salin and J. Squier, “Gain guiding in solid-state lasers,” *Opt. Lett.* **17**(19), 1352–1354 (1992).
 24. G. Arisholm, R. Paschotta, and T. Südmeyer, “Limits to the power scalability of high-gain optical parametric amplifiers,” *J. Opt. Soc. Am. B* **21**(3), 578–590 (2004).
 25. M. Piotrowski, M. A. Medina, M. Schellhorn, G. Spindler, and A. Hildebrand-Dhollande, “Effects of pump pulse energy and repetition rate on beam quality in a high-power mid-infrared ZnGeP₂ OPO,” *Opt. Express* **29**(2), 2577–2586 (2021).
 26. M. Schellhorn and G. Spindler, “High-Efficient Resonantly Pumped Q-Switched Ho:LLF MOPA System,” in *Laser Congress 2019 (ASSL, LAC, LS&C)*, (Optical Society of America, 2019), p. JTh3A.18.
 27. K. T. Zawilski, S. D. Setzler, P. G. Schunemann, and T. M. Pollak, “Increasing the laser-induced damage threshold of single-crystal ZnGeP₂,” *J. Opt. Soc. Am. B* **23**(11), 2310–2316 (2006).
 28. K. T. Zawilski, P. G. Schunemann, S. D. Setzler, and T. M. Pollak, “Advances in single crystal ZnGeP₂ processing for high energy applications,” in *Conference on Lasers and Electro-Optics/Quantum Electronics and Laser Science Conference and Photonic Applications Systems Technologies*, (Optical Society of America, 2008), p. JTuA28.
 29. W. A. Neuman and S. P. Velsko, “Effect of cavity design on optical parametric oscillator performance,” in *Advanced Solid State Lasers*, (Optical Society of America, 1996), p. OP12.
 30. W. Koechner, in *Solid-State Laser Engineering*, (Springer, 2006), chap. 7, sixth ed.
 31. I. Elder, “Thulium fiber laser pumped mid-IR source,” in *Laser Technology for Defense and Security V*, vol. 7325 M. Dubinskii and S. G. Post, eds., International Society for Optics and Photonics (SPIE, 2009), pp. 98–108.
 32. C. Kieleck, A. Berrou, B. Donelan, B. Cadier, T. Robin, and M. Eichhorn, “6.5 W ZnGeP₂ OPO directly pumped by a Q-switched Tm³⁺-doped single-oscillator fiber laser,” *Opt. Lett.* **40**(6), 1101–1104 (2015).
 33. R. W. Boyd, in *Nonlinear Optics*, (Elsevier, 2007), chap. 2, 3rd ed.
 34. G. Marchev, A. Tyazhev, G. Stöppler, M. Eichhorn, P. G. Schunemann, and V. Petrov, “Comparison of linear and RISTRA cavities for a 1064-nm pumped CdSiP₂ OPO,” in *Nonlinear Frequency Generation and Conversion: Materials, Devices, and Applications XI*, vol. 8240 K. L. Vodopyanov, ed., International Society for Optics and Photonics (SPIE, 2012), pp. 70–76.
 35. M. Piotrowski, M. A. Medina, G. Spindler, M. Schellhorn, and A. Hildenbrand-Dhollande, “Beam Quality Enhancement in High Power mid-IR ZGP OPO Sources: a Focus on Thermal Lens Build-up,” in *Laser Congress 2020 (ASSL, LAC)*, (Optical Society of America, 2020), p. JTh2A.8.
 36. M. Piotrowski, M. Medina, M. Schellhorn, and A. Hildenbrand-Dhollande, “Temporally resolved studies of thermal effects in high power ZGP OPO pumped by high-repetition Ho:LLF MOPA system,” *EPJ Web Conf.* **243**, 18001 (2020).
 37. M. Medina, M. Piotrowski, M. Schellhorn, F. Wagner, A. Berrou, and A. Hildenbrand-Dhollande, “38 W high repetition rate ZGP OPO and novel approaches to improve beam quality in miniaturized non-planar cavities,” in *Europhysics Conference Abstracts (9th EPS-QEOD Europhoton Conference)*, (European Physical Society, 2020), p. THA3.7.



Effects of pump pulse energy and repetition rate on beam quality in a high-power mid-infrared ZnGeP₂ OPO

MARCIN PIOTROWSKI,^{1,*}  MANUEL ALESSANDRO MEDINA,^{1,2} 
MARTIN SCHELLHORN,¹ GERHARD SPINDLER,³ AND ANNE
HILDENBRAND-DHOLLANDE¹

¹French-German Research Institute, ISL, 5, rue du General Cassagnou, 68301 Saint-Louis, France

²Aix Marseille Univ., CNRS, Centrale Marseille, Institute Fresnel, Marseille, France

³Untere Gaisäckerstr, 10, 79761 Waldshut-Tiengen, Germany

*marcin.piotrowski@isl.eu

Abstract: We report on changes of beam quality with rising pump pulse energy and repetition rate in a high-power mid-infrared ZnGeP₂ (ZGP) OPO in a non-planar cavity. The ZGP OPO generates 25 W in 3 – 5 μm pumped by a 10 kHz Q-switched Ho:LLF MOPA system at 2 μm. The beam quality factor increases from nearly diffraction-limited at OPO threshold to a $M^2 = 1.8$ at maximum pump power. The degradation can be attributed to thermal lensing and gain guiding effects in the nonlinear crystal. To discriminate between those effects, we monitored the beam quality as a function of the repetition rate at the highest pump pulse energy using a Pockels cell as a pulse picker. Therefore, the heat load inducing thermal lensing increases linearly, whereas gain guiding remains nearly unaffected. M^2 shows a minimum of 1.2 at 1 kHz, starting from 1.3 at 100 Hz and rising to 1.8 at 10 kHz. Those findings have been reproduced by numerical simulations. Further investigations show the transient evolution of beam quality, revealing the thermal lens build-up process to the steady-state.

© 2021 Optical Society of America under the terms of the [OSA Open Access Publishing Agreement](#)

1. Introduction

Optical conversion in parametric oscillators (OPO) and amplifiers (OPA) is a versatile and common method for tunable coherent sources [1]. Nonlinear conversion is of particular interest for the middle infrared (mid-IR) part of the spectrum, where the availability of other solid-state coherent sources is limited to quantum cascade lasers [2,3] and lasers based on chalcogenides doped with transition metals [4]. Zinc germanium phosphide (ZGP) crystals have favorable properties [5,6] among nonlinear materials suitable for conversion to mid-IR with pumping near 2 μm, where a wide choice of high power pump lasers with excellent beam quality is available. The ZGP is particularly appropriate for high-power and high-energy applications due to its thermal and mechanical properties. Recently, significant progress in growth techniques allowed reduction of residual pump absorption at 2 μm down to 0.02 cm⁻¹ and an increase of a laser-induced damage threshold for ns-pulses to 4 – 5 J/cm² [6–13]. A demand for such laser sources stems from areas like remote sensing, free space communication or countermeasures in defense. Many of these applications require high-average power sources with good beam quality, hence power up-scaling has been investigated over many years and remains challenging [14–18].

To date, among high-power mid-IR ZGP OPO demonstrations, many suffer from limited stability and beam quality. The highest average power demonstrated in single-stage ZGP OPO reached 110 W [19], but beam quality at 100 W was poor, that is $M^2 \approx 9$, and the operation at maximum output power lasted only for a few seconds before crystal damage, at the level of 30 W, authors reported $M^2 \approx 4$. The most recent stable high-repetition-rate source is two-stage OPO-OPA tandem pumped by a 10 kHz Ho:YAG [20]. In this case, the first stage ZGP OPO

yielded 28.4 W ($M^2 = 2.1$), while the OPA stage had $M^2 \approx 3$ at an output power of 102 W. All aforementioned experiments utilized 4-mirrors planar ring resonators. In a similar cavity arrangement but with two separate ZGP crystals placed in series 41 W with $M^2 = 4.4$ was reported [21]. Other demonstrations of stable single-stage ZGP OPO include 27 W ($M^2 = 4$) with two ZGPs in a linear cavity [22] and 22 W with $M^2 = 1.4$ in 3-mirror V-shaped planar ring resonator [23].

There are two dominant effects causing deterioration of the beam quality in high-power ZGP OPOs. These are thermal lensing [24] and gain guiding [25,26]. The latter arises from a spatial intensity distribution of pump pulse energy, and thus gain distribution. It only depends on pulse energy, but not on the average power of the pump. On one hand, this can be minimized by increasing the pump spot size in the crystal, but on the other hand, the greater the pump spot size, the higher is the threshold and more difficult to maintain good beam quality [15]. Unlike the gain guiding, the thermal lens effect depends on heat absorbed by the crystal, so it is proportional to the pump repetition frequency. One way to counter the thermal lens is direct compensation with intracavity negative lens [18] or a Galilean telescope [27]. This approach was also proven to be effective in the demonstration of the OPO-OPA 102 W system [20]. The compensation with elements of fixed dioptric strengths is limited to systems of well-characterized and known thermal lens, but very often its dynamic nature is not studied carefully.

Another well-established technique to improve beam quality in OPOs is a ring resonator with a non-planar configuration of mirrors. Such resonators and their effect on beam quality improvement were first investigated by Smith *et al.* [28]. A specific non-planar design with 90° image-rotation is known as a Rotated Image Singly-Resonant Twisted RectAngle (RISTRA) cavity [29]. The RISTRA as an OPO resonator was proven to be effective and advantageous compared to planar resonators in many later demonstrations of high-power and high-energy OPOs with improved beam quality [30,31]. In this study, we take advantage of this particular cavity design and its properties to focus on different factors affecting beam quality.

Within the technical limits of the experimental setup, a given OPO output power can be realized by a high pump pulse repetition rate and a low pump pulse energy or vice versa. The question is which combination yields the better beam quality.

Here, we demonstrate experimental verification of beam quality improvement using single-stage ZGP OPO in the RISTRA cavity pumped by a high-repetition rate Ho:LLF MOPA system. We experimentally investigate changes of the beam quality with pulse energy and repetition rate of the pump. The beam quality factor M^2 as a function of the repetition rate at constant pulse energy shows an unexpected minimum, which we support by numerical simulations. For the first time, we demonstrate time-resolved experimental studies of a steady-state thermal lens build-up process.

2. Experimental setup

2.1. Highly-efficient resonantly pumped Q-switched Ho:LLF MOPA system

A Ho:LuLiF₄ (Ho:LLF) MOPA system [32] serves as a pump laser, its schematic diagram is shown in Fig. 1. The unpolarized pump light of a 120 W Tm fiber laser (IPG TLR-120-WC-Y14) passes through a first telescope (L1: $f = 75$ mm; L2: $f = -40$ mm) and then is split into two orthogonally polarized pump beams passing each a second telescope (L3: $f = -75$ mm; L4: $f = 100$ mm; L5: $f = -200$ mm). The size of the pump image in the crystals can be simply adjusted by moving lenses L3 and L4 of the second telescope [33].

The 0.5 at. % doped a-cut Ho:LLF crystals have diameters of 6 mm. The c-axis of the 60 mm long oscillator and the two amplifier crystals (40 and 60 mm long) are oriented parallel to the polarization of the pump beams to take advantage of the high absorption on π -polarization of Ho:LLF at 1940 nm. The folded resonator is 130 mm long with a concave output coupler (OC) with a radius of curvature 300 mm and reflectivity of 60 %, a flat high-reflector (HR), and two

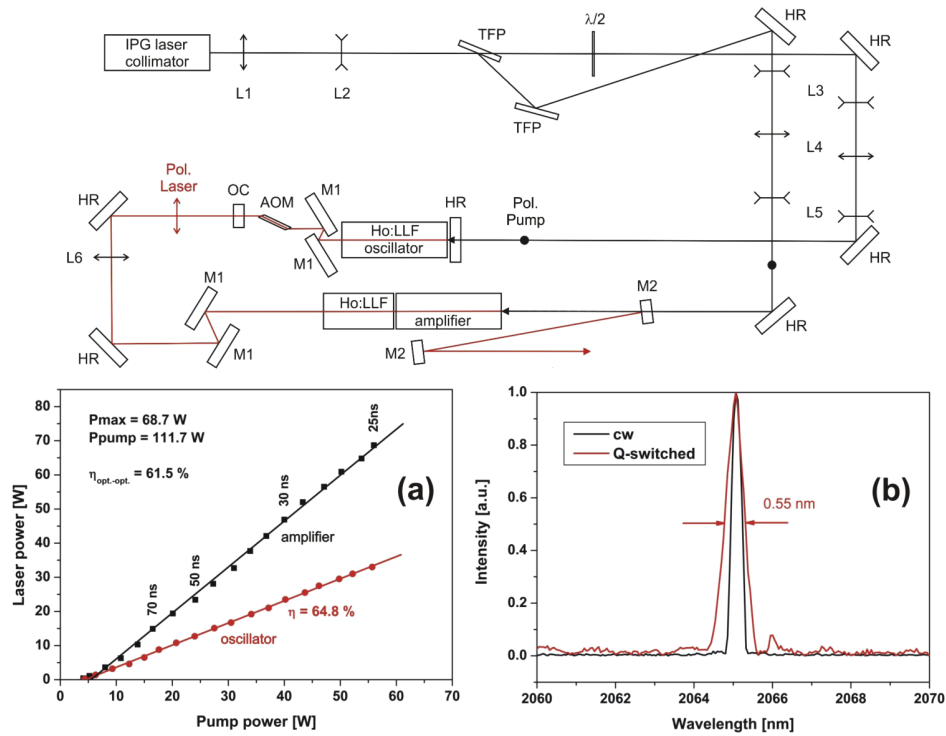


Fig. 1. Setup of the end-pumped Ho:LLF MOPA system; TFP: thin-film polarizer, $\lambda/2$: half-wave plate, HR: high reflector. The graphs below: Laser power with labels indicating pulse duration (a) and spectral output (b) of the Ho:LLF MOPA system.

flat mirrors M1 tilted by 32° , with high transmission at the pump and high reflection at the laser wavelengths. A 17 mm Brewster-cut acousto-optic modulator (AOM) (Gooch & Housego model QS041-4M(BR)-IS3) was used for Q-switched operation with a repetition rate of 10 kHz. Radio-frequency power was 20 W at 41 MHz. The AOM forces oscillation on σ -polarization and amplification is done on σ -polarization, too. The middle of the oscillator crystal is imaged 1 to 1 to the center of the composite amplifier crystal with lens L6 ($f = 150 \text{ mm}$).

The graphs in Fig. 1 show average laser power (a) and spectral output (b) of the system. It delivers 68.7 W at 2065 nm in TEM₀₀ operation at a repetition rate of 10 kHz with an optical-to-optical efficiency of 61.5 %. The second telescope was adjusted to obtain temporally stable pulses. Afterward, a pump spot diameter of 609 μm was measured. The output beam quality is diffraction-limited at a maximum pulse energy of 6.87 mJ.

2.2. ZGP OPO experimental setup

The experimental setup of the ZGP OPO is presented in Fig. 2. The 300 mm lens focuses the output from Ho:LLF onto the ZGP crystal with a measured spot diameter of 1.1 mm. The spot size was chosen not to exceed the damage threshold of the ZGP ($< 1 \text{ J/cm}^2$). A half-wave plate in combination with a polarizer allows polarization rotation and, by this means, pulse energy and power adjustment without changes in spatial and temporal pulse properties. A Pockels cell allows voltage-controlled polarization rotation for power adjustment and pulse picking. We can set the pump repetition rate to the values: 0.1 kHz, 0.5 kHz, 1 kHz, 2.5 kHz, 5 kHz, and 10 kHz without affecting pulse properties. Behind the cavity, the depleted pump is filtered out by a

dichroic mirror. A wedge is used to reflect a small portion of the OPO beams for M^2 -analysis. It is carried out with $f = 500$ mm focusing lens. The respective power of the beams is monitored with water-cooled thermal sensors (mks Ophir L250W).

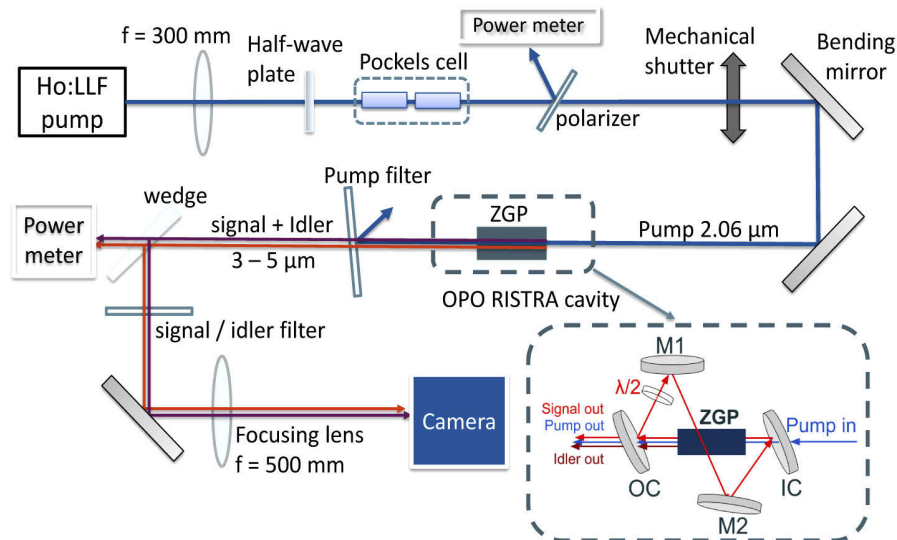


Fig. 2. The experimental setup with a mirror configuration of the RISTRA OPO cavity used in this study.

Brightness determination was done by inspection of the signal and idler beams with infrared pyroelectric array sensor (mks Ophir Pyrocam IV Beam Profiling Camera) using the test method for laser beam parameters: beam widths, divergence angle, and beam propagation factor M^2 (EN ISO 11146). The camera resolution is 320×320 pixels with the pixel pitch $80 \mu\text{m}$. This camera was used in chopped (50 Hz) or triggered (100 Hz) modes for all the beam images presented here. The 50 Hz frame rate offers 20 ms time resolution for the acquisition of beam images. The mechanical, remotely controlled beam shutter allows the pump beam blocking before the OPO cavity.

The ZGP crystal used in this study has an aperture of $6 \times 6 \text{ mm}^2$ and a length of 20 mm, it is cut at 55° with respect to the optical axis for type-I phase matching at $2 \mu\text{m}$, its end faces are AR-coated for the pump and $3 - 5 \mu\text{m}$ (Harbin Huigong Science & Technology Co., Ltd.). We determined its absorption coefficient by measuring absorptance $\alpha = 0.044 \text{ cm}^{-1}$ at $2.065 \mu\text{m}$. It is transversely centered on the pump beam and adjusted in a phase-matching angle for maximum OPO output pulse energy, resulting in a signal wavelength around $3.85 \mu\text{m}$ and an idler around $4.45 \mu\text{m}$. The crystal is wrapped in indium foil and mounted inside the optical cavity in a copper holder, serving as a heat sink. The crystal holder was not water-cooled.

The singly signal resonant RISTRA cavity is composed of four flat mirrors in a non-planar ring configuration. The output coupler (OC) of the RISTRA is partially reflective for the signal beam ($R \approx 50\%$) and highly transmitting ($T > 95\%$) for the pump and the idler. The input coupling mirror (IC) and the two other mirrors (M1, M2) are identical and have high transmission for the pump ($T = 86.3\%$) and the idler ($T > 94\%$), and high reflectivity for the signal ($R > 99\%$). The uncoated, zero-order MgF_2 half-wave plate compensates for polarization rotations in the resonator and keeps it unchanged after a round trip. The physical length of the resonator is 130 mm, which corresponds to the optical path of the signal beam per round trip around 172 mm.

3. Results and discussion

3.1. Beam quality at a constant repetition rate of 10 kHz

The beam quality factor M^2 of the OPO signal and idler beams as a function of the pump pulse energy at a constant repetition rate of 10 kHz is shown in Fig. 3 (upper left). It is nearly diffraction-limited near threshold at pump energy of 1 mJ and increases to a value of $M^2 \sim 1.8$ at maximum pump pulse energy of 6 mJ (60 W). The inset depicts corresponding conversion efficiency and the OPO output pulse energy and power. The graphs on the right in Fig. 3 show the change of the focused signal beam between the highest (top) and the lowest (bottom) laser power after a positive 500 mm focal length CaF₂ lens. The beam quality factors were determined by fitting the standard Gaussian beam propagation expression to the measured data. A shift of the waist position of around 2.5 cm is visible. The rows of images in the bottom are the near-field beam images taken at the position 80 cm after the focusing lens. Higher-order modes contribute to beam profiles, which is the result of a decrease in the fundamental mode size of the signal. Because the idler beam has a much larger divergence than the signal beam, it was clipped by the 1-inch optics. The M^2 measurement at the highest power could not be performed, that is the reason for a lack of the last 3 data points for the idler in the graph. There is no reason for a deviation from the trend, thus similar behavior can be anticipated.

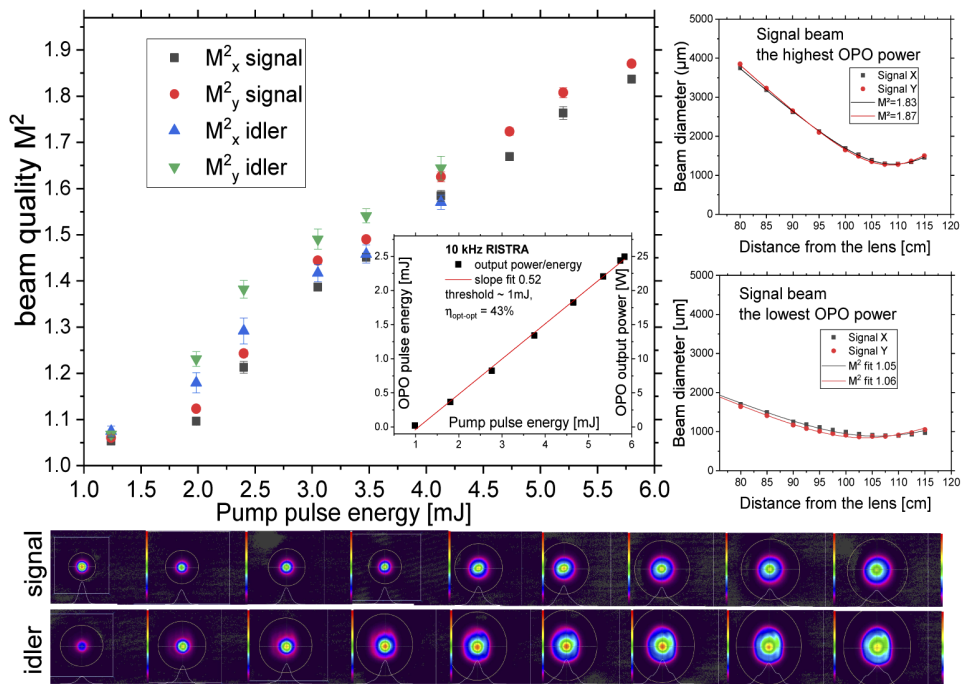


Fig. 3. The main graph shows how the beam quality factor scales with the pump pulse energy at a fixed repetition rate of 10 kHz. The inset shows the conversion efficiency with output pulse energy associated with the left axis and total output power with the right axis. Below are near-field beam images (taken 80 cm after the focusing lens) corresponding to each data point. The graphs on the right-hand-side show signal beam focusing behavior as measured for two extreme pump power levels.

3.2. Calculation of the fundamental mode size

Since all the cavity mirrors are flat, the question remains, what makes it stable? On one hand, a portion of the pump radiation is converted into heat inside the crystal and forms a positive thermal lens. As depicted in Fig. 4(a), the signal fundamental mode beam radius w decreases with increasing thermal lens (n_2 parameter) which makes the resonator stable. Calculations are done with laser cavity analysis and design software (LAS-CAD GmbH, <http://www.las-cad.com>). From the relation between the real spot size of a laser beam, which in our case is the pump spot size w_{pump} , and its corresponding fundamental mode spot size w , the $M^2 = (w_{pump}/w)^2$ [34] increases with increasing thermal lens. At increasing values of n_2 , the resonator approaches its stability limit and the fundamental mode spot size increases again, resulting in a decrease of M^2 value. On the other hand, a quadratic variation of the gain parameter $\alpha(r) = \alpha_0 - \frac{1}{2}\alpha_2 r^2$ makes the cavity stable too, its influence on the fundamental mode signal beam size and expected M^2 value is shown in Fig. 4(b). The parametric gain coefficient α can be found e.g. in [18].

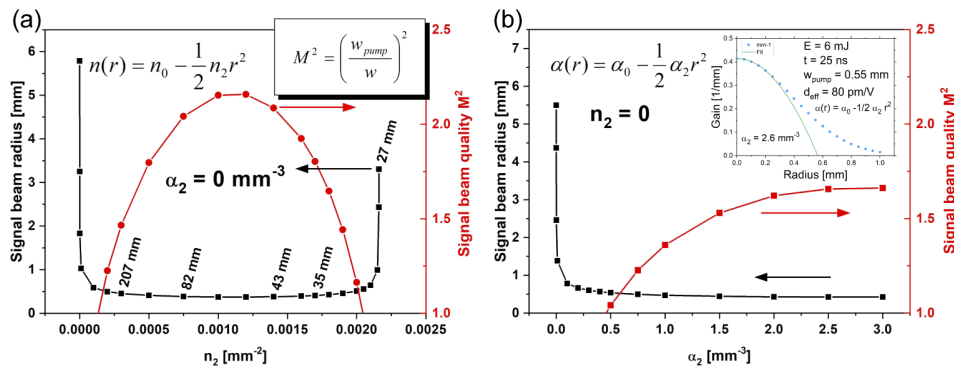


Fig. 4. Calculation of the fundamental mode signal radius w and corresponding expected M^2 value as a function of (a) the quadratically varying index of refraction parameter n_2 and (b) the quadratically varying gain parameter α_2 . In (a), respective focal lengths of the thermal lens are displayed on the radius curve.

Taking into account a Gaussian intensity distribution with pump spot radius $w_{pump} = 0.55 \text{ mm}$, pump pulse energy $E = 6 \text{ mJ}$, pulse duration $t = 25 \text{ ns}$ (FWHM), and an effective nonlinear coefficient $d_{eff} = 80 \text{ pm/V}$, the calculated gain distribution is shown in the inset of Fig. 4(b). By curve fitting, the quadratic gain parameter α_2 turns out to be 2.6 mm^{-3} . This simple calculation shows that gain guiding can make the signal beam narrower than the pump beam, increasing the M^2 . Therefore, both effects of thermal lensing and gain guiding lead to deterioration of the beam quality. To discriminate between them, we investigated the beam quality as a function of the repetition rate.

3.3. Evolution of beam quality with pump repetition rate

We controlled the repetition rate of the pump by pulse picking without affecting pulse properties. This way, we isolated the influence of the repetition frequency from other factors affecting beam quality. Figure 5(a) shows the results of the measurement of the beam quality factor as a function of the repetition rate of the pump. The pulse energy was kept at 6 mJ and other pulse properties were not changed between measurements. At the maximum rate of 10 kHz, corresponding to the maximum output power of 25 W in our setup, we measured $M^2 = 1.8$ (Fig. 5(b)). As one could expect when lowering the repetition rate, the beam quality should improve as it does when the pulse energy is lowered. However, the actual behavior deviates from expected. The M^2 data show a minimum value of 1.2 at 1 kHz, starting from 1.3 at a low repetition rate of 0.1 kHz and

rising to 1.8 at 10 kHz. The observed minimum suggests a trade-off between the thermal lens and the gain guiding, as in this case only the thermal lens is varied while the gain is fixed. It is different from the behavior observed previously when both pulse energy (gain) and thermal lens (average pump power) were varied.

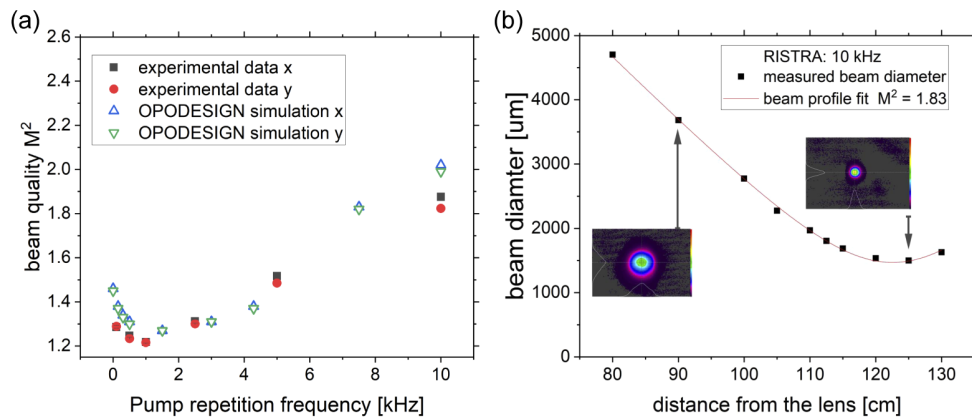


Fig. 5. (a) Evolution of beam quality with the pump repetition rate for RISTRA cavity at constant pump pulse energy of 6 mJ and (b) an example of the caustic registered to retrieve M^2 for signal beam corresponding to the maximum output power at 10 kHz.

The results of numerical simulations confirm the experimental data. The simulation tool OPODESIGN [18] solves the paraxial wave equations with fast Fourier transform and it propagates the signal, idler, and pump waves in the crystal, cavity, and outside to establish the caustic. The split-step method is applied to integrate the OPO equations, thus conversion and back conversion are accounted for. The simulation uses only single frequencies for all waves. The temporal evolution is realized by sampling slices of round-trip time in the cavity. At low repetition rate, the thermal lens is weak and the beam quality is dominantly governed by the gain guiding effect at the pump pulse energy of 6 mJ. When the repetition rate rises, the thermal lens gets stronger, causing the weakening of the gain guiding and slight improvement of the beam quality. Simulations with OPODESIGN indicate that this trend to better beam quality cannot be ascribed to an obvious change of a single parameter like, for instance, the diameter of the signal in the crystal. A further rise of the repetition rate makes the thermal lens stronger and stronger, thus causing a growing destabilizing effect on the OPO cavity. The beam quality factor leaves its minimum and rises again.

The effect of the pump repetition rate in such an OPO system has not been studied before. In [30] authors used the RISTRA and monitored conversion efficiency 1 – 500 Hz range, however they tuned Q-switching, thus varying the pump pulse duration along with the repetition frequency.

3.4. Time-resolved studies of a steady-state thermal lens

The transient evolution of beam quality correlates with a build-up of temperature gradient inside the crystal. Such a gradient leads to a steady-state thermal lens. To understand the process, we monitored the M^2 as a function of time after opening the pump with a mechanical shutter. The procedure to reconstruct the beam quality as a time function is as follows. The beam profiles at a certain position of the camera are captured with a 20 ms resolution. Then, the camera is moved to the next position along the signal beam, while the crystal is allowed to cool down and come back to the initial equilibrium conditions. The intervals required for this were determined experimentally. After data is collected for enough points to plot caustics, we retrieve the time evolution of the beam quality factor in post-processing by combining the profiles for the same

time frame. The result of such procedure is shown in Fig. 6 over 8 s after the pump was unblocked. The inset graph shows an example of the build-up of temperature in the ZGP center calculated numerically by solving heat transport equations.

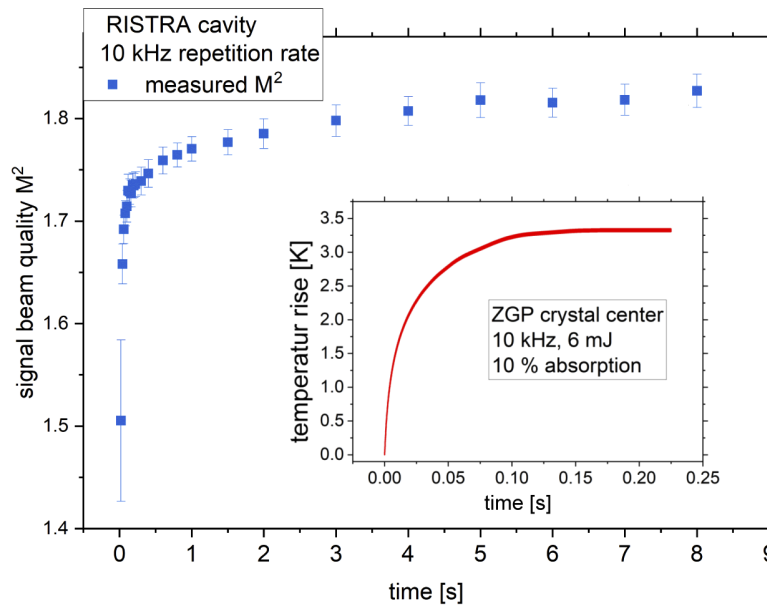


Fig. 6. The evolution of the beam quality factor M^2 for the RISTRA cavity registered with 20 ms time resolution (not all the points are plotted). The inset graph shows the numerical simulation of temperature evolution in the crystal center.

What we notice about the M^2 time dependency are two timescales of this process. The fast exponential growth is related to the steady-state thermal lens build-up with a time constant in a good agreement with a value calculated from heat diffusion equations for the steady-state thermal lens [35]. After this, we observe a drift in the M^2 -value, which can be likely attributed to heat accumulation and a rise in the overall temperature of the crystal and its holder. The heat accumulation leads to a slow change of the boundary conditions for a temperature profile inside the crystal, thus a change in the shape of the thermal lens. As a consequence, we can see higher-order modes appearing as explained before. The beam shape during the evolution changes similarly to the dependency observed for pump pulse energy (compare Fig. 3). The slow drift in the M^2 -value depends only on water cooling of the crystal holder, as its constant temperature ensures constant boundary conditions for the transient thermal lens [36].

4. Conclusions

In this paper, we investigated how the beam quality in a single-stage ZGP OPO changes under varying pumping conditions to determine the best parameters to further up-scale the output power while maintaining good beam quality. The maximum total output power in the mid-IR region between 3 and 5 μm from our system was 25 W with $M^2 = 1.8$ and it is only pump-power limited. The variation of M^2 with pump repetition rate is a manifestation of a trade-off between the thermal lens and gain guiding. To our knowledge, the effect of the pump repetition rate on M^2 has not been considered earlier. Our investigation revealed conditions for optimal beam quality. We supported our findings by numerical simulations of OPO pulse propagation relevant to our experimental conditions.

We also presented results of the time-resolved beam quality factor monitoring in our setup with the 20-ms resolution revealing the steady-state thermal lens build-up. Such studies provide new information about ZGP OPOs, being usually masked in other high-power experiments, where beam quality measurements show only the system performance at stationary conditions in equilibrium. The knowledge of dynamic behavior is useful when designing and optimizing the duty cycle for a particular application, e.g. the ability to focus the laser output over long ranges can be enhanced by appropriate timing control.

Funding. Direction Générale de l'Armement.

Acknowledgments. Portions of this work were presented at the *OSA Laser Congress* in 2019 [32], the *OSA Laser Congress* in 2020 [37], and the *9th EPS-QEOD Europhoton Conference on Solid-State, Fibre, and Waveguide Coherent Light Sources* in 2020 [38].

Disclosures. The authors declare no conflicts of interest.

References

1. M. H. Dunn and M. Ebrahimzadeh, "Parametric generation of tunable light from continuous-wave to femtosecond pulses," *Science* **286**(5444), 1513–1517 (1999).
2. J. Faist, F. Capasso, C. Sirtori, D. L. Sivco, J. N. Baillargeon, A. L. Hutchinson, S.-N. G. Chu, and A. Y. Cho, "High power mid-infrared ($\lambda \sim 5\mu\text{m}$) quantum cascade lasers operating above room temperature," *Appl. Phys. Lett.* **68**(26), 3680–3682 (1996).
3. Y. Yao, A. J. Hoffman, and C. F. Gmachl, "Mid-infrared quantum cascade lasers," *Nat. Photonics* **6**(7), 432–439 (2012).
4. S. B. Mirov, I. S. Moskalev, S. Vasilyev, V. Smolski, V. V. Fedorov, D. Martyshkin, J. Peppers, M. Mirov, A. Dergachev, and V. Gapontsev, "Frontiers of mid-IR lasers based on transition metal doped chalcogenides," *IEEE J. Sel. Top. Quantum Electron.* **24**(5), 1–29 (2018).
5. G. Boyd, E. Buehler, F. Storz, and J. Wernick, "Linear and nonlinear optical properties of ternary $A^II B^IV C_2^V$ chalcopyrite semiconductors," *IEEE J. Quantum Electron.* **8**(4), 419–426 (1972).
6. P. G. Schunemann, K. T. Zawilski, L. A. Pomeranz, D. J. Creeden, and P. A. Budni, "Advances in nonlinear optical crystals for mid-infrared coherent sources," *J. Opt. Soc. Am. B* **33**(11), D36–D43 (2016).
7. R. D. Peterson, K. L. Schepler, J. L. Brown, and P. G. Schunemann, "Damage properties of ZnGeP₂ at 2 μm ," *J. Opt. Soc. Am. B* **12**(11), 2142–2146 (1995).
8. G. Verozubova, A. Okunev, A. Gribenyukov, A. Trofimiv, E. Trukhanov, and A. Kolesnikov, "Growth and defect structure of ZnGeP₂ crystals," *J. Cryst. Growth* **312**(8), 1122–1126 (2010).
9. K. T. Zawilski, S. D. Setzler, P. G. Schunemann, and T. M. Pollak, "Increasing the laser-induced damage threshold of single-crystal ZnGeP₂," *J. Opt. Soc. Am. B* **23**(11), 2310–2316 (2006).
10. L. Wang, T. Xing, S. Hu, X. Wu, H. Wu, J. Wang, and H. Jiang, "Mid-infrared ZGP-OPO with a high optical-to-optical conversion efficiency of 75.7%," *Opt. Express* **25**(4), 3373–3380 (2017).
11. Z. Lei, C. Zhu, C. Xu, B. Yao, and C. Yang, "Growth of crack-free ZnGeP₂ large single crystals for high-power mid-infrared OPO applications," *J. Cryst. Growth* **389**, 23–29 (2014).
12. C. Huang, H. Wu, R. Xiao, S. Chen, and J. Ma, "High-pressure-assisted synthesis of high-volume ZnGeP₂ polycrystalline," *J. Cryst. Growth* **492**, 24–28 (2018).
13. S. Mi, Y. Chen, G. Liu, K. Yang, B. Yao, D. Tongyu, and X. Duan, "Measurement of optical homogeneity of ZnGeP₂ crystal using a 2.02 μm single-longitudinal-mode Tm:LuAG ring laser," *Appl. Opt.* **59**(19), 5864–5869 (2020).
14. G. Arisholm, Ø. Nordseth, and G. Rustad, "Optical parametric master oscillator and power amplifier for efficient conversion of high-energy pulses with high beam quality," *Opt. Express* **12**(18), 4189–4197 (2004).
15. G. Arisholm, R. Paschotta, and T. Südmeyer, "Limits to the power scalability of high-gain optical parametric amplifiers," *J. Opt. Soc. Am. B* **21**(3), 578–590 (2004).
16. Ø. Farsund, G. Arisholm, and G. Rustad, "Improved beam quality from a high energy optical parametric oscillator using crystals with orthogonal critical planes," *Opt. Express* **18**(9), 9229–9235 (2010).
17. G. Rustad, G. Arisholm, and Ø. Farsund, "Effect of idler absorption in pulsed optical parametric oscillators," *Opt. Express* **19**(3), 2815–2830 (2011).
18. M. Schellhorn, G. Spindler, and M. Eichhorn, "Improvement of the beam quality of a high-pulse-energy mid-infrared fractional-image-rotation-enhancement ZnGeP₂ optical parametric oscillator," *Opt. Lett.* **42**(6), 1185–1188 (2017).
19. B.-R. Zhao, B.-Q. Yao, C.-P. Qian, G.-Y. Liu, Y. Chen, R.-X. Wang, T.-Y. Dai, and X.-M. Duan, "231 W dual-end-pumped Ho:YAG MOPA system and its application to a mid-infrared ZGP OPO," *Opt. Lett.* **43**(24), 5989–5992 (2018).
20. C.-P. Qian, B.-Q. Yao, B.-R. Zhao, G.-Y. Liu, X.-M. Duan, T.-Y. Dai, Y.-L. Ju, and Y.-Z. Wang, "High repetition rate 102 W middle infrared ZnGeP₂ master oscillator power amplifier system with thermal lens compensation," *Opt. Lett.* **44**(3), 715–718 (2019).
21. B.-Q. Yao, Y.-J. Shen, X.-M. Duan, T.-Y. Dai, Y.-L. Ju, and Y.-Z. Wang, "A 41-W ZnGeP₂ optical parametric oscillator pumped by a Q-switched Ho:YAG laser," *Opt. Lett.* **39**(23), 6589–6592 (2014).

22. A. Hemming, J. Richards, A. Davidson, N. Carmody, S. Bennetts, N. Simakov, and J. Haub, "99 W mid-IR operation of a ZGP OPO at 25% duty cycle," *Opt. Express* **21**(8), 10062–10069 (2013).
23. E. Lippert, H. Fonnum, G. Arisholm, and K. Stenersen, "A 22-watt mid-infrared optical parametric oscillator with V-shaped 3-mirror ring resonator," *Opt. Express* **18**(25), 26475–26483 (2010).
24. J. P. Gordon, R. C. C. Leite, R. S. Moore, S. P. S. Porto, and J. R. Whinnery, "Long-transient effects in lasers with inserted liquid samples," *J. Appl. Phys.* **36**(1), 3–8 (1965).
25. F. Salin and J. Squier, "Gain guiding in solid-state lasers," *Opt. Lett.* **17**(19), 1352–1354 (1992).
26. G. Arisholm, R. Paschotta, and T. Südmeyer, "Limits to the power scalability of high-gain optical parametric amplifiers," *J. Opt. Soc. Am. B* **21**(3), 578–590 (2004).
27. M. Schellhorn, G. Spindler, and M. Eichhorn, "Mid-infrared ZGP OPO with divergence compensation and high beam quality," *Opt. Express* **26**(2), 1402–1410 (2018).
28. A. V. Smith and M. S. Bowers, "Image-rotating cavity designs for improved beam quality in nanosecond optical parametric oscillators," *J. Opt. Soc. Am. B* **18**(5), 706–713 (2001).
29. A. V. Smith and D. J. Armstrong, "Nanosecond optical parametric oscillator with 90° image rotation: design and performance," *J. Opt. Soc. Am. B* **19**(8), 1801–1814 (2002).
30. A. Dergachev, D. Armstrong, A. Smith, T. Drake, and M. Dubois, "3.4- μm ZGP RISTRA nanosecond optical parametric oscillator pumped by a 2.05- μm Ho:YLF MOPA system," *Opt. Express* **15**(22), 14404–14413 (2007).
31. G. Marchev, M. Reza, V. Badikov, A. Esteban-Martin, G. Stöppler, M. Starikova, D. Badikov, V. Panyutin, M. Eichhorn, G. Shevyrdyaeva, A. Tyazhev, S. Sheina, A. Agnesi, A. Fintisova, and V. Petrov, "Mid-infrared rotated image singly resonant twisted rectangle optical parametric oscillator based on HgGa₂S₄ pumped at 1064 nm," *Appl. Opt.* **53**(33), 7951–7962 (2014).
32. M. Schellhorn and G. Spindler, "High-Efficient Resonantly Pumped Q-Switched Ho:LLF MOPA System," in *Laser Congress 2019 (ASSL, LAC, LS&C)*, (Optical Society of America, 2019), p. JTh3A.18.
33. P. Krötz, "On high-energy, high-stability and short-pulse Ho:YLF regenerative amplifiers," Ph.D. thesis, Universität Hamburg (2017).
34. S. Bigotta, G. Stöppler, J. Schöner, M. Schellhorn, and M. Eichhorn, "Novel non-planar ring cavity for enhanced beam quality in high-pulse-energy optical parametric oscillators," *Opt. Mater. Express* **4**(3), 411–423 (2014).
35. W. Koechner, "Transient thermal profile in optically pumped laser rods," *J. Appl. Phys.* **44**(7), 3162–3170 (1973).
36. J. E. Tucker, C. L. Marquardt, S. R. Bowman, and B. J. Feldman, "Transient thermal lens in a ZnGeP₂ crystal," *Appl. Opt.* **34**(15), 2678–2682 (1995).
37. M. Piotrowski, M. A. Medina, G. Spindler, M. Schellhorn, and A. Hildenbrand-Dhollande, "Beam quality enhancement in high power mid-IR ZGP OPO sources: a focus on thermal lens build-up," in *Laser Congress 2020 (ASSL, LAC)*, (Optical Society of America, 2020), p. JTh2A.8.
38. M. Piotrowski, M. A. Medina, M. Schellhorn, and A. Hildenbrand-Dhollande, "Temporally resolved studies of thermal effects in high power ZGP OPO pumped by high-repetition Ho:LLF MOPA system," *EPJ Web Conf.* **243**, 18001 (2020).

References

- [1] T. H. Maiman. Stimulated Optical Radiation in Ruby. *Nature*, 187(4736):493–494, August 1960.
- [2] J. A. Giordmaine and R. C. Miller. Tunable coherent parametric oscillation in $LiNbO_3$ at optical frequencies. *Phy. Rev. Lett.*, 14:973, 1965.
- [3] <https://hitran.iao.ru/>.
- [4] Konstantin L. Vodopyanov. In *Laser-based mid-infrared sources and applications*, chapter 3. John Wiley & Sons, Inc., 2020.
- [5] S. Mirov, I. Moskalev, S. Vasilyev, V. Smolski, V. Federov, D. Martyshkin, J. Peppers, M. Mirov, A. Dergachev, and V. Gapontsev. Frontiers of mid-IR lasers based on transition metal doped chalcogenides. *IEEE J. Sel. Top. Quantum Electronics*, 24:1–29, 2018.
- [6] S. Vasilyev, I. Moskalev, M. Mirov, S. Mirov, and V. Gapontsev. Multi-Watt mid-IR femtosecond polycrystalline Cr^{2+} :ZnS and Cr^{2+} :ZnSe laser amplifiers with the spectrum spanning 2.0-2.6 μ m. *Opt. Express*, 24(2):1616–1623, Jan 2016.
- [7] V. A. Akimov, V. I. Kozlovskii, Y. V. Korostelin, A. I. Landman, Y. P. Podmar'kov, Y. K. Skasyrskii, and M. P. Frolov. Efficient Cr^{2+} :CdSe laser continuously tunable in the spectral range from 2.26 to 3.61 μ m. *Quantum Electronics*, 38(3):205–208, 2008.
- [8] M. Razeghi, Q. Y. Lu, N. Bandyopadhyay, W. Zhou, D. Heydari, Y. Bai, and S. Slivken. Quantum cascade lasers: from tool to product. *Opt. Express*, 23(7):8462–8475, Apr 2015.
- [9] Y. Bai, N. Bandyopadhyay, S. Tao, S. Slivken, and M. Razeghi. Room temperature quantum cascade lasers with 27 % wall plug efficiency. *Appl. Phys. Lett.*, 98, 2011.
- [10] Q. Lu, S. Slivken, D. Wu, and M. Razeghi. High power continuous wave operation of single mode quantum cascade lasers up to 5 W spanning $\lambda \sim 3.8 - 8.3 \mu$ m. *Opt. Express*, 28(10):15181–15188, May 2020.

- [11] F. Wang, S. Slivken, D. H. Wu, Q. Y. Lu, and M. Razeghi. Continuous wave quantum cascade lasers with 5.6 W output power at room temperature and 41% wall-plug efficiency in cryogenic operation. *AIP Advances*, 10(5):055120, 2020.
- [12] S. Das. Optical parametric oscillator: status of tunable radiation in mid-IR to IR spectral range based on ZnGeP₂ crystal pumped by solid state lasers. *Optical and Quantum Electronics*, 51(3):70, 2019.
- [13] J. A. Armstrong, N. Bloembergen, J. Ducuing, and P. S. Pershan. Interactions between light waves in a nonlinear dielectric. *Phy. Rev.*, 127:1918, 1962.
- [14] N. M. Kroll. Parametric amplification in spatially extended media and application to the design of tunable oscillators at optical frequencies. *Phy. Rev.*, 127:1027, 1962.
- [15] V. Petrov. Frequency down-conversion of solid-state laser sources to the mid-infrared spectral range using non-oxide nonlinear crystals. *Progress in Quantum Electronics*, 42:1 – 106, 2015.
- [16] <https://www.webofscience.com/>.
- [17] C. F. O'Donnell, S. C. Kumar, P. G. Schunemann, and M. Ebrahim-Zadeh. Femtosecond optical parametric oscillator continuously tunable across 3.6-8 μm based on orientation-patterned gallium phosphide. *Opt. Lett.*, 44(18):4570–4573, Sep 2019.
- [18] M. S. Webb, P. F. Moulton, J. J. Kasinski, R. L. Burnham, G. Loiacono, and R. Stolzenberger. High-average-power KTiOAsO₄ optical parametric oscillator. *Opt. Lett.*, 23(15):1161–1163, Aug 1998.
- [19] L.A. Gloster, I. T. McKinnie, Z. X. Jiang, T. A. King, J. M. Boon-Engering, W. E. Van der Veer, and W. Hogervorst. Narrow-band $\beta\text{-BaB}_2\text{O}_4$ optical parametric oscillator in a grazing-incidence configuration. *J. Opt. Soc. Am. B*, 12(11):2117, 1995.
- [20] W. R. Bosenberg, A. Drobshoff, J. I. Alexander, L. E. Myers, and R. Byer. 93% pump depletion, 3.5-W continuous-wave, singly resonant optical parametric oscillator. *Opt. Letters*, 21(17):1336, 1996.
- [21] P. G. Schunemann, K. T. Zawilski, L. A. Pomeranz, D. J. Creeden, and P. A. Budni. Advances in nonlinear optical crystals for mid-infrared coherent sources. *J. Opt. Soc. Am. B*, 33(11):D36–D43, November 2016.
- [22] V. Petrov, F. Noack, I. Tunchev, P. Schunemann, and K. Zawilski. The nonlinear coefficient d_{36} of CdSiP₂. *Proc. SPIE*, 7197:91970M, 2009.

- [23] P. G. Schunemann, L. A. Pomeranz, Y. E. Young, L. Mohnkern, and A. Vera. Recent advances in all-epitaxial growth and properties of orientation-patterned gallium arsenide (OP-GaAs). In *2009 Conference on Lasers and Electro-Optics and 2009 Conference on Quantum electronics and Laser Science Conference*. Optical Society of America, 2009. paper CWJ5.
- [24] B. Cole, L. Goldberg, S. Chinn, L. A. Pomeranz, K. T. Zawilski, P. G. Schunemann, and J. McCarthy. Compact and efficient mid-IR OPO source pumped by a passively Q-switched Tm:YAP laser. *Opt. Letters*, 43(5):1099, 2018.
- [25] D. Creeden, L. A. Pomeranz, C. Jones, B. R. Johnson, P. A. Ketteridge, M. Lemons, C. Ibach, P. A. Budni, K. T. Zawilski, P. G. Schunemann, and S. D Setzler. High power mid-infrared laser sources. In *Conference on Laser and Electro-Optics*. Optical Society of America, 2016. paper ATh3K.1.
- [26] J. Wueppen, S. Nyga, B. Jungbluth, and D. Hoffman. 1.95 μm -pumped OP-GaAs optical parametric oscillator with 10.6 μm idler wavelength. *Opt. Letters*, 41(18):4225–4228, 2016.
- [27] A. Hildenbrand, C. Kieleck, E. Lallier, D. Faye, A. Grisard, B. Gérard, and M. Eichhorn. Compact efficient mid-infrared laser source: OP-GaAs OPO pumped by Ho^{3+} :YAG laser. In David H. Titterton and Mark A. Richardson, editors, *Technologies for Optical Countermeasures VIII*, volume 8187, pages 86 – 91. International Society for Optics and Photonics, SPIE, 2011.
- [28] G. A. Verozubova, A. O. Okunev, A. I. Gribenyukov, A. Y. Trofimiv, E. M. Trukhanov, and A. V. Kolesnikov. Growth and defect structure of ZnGeP_2 crystals. *Journal of Crystal Growth*, 312(8):1122–1126, 2010. The 17th American Conference on Crystal Growth and Epitaxy/The 14th US Biennial Workshop on Organometallic Vapor Phase Epitaxy/The 6th International Workshop on Modeling in Crystal Growth.
- [29] Z. Lei, C. Zhu, C. Xu, B. Yao, and C. Yang. Growth of crack-free ZnGeP_2 large single crystals for high-power mid-infrared OPO applications. *Journal of Crystal Growth*, 389:23 – 29, 2014.
- [30] P. E. Powers, C. L. Tang, and L. K. Cheng. High-repetition-rate femtosecond OPO using RbTiOAsO_4 . In *Conference on Lasers and Electro-Optics*, page CWM4. Optical Society of America, 1994.
- [31] L. P. Chen, Yong Wang, and J. M. Liu. Singly resonant optical parametric oscillator synchronously pumped by frequency-doubled additive-pulse mode-locked Nd:YLF laser pulses. *J. Opt. Soc. Am. B*, 12(11):2192–2198, Nov 1995.

- [32] V. Petrov. Parametric down-conversion devices: the coverage of the mid-infrared spectral range by solid-state laser sources. *Optical materials*, 34:536–554, 2012.
- [33] T. Y. Fan, G. Huber, R. L. Byer, and P Mitzscherlich. Spectroscopy and diode laser-pumped operation of Tm,Ho:YAG. *IEEE J. Quant. Electron.*, 24(6):924, 1988.
- [34] E. Lippert, S. Nicolas, G. Arisholm, K. Stenersen, and G. Rustad. Mid-infrared laser source with high power and beam quality. *App. Optics*, 45(16):3839, 2006.
- [35] X. M. Duan, Y. J. Shen, B. Q. Yao, and Y. Z. Wang. A 106 W Q-switched Ho:YAG laser with single crystal. *Optik International Journal for Light and Electron Optics*, 169:224, 2018.
- [36] M. Schellhorn. A comparison of resonantly pumped Ho:YLF and Ho:LLF lasers in CW and Q-switched operation. In *Advances in Optical Materials*, page AWA8. Optical Society of America, 2011.
- [37] M. Schellhorn and M. Eichhorn. High-energy Ho:LLF MOPA laser system using a top-hat pump profile for the amplifier stage. *App. Phy. B*, 109:351, 2012.
- [38] H. Fonnum, E. Lippert, and M. W. Haakestad. 550 mJ Q-switched cryogenic Ho:YLF oscillator pumped with a 100 W Tm:fiber laser. *Opt. Lett.*, 38(11):1884–1886, Jun 2013.
- [39] M. Schellhorn and G. Spindler. High-Efficient Resonantly Pumped Q-Switched Ho:LLF MOPA System. In *Laser Congress 2019 (ASSL, LAC, LS&C)*, page JTh3A.18. Optical Society of America, 2019.
- [40] W. Koen and C. Jacobs and L. Wu and H. J. Strauss. 60 W Ho:YLF oscillator-amplifier system. In *Solid State Lasers XXIV:Technology and Devices*, 2015. paper 93421Y.
- [41] A. Motard, C. Louot, T. Robin, B. Cadier, I. Manek-Honninger, N. Dalloz, and A. Hildenbrand-Dhollande. Diffraction limited 195-W continuous wave laser emission at 2.09 μm from a Tm³⁺, Ho³⁺-codoped single-oscillator monolithic fiber laser. *Opt. Express*, 29(5):6599–6607, 2021.
- [42] W. Yao, C. Shen, Z. Shao, Q. Liu, H. Wang, Y. Zhao, and D. Shen. High-power nanosecond pulse generation from an integrated Tm-Ho fiber MOPA over 2.1 μm . *Opt. Express*, 26(7):8841, 2018.

- [43] N. Dalloz, T. Robin, B. Cadier, C. Kieleck, M. Eichhorn, and A. Hildenbrand-Dhollande. 55 W actively Q-switched single oscillator Tm^{3+} , Ho^{3+} -codoped silica polarization maintaining 2.09 μm fiber laser. *Opt. Express*, 27(6):8387–8394, Mar 2019.
- [44] M. T. Kalichevsky-Dong, W. Ge, T. W. Hawkins, T. Matniyaz, and L. Dong. 4.8 mJ pulse energy directly from single-mode Q-switched ytterbium fiber lasers. *Opt. Express*, 29(19):30384–30391, Sep 2021.
- [45] D. Creeden, P. A. Ketteridge, P. A. Budni, S. D. Setzler, Y. E. Young, J. C. McCarthy, K. Zawilski, P. G. Schunemann, T. M. Pollak, E. P. Chicklis, and M. Jiang. Mid-infrared ZnGeP_2 parametric oscillator directly pumped by a pulsed 2 μm Tm-doped fiber laser. *Opt. Lett.*, 33(4):315–317, Feb 2008.
- [46] N. Dalloz, T. Robin, B. Cadier, C. Kieleck, M. Eichhorn, and A. Hildenbrand-Dhollande. High power Q-switched Tm^{3+} , Ho^{3+} -codoped 2 μm fiber laser and application for direct OPO pumping. In Adrian L. Carter and Liang Dong, editors, *Fiber Lasers XVI: Technology and Systems*, volume 10897, pages 90 – 97. International Society for Optics and Photonics, SPIE, 2019.
- [47] L. G. Holmen and H. Fonnum. Holmium-doped fiber amplifier for pumping a ZnGeP_2 optical parametric oscillator. *Opt. Express*, 29(6):8477–8489, Mar 2021.
- [48] G. Liu, S. Mi, K. Yang, D. Wei, J. Li, B. Yao, C. Yang, T. Dai, X. Duan, L. Tian, and Y. Ju. 161 W middle infrared ZnGeP_2 MOPA system pumped by 300 W-class Ho:YAG MOPA system. *Optics Letters*, 46(1):82–85, 2021.
- [49] I. Elder. Thulium fiber laser pumped mid-IR source. In Mark Dubinskii and Stephen G. Post, editors, *Laser Technology for Defense and Security V*, volume 7325, pages 98 – 108. International Society for Optics and Photonics, SPIE, 2009.
- [50] A. Hemming, J. Richards, A. Davidson, N. Carmody, S. Bennetts, N. Simakov, and J. Haub. 99 W mid-IR operation of a ZGP OPO at 25% duty cycle. *Opt. Express*, 21(8):10062–10069, Apr 2013.
- [51] L. Wang, T. Xing, S. Hu, X. Wu, H. Wu, J. Wang, and H. Jiang. Mid-infrared ZGP-OPO with high optical-to-optical conversion efficiency of 75.7%. *Opt. Express*, 25(4):3373, 2017.
- [52] M. Schellhorn, G. Spindler, and M. Eichhorn. Mid-infrared ZGP OPO with divergence compensation and high beam quality. *Opt. Express*, 26(2):1402–1410, Jan 2018.

- [53] B. Yao, Y. Shen, X. Duan, T. Dai, Y. Ju, and Y. Wang. A 41-W ZnGeP₂ optical parametric oscillator pumped by a Q-switched Ho:YAG laser. *Opt. Lett.*, 39(23):6589–6592, Dec 2014.
- [54] B. Zhao, B. Yao, C. Qian, G. Liu, Y. Chen, R. Wang, T. Dai, and X. Duan. 231 W dual-end-pumped Ho:YAG MOPA system and its application to a mid-infrared ZGP OPO. *Opt. Lett.*, 43(24):5989–5992, Dec 2018.
- [55] C. Qian, B. Yao, B. Zhao, G. Liu, X. Duan, T. Dai, Y. Ju, and Y. Wang. High repetition rate 102 W middle infrared ZnGeP₂ master oscillator power amplifier system with thermal lens compensation. *Opt. Lett.*, 44(3):715–718, Feb 2019.
- [56] E. Lippert, H. Fonnum, G. Arisholm, and K. Stenersen. A 22-watt mid-infrared optical parametric oscillator with V-shaped 3-mirror ring resonator. *Opt. Express*, 18(25):26475–26483, 2010.
- [57] A. V. Smith and M. S. Bowers. Image-rotating cavity designs for improved beam quality in nanosecond optical parametric oscillators. *J. Opt. Soc. Am. B*, 18(5):706–713, May 2001.
- [58] A. V. Smith and D. J. Armstrong. Nanosecond optical parametric oscillator with 90° image rotation: design and performance. *J. Opt. Soc. Am. B*, 19(8):1801–1814, Aug 2002.
- [59] S. Bigotta, G. Stöppler, J. Schöner, M. Schellhorn, and M. Eichhorn. Novel non-planar ring cavity for enhanced beam quality in high-pulse-energy optical parametric oscillators. *Opt. Mater. Express*, 4(3):411–423, Mar 2014.
- [60] M. Eichhorn, G. Stoppler, M. Schellhorn, M. T. Kawilski, and P. G. Schunemann. Gaussian versus flat-top-pumping of a mid-IR ZGP RISTRA OPO. *Appl. Phys. B*, 108:109–115, 2012.
- [61] M. Schellhorn, G. Spindler, and M. Eichhorn. Improvement of the beam quality of a high-pulse-energy mid-infrared fractional-image-rotation-enhancement ZnGeP₂ optical parametric oscillator. *Opt. Lett.*, 42(6):1185–1188, Mar 2017.
- [62] A. Dergachev, D. Armstrong, A. Smith, T. Drake, and M. Dubois. 3.4- μm ZGP RISTRA nanosecond optical parametric oscillator pumped by a 2.05- μm Ho:YLF MOPA system. *Opt. Express*, 15(22):14404–14413, 2007.
- [63] M. Ebrahimzadeh. *Mid-Infrared Ultrafast and Continuous-Wave Optical Parametric Oscillators*, pages 184–224. Springer Berlin Heidelberg, Berlin, Heidelberg, 2003.

- [64] Robert W Boyd. In *Nonlinear Optics*, chapter 2. Elsevier, third edition, 2007.
- [65] Venkata Ramaiah-Badarla. *Ultrafast optical parametric oscillators: Novel systems, techniques, and concepts*. PhD thesis, Intitut de Ciències Fotoniques-ICFO.
- [66] D. A. Kleinman. Nonlinear dielectric polarization in optical media. *Phys. Rev.*, 126:1977–1979, Jun 1962.
- [67] Arlee V. Smith. In *Crystal nonlinear optics: with SNLO examples*. AS-Photonics, second edition, 2018.
- [68] S.E. Harris. Tunable optical parametric oscillators. *Proceedings of the IEEE*, 57(12):2096–2113, 1969.
- [69] Evgeny Kovalchuk. *Optical Parametric Oscillators for precision IR spectroscopy and metrology*. PhD thesis, Mathematisch-Naturwissenschaftlichen Fakultät I Humboldt-Universität zu Berlin, 2007.
- [70] R. C. Eckardt, C. D. Nabors, W. J. Kozlovsky, and R. L. Byer. Optical parametric oscillator frequency tuning and control. *J. Opt. Soc. Am. B*, 8(3):646–667, Mar 1991.
- [71] W. Koechner. In *Solid-State Laser Engineering*, chapter 7. Springer, sixth edition, 2006.
- [72] A. V. Smith, W. J. Alford, and M. S. Bowers. Method to improve optical parametric oscillator beam quality, November 2003. US patent 6,647,034.
- [73] G. Marchev, M. Reza, V. Badikov, A. Esteban-Martin, G. Stoppler, M. Starikova, D. Badikov, V. Panyutin, M. Eichhorn, G. Shevyrdyaeva, A. Tyazhev, S. Sheina, A. Agnesi, A. Fintisova, and V. Petrov. Mid-infrared rotated image singly resonant twisted rectangle optical parametric oscillator based on HgGa₂S₄ pumped at 1064 nm. *Appl. Opt.*, 53(33):7951–7962, 2014.
- [74] G. Marchev, A. Tyazhev, G. Stöppler, M. Eichhorn, P. G. Schunemann, and V. Petrov. Comparison of linear and RISTRA cavities for a 1064-nm pumped CdSiP₂ OPO. In Konstantin L. Vodopyanov, editor, *Nonlinear Frequency Generation and Conversion: Materials, Devices, and Applications XI*, volume 8240, pages 70 – 76. International Society for Optics and Photonics, SPIE, 2012.
- [75] M. Eichhorn. Optical resonator for a laser beam, April 2013. European patent EP2581787A2.

- [76] O. Svelto. In *Principles of Lasers*, chapter 4. Springer, fifth edition, 2010.
- [77] A. E. Siegman. How to (maybe) measure laser beam quality. In *DPSS (Diode Pumped Solid State) Lasers: Applications and Issues*, page MQ1. Optical Society of America, 1998.
- [78] R. J. Hutcheon, B. J. Perrett, and P. D. Mason. Modelling of thermal effects within a 2- μm pumped ZGP optical parametric oscillator operating in the mid-infrared. In Jonathan A. C. Terry and W. Andrew Clarkson, editors, *Solid State Laser Technologies and Femtosecond Phenomena*, volume 5620, pages 264 – 274. International Society for Optics and Photonics, SPIE, 2004.
- [79] J. E. Tucker, C. L. Marquardt, S. R. Bowman, and B. J. Feldman. Transient thermal lens in a ZnGeP_2 crystal. *Appl. Opt.*, 34(15):2678–2682, May 1995.
- [80] W. Koechner. Transient thermal profile in optically pumped laser rods. *Journal of Applied Physics*, 44(7):3162–3170, 1973.
- [81] G. Arisholm, R. Paschotta, and T. Südmeyer. Limits to the power scalability of high-gain optical parametric amplifiers. *J. Opt. Soc. Am. B*, 21(3):578–590, Mar 2004.
- [82] F. Salin and J. Squier. Gain guiding in solid-state lasers. *Opt. Lett.*, 17(19):1352–1354, Oct 1992.
- [83] M. Piotrowski, M. A. Medina, M. Schellhorn, G. Spindler, and A. Hildenbrand-Dhollande. Effects of pump pulse energy and repetition rate on beam quality in a high-power mid-infrared ZnGeP_2 OPO. *Opt. Express*, 29(2):2577–2586, 2021.
- [84] A. Hildenbrand, C. Kieleck, A. Tyazhev, G. Marchev, G. Stöppler, M. Eichhorn, P. G. Schunemann, and V. Petrov. Laser damage studies of CSP_2 and ZnGeP_2 nonlinear crystals with nanosecond pulses at 1064 and 2090 nm. In Konstantin L. Vodopyanov, editor, *Nonlinear Frequency Generation and Conversion: Materials, Devices, and Applications XIII*, volume 8964, pages 162 – 169. International Society for Optics and Photonics, SPIE, 2014.
- [85] M. Eichhorn, M. Schellhorn, M. W. Haakestad, H. Fonnum, and E. Lippert. High-pulse-energy mid-infrared fractional-image-rotation-enhancement ZnGeP_2 optical parametric oscillator. *Opt. Lett.*, 41(11):2596–2599, Jun 2016.
- [86] <https://refractiveindex.info/>.
- [87] Richard J. Sutherland. In *Handbook of nonlinear optics*, chapter 3. Marcel Dekker, second edition, 2003.

- [88] H. Wang and A. M. Weiner. Efficiency of short-pulse type-I second-harmonic generation with simultaneous spatial walk-off, temporal walk-off, and pump depletion. *IEEE Journal of Quantum Electronics*, 39(12):1600–1618, 2003.
- [89] W. J. Alford, Russell J. Gehr, R. L. Schmitt, A. V. Smith, and G. Arisholm. Beam tilt and angular dispersion in broad-bandwidth, nanosecond optical parametric oscillators. *J. Opt. Soc. Am. B*, 16(9):1525–1532, Sep 1999.
- [90] J. A. Fleck and M. D. Feit. Beam propagation in uniaxial anisotropic media. *J. Opt. Soc. Am.*, 73(7):920–926, Jul 1983.
- [91] G. Rustad, E. Lippert, K. Stenersen, and G. Arisholm. Enhanced power from a doubly resonant optical parametric oscillator by choice of resonator length. In *Advanced Solid-State Lasers*, page WD5. Optical Society of America, 2001.
- [92] Y. Chen, G. Liu, B. Yao, R. Wang, C. Yang, X. Duan, T. Dai, and Y. Wang. Comparison of mid-infrared ZnGeP₂ rectangle ring optical parametric oscillators of three types of resonant regimes. *Applied Optics*, 58(15):4163, 2019.
- [93] S. Brosnan and R. Byer. Optical parametric oscillator threshold and linewidth studies. *IEEE Journal of Quantum Electronics*, 15(6):415–431, 1979.
- [94] G. Rustad, K. Stenersen, and G. Arisholm. Analysis of a high power ZGP OPO by numerical modeling. In *Advanced Solid State Lasers*, page WC9. Optical Society of America, 2000.
- [95] G. Anstett, A. Borsutzky, and R. Wallenstein. Investigation of the spatial beam quality of pulsed ns-OPOs. *Applied Physics B*, 76:541–545, 2003.
- [96] <https://www.las-cad.com/>.
- [97] W. A. Neuman and S. P. Velsko. Effect of cavity design on optical parametric oscillator performance. In *Advanced Solid State Lasers*, page OP12. Optical Society of America, 1996.
- [98] C. Kieleck, A. Berrou, B. Donelan, B. Cadier, T. Robin, and M. Eichhorn. 6.5 W ZnGeP₂ OPO directly pumped by a Q-switched Tm³⁺-doped single-oscillator fiber laser. *Optics Letters*, 40(6), 2015.
- [99] C. Fallnich, B. Ruffing, Th. Hermann, A. Nebel, R. Beigang, and R. Wallenstein. Experimental investigation and numerical simulation of the influence of resonator-length detuning on the output power, pulse duration

and spectral width of a CW mode-locked picosecond optical parametric oscillator. *Applied Physics B*, 60:427–436, 1995.

- [100] J. P. Gordon, R. C. C. Leite, R. S. Moore, S. P. S. Porto, and J. R. Whinnery. Long-transient effects in laser with inserted liquid samples. *J. Appl. Phy.*, 36:3–8, 1965.
- [101] F. Bai, Q. Wang and Z. Liu, Z. Jiao, X. Xu, and H. Zhang. Comparison of signal-resonant and idler-resonant KTA-SROs. *Chinese Optics Letters*, 14(7), 2016.
- [102] David E. Zelmon, Elizabeth A. Hanning, and Peter G. Schunemann. Refractive-index measurements and sellmeier coefficients for zinc germanium phosphide from 2 to 9 μm with implications for phase matching in optical frequency-conversion devices. *J. Opt. Soc. Am. B*, 18(9):1307–1310, Sep 2001.
- [103] K. Kato, Eiko Takaoka, and N. Umemura. New sellmeier and thermo-optic dispersion formulas for ZnGeP_2 . In *Conference on Lasers and Electro-Optics/Quantum Electronics and Laser Science Conference*, page CTuM17. Optica Publishing Group, 2003.
- [104] P.D. Mason, D.J. Jackson, and E.K. Gorton. CO_2 laser frequency doubling in ZnGeP_2 . *Optics Communications*, 110(1):163–166, 1994.